2015-08-01

Peroxy Radical - Water Complexes: Their Role in the Atmosphere

Sambhav Rajendra Kumbhani
Brigham Young University

BYU ScholarsArchive Citation

Kumbhani, Sambhav Rajendra, "Peroxy Radical - Water Complexes: Their Role in the Atmosphere" (2015). *All Theses and Dissertations*. 5729.
https://scholarsarchive.byu.edu/etd/5729

Peroxy Radical – Water Complexes: Their Role in the Atmosphere

Sambhav Rajendra Kumbhani

A dissertation submitted to the faculty of
Brigham Young University
in partial fulfillment of the requirements for the degree of

Doctor of Philosophy

Jaron C. Hansen, Chair
James E. Patterson
Daniel E. Austin
David V. Dearden
Adam T. Woolley

Department of Chemistry and Biochemistry

Brigham Young University

August 2015

This dissertation is dedicated to the Kumbhani family.

ABSTRACT

Peroxy Radical – Water Complexes: Their Role in the Atmosphere

Sambhav Rajendra Kumbhani
Department of Chemistry and Biochemistry, BYU
Doctor of Philosophy

The importance of radical-water complexes in the atmosphere is explored in this dissertation. Radicals, although present in small concentrations in the atmosphere, play a significant role in creating and removing atmospheric pollution. As the atmosphere warms and consequently gets wetter, it is essential to understand the effects of water vapor on radical chemistry. This dissertation reports studies on the effects of water vapor on the kinetics of the self-reaction of β-hydroxyethyl peroxy radical (β-HEP), a prominent organic peroxy radical in the atmosphere. Both experimental and computational studies have been performed to examine the effects of water vapor on the kinetics of the self-reaction. The influence of water vapor and temperature on the reaction rate constant is presented. The rate of the self-reaction increases between 2 to 6 times with an increase in water vapor and decrease in temperature. The products of the self-reaction in the presence and absence of water vapor have been computed using high level *ab initio* calculations. Major products include alkoxy radicals, peroxides, aldehydes, alcohols and oxygen. A new reaction pathway leading to formation of hydroperoxy radical (HO_2) from the self-reaction of β-HEP in the presence of water vapor was identified. In the presence of high NO_x concentration HO_2, forms tropospheric ozone, which is classified as a harmful pollutant by the Environmental Protection Agency (EPA).

Like tropospheric ozone, aerosols are also classified as harmful pollutants by the EPA. Sulfuric acid-water complexes are estimated to be the primary reason for new aerosol formation in the atmosphere. However, the sulfuric acid concentration in the atmosphere alone is not sufficient to account for observed aerosol concentrations. Classical nucleation theory is used to explain new particle formation (NPF), which is initiated by the formation of a nucleating site (a highly polar complex). This dissertation explores the role of various radical-molecule complexes acting as the nucleating site. Experimentally, the HO_2-water complex is studied as a possible nucleating site for NPF. A new instrument was developed to create and measure radical-water complex initiated particle formation. The instrument incorporates two scanning mobility particle sizers (SMPS) to measure the size distribution and number density of the aerosol particles formed. The experimental setup uses UV absorption spectroscopy and wavelength modulated spectroscopy to measure the HO_2 radical and water vapor concentrations in the reaction cell. No significant particle formation was observed at room temperature and pressure. Particle formation from the HO_2-water complex, may occur at lower temperatures.

Additional radical-molecule complexes have been studied computationally in an effort to identify other possible nucleating sites for particle formation. In particular, the complexes of sulfuric acid, nitric acid, acetic acid and formic acid with ammonia, amidogen radical (NH_2) and imidogen radical (NH) have been studied. H_2SO_4-NH_2 and HNO_3-NH_2 complexes show the potential to act as nucleating sites for formation of aerosol particles in the atmosphere.

In summary, water mediated chemistry plays a significant role in the atmosphere and must be included in scientific models to better predict pollution levels in the atmosphere.

Keywords: peroxy radical, radical-water complex, β-hydroxyethyl peroxy radical, aerosols, kinetics, self-reaction, ab-initio calculations

ACKNOWLEDGEMENTS

It is my proud privilege to have come under the guidance of Dr. Jaron Hansen at Brigham Young University. I thank him for his constant guidance and support, valuable suggestions, encouragement, personal attention, and being an inspiration during the course of my doctorate work. I acknowledge my earnest gratitude and everlasting regards towards him. I am thankful to all my committee members including Dr. Daniel Austin, Dr. David Dearden, Dr. James Patterson, and Dr. Adam Woolley for their kind support and helpful suggestions during my entire research work.

It is with a great deal of pleasure, I express my profound sense of gratitude to Dr. Lee Hansen and Dr. Randall Shirts for their invaluable suggestions for improvements in my research and their generous support throughout my research. I take this opportunity to thank all the professors at Brigham Young University, who, besides chemistry, also taught me some valuable life lessons. I am thankful to everyone from Hansen group including Will Keeton, Emma Burrell, Paul Cropper, Braden Myers, Dr. Taylor Cline, Dr. Jared Clark, Marie Killian, Makena Clive and other students in the group. I am thankful to all the supporting staff of the department including the Instrument shop, Precision Machine Laboratory, Janet Fonoimoana, Sue Mortensen, Peggy Erickson, Teresa Harper and all the secretaries.

I am thankful to all the new friends (too many to be named) I made in the United States. But, I am especially thankful to Vikas Asthana for sticking with me all this while. I am grateful for all the photoshoots and the Salt Lake City trips we made together; they really kept me sane throughout my research.

Last but not the least, I am profoundly thankful to my parents, Mr. Rajendra Kumbhani and Mrs. Malti Kumbhani, for their everlasting blessings, encouragement and support that has paved my path to success. I thank my dearest niece, Prisha, and her parents Mr. and Mrs. Modi for their support and for all those couriers they sent me all these years. It would have been almost impossible to survive without those couriers in this distant foreign land, I now call home.

TABLE OF CONTENTS

LIST OF TABLES

LIST OF FIGURES

Chapter 1

Introduction

Humans have enjoyed a stable climate since the last ice age, which ended several thousand years ago. Over the past century, our climate has changed rapidly due to human activities. Industrialization, boom in automotive usage and burning of fossil fuel are the principle reasons for the rapid climate change observed over the last 6 decades. The warming climate could bring drastic changes and affect water supplies, agriculture, power and transportation systems, and human health.

The chemistry of the atmosphere is complex and varies with place and time. The chemistry of the atmosphere might be local, but the effects of climate change are global. For example, pollution that is created in a factory in Shanghai, China not only affects Shanghai, but also affects the west coast of the United States, as part of this pollution may be carried over the Pacific Ocean to the United States by the wind.[1] Thus, addressing a pollution issue in one location might remedy the problem globally.

Pollution can have life threatening effects on humans, plants and animals.[2] A number of recent studies show the Arctic has warmed at twice the global rate causing the Arctic ice to melt.[3] This has direct effects on polar bears. Polar bears require ice layers over the sea to hunt their primary food source, seals.[4] In the past decade, the summer months in the Artic are constantly getting longer. This results in less ice for hunting seals. A recent study in the southern Beaufort Sea of the United States and Canada has shown that during 2001-2010, the number of polar bears in the area have reduced by 25-50%.[4] Due to the melting ice and changing habitat for the polar bears, the United States government in 2008 declared polar bears as a threatened species under the Endangered Species Act (ESA) of 1973.

Pollution is also responsible for various health hazards in humans including cancer and heart attacks and respiratory diseases.[5-7] The United States of America is one of the first few countries to recognize the health effects of climate change. In 1963, the United States Congress passed the Clean Air Act, which commissioned extensive research in atmospheric pollution and its effects. In 1970, the act was amended to give federal regulatory powers to the Environmental Protection Agency (EPA). The EPA maintains and enforces the National Ambient Air Quality Standards (NAAQS) in the United States.

EPA regularly updates the NAAQS. Presently, there are six major pollutants identified by the EPA as harmful for human health; ozone (O_3), nitrogen dioxide (NO_2), carbon monoxide (CO), lead (Pb), sulfur dioxide (SO_2), and particulate matter (PM 2.5 and PM 10). PM 2.5 represents the size of the particulate matter being anything below 2.5 µm in diameter and PM 10 being anything below 10 µm in diameter. This dissertation mainly focuses on ozone and particulate matter pollution. Particulate matter is also referred to as an aerosol.

1.1 Sources of Ozone and Aerosol Pollution

Ozone: Ozone naturally exists in the stratosphere, (10-25km above sea level) as a filter for harmful solar radiation (<300nm) coming to earth from the sun. Ozone formation in the stratosphere occurs via oxygen photolysis.[8]

$$O_2 + h\upsilon\ (\lambda < 240\text{nm}) \rightarrow 2O\bullet \quad (1.1)$$

$$O\bullet + O_2 \rightarrow O_3 \quad (1.2)$$

$$O_3 + O\bullet \rightarrow 2O_2 \quad (1.3)$$

Ozone in the stratosphere reacts with oxygen atoms to form oxygen molecules in the stratosphere via reaction 1.3. Due to the ozone cycle, the total ozone concentration is never more than 0.6ppm in the stratosphere. However, due to industrialization and use of chlorofluorocarbons (CFC) as a refrigerant, the ozone depletion was observed in the late 20th century.

Chlorofluorocarbons photolyze to form chlorine radicals in the stratosphere where short wavelengths of UV light are available. Chlorine radicals then react with ozone to form oxygen molecules and ClO radical.

$$\text{CFC} + h\upsilon \rightarrow Cl\bullet \quad (1.4)$$

$$Cl\bullet + O_3 \rightarrow ClO\bullet + O_2 \quad (1.5)$$

$$ClO\bullet + O \rightarrow Cl\bullet + O_2 \quad (1.6)$$

The chlorine radical formed in reaction 1.6 reacts with more ozone molecules converting them to oxygen and depleting the ozone layer. Each chlorine radical can remove approximately 1 x 10^6 ozone molecules from the stratosphere before the radical is removed.[8] The issue of CFC's destroying the ozone layer in the stratosphere has been addressed by replacing them with hydrochlorofluorocarbons (HCFC). HCFC's are engineered to have a shorter atmospheric lifetime in the troposphere, which minimizes the amount of these compounds that can be introduced into the upper atmosphere.

NO_x (NO, NO_2, and NO_3), HO_x (OH, HO_2) and volatile organic compounds (VOC) are primary precursors of ozone formation in the troposphere. Tropospheric ozone (0 to 10 km) is extremely harmful to flora and fauna, including humans. Human activities produce tropospheric ozone. Automotive and industrial emissions release NO_x ($NO_x = NO, NO_2$, and NO_3) gases into the atmosphere, which form tropospheric ozone via the following reactions (1.7 and 1.8)

$$NO_2 + h\nu \rightarrow NO + O\bullet \qquad (1.7)$$

$$O\bullet + O_2 \rightarrow O_3 \qquad (1.8)$$

VOCs are released into the atmosphere from both biogenic and anthropogenic sources. Major VOCs in the atmosphere include terpenes, isoprene, α-pinene and ethylene. VOCs such as formaldehyde and formic acid are photolyzed with wavelengths less than 370nm to form OH or HO_2 radical.[8] A variety of oxidants including OH, Cl, and NO_3 react with VOCs to form organic peroxy radicals (RO_2) in the presence of oxygen (reaction 1.10-1.11). RO_2 further reacts with NO to form RO and NO_2 (reaction 1.12). NO_2 further photolyzes to form ozone by reactions 1.7-1.8. This cycle continues to produce ozone during daytime.

$$\mathrm{HONO\bullet} + h\nu \rightarrow \mathrm{OH\bullet} + \mathrm{NO_2} \qquad (1.9)$$

$$\mathrm{OH\bullet} + \mathrm{RH} \rightarrow \mathrm{H_2O} + \mathrm{R\bullet} \qquad (1.10)$$

$$\mathrm{R\bullet} + \mathrm{O_2} \rightarrow \mathrm{RO_2\bullet} \qquad (1.11)$$

$$\mathrm{RO_2\bullet} + \mathrm{NO} \rightarrow \mathrm{RO\bullet} + \mathrm{NO_2} \qquad (1.12)$$

Aerosol: Sources of aerosol are classified as primary and secondary sources. Primary sources release aerosol particles directly into the atmosphere. Secondary sources release the precursors for formation of aerosols. Both primary and secondary sources can have natural or anthropogenic origins. Volcanic emissions, forest fires, and storms introduce the majority of aerosols into the atmosphere.[9] Volcanic emissions release sulfate particles into the atmosphere. Volcanic emissions are known to cool the planet, as large amounts of particles are released in a short period of time.[9] The massive amount of particles released reflect and scatter incoming solar radiation and thus cool the planet. Volcanic emissions also release precursors like SO_2 that lead to aerosol formation in the atmosphere. SO_2 gas undergoes oxidation in the presence of OH radical and molecular oxygen to form sulfuric acid, which eventually forms aerosols via the nucleation process with water vapor. In 1991, the eruption of

Mount Pinatubo in the Philippines ejected more than 20 million tons of sulfate particles into the stratosphere.[8] These particles remained above the clouds and not washed from the sky by rain; settling only after several years. Following the eruption, global temperatures abruptly dipped by about a half-degree (0.6°C) for approximately two years. A large amount of volcanic ash is also released into the atmosphere, but the lifetime is much shorter than aerosol particles because volcanic ash consists of larger particles that fall out quickly. Similarly, during forest fires a large amount of ash and soot particles are released into the atmosphere.

Anthropogenic primary emission sources include coal fired power plants, industrial emissions and automotive emissions. Coal fired power plants produce carbon based aerosol particles, also known as soot, which contribute to global warming of the planet. Automotive and industrial emissions produce sulfate particles (especially diesel emissions) and release particle formation precursors like SO_2 and NO_x gases that react in the atmosphere to form sulfate and nitrate.

The nucleation process is the primary reason for secondary particle formation in the atmosphere. Formation of aerosols is described by classical nucleation theory as a two-step process. The first step is the nucleation step where molecules cluster together. The second step is subsequent growth of the clusters through coagulation or condensation. Figure 1 describes the formation of sulfate aerosol particles via homogeneous nucleation of sulfuric acid and water vapor. Sulfuric acid hydrogen bonds with the surrounding water molecules, due to their polar nature, forming the critical cluster (~1nm). The critical cluster then undergoes coagulation to form the aerosol particle (~60-100nm). The aerosol particle keeps growing in size until it forms cloud condensation nuclei (~100-250nm), which in turn grows to form a cloud droplet. Thousands of such cloud droplets form the cloud. More and more water droplets coalesce until the saturation point is reached and the water falls out of the cloud as rain. In addition to molecule-molecule homogenous nucleation, this dissertation proposes radical-molecule homogenous nucleation as a novel source of particle formation in the atmosphere.

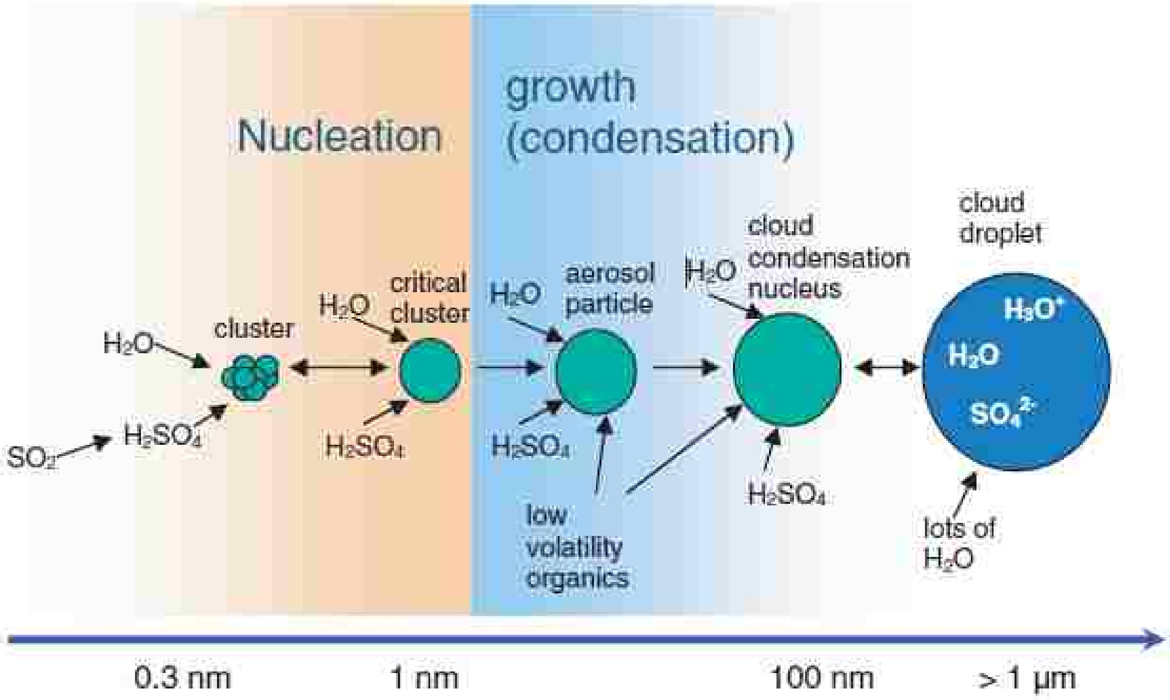

Figure 1 The formation of sulfate aerosol particle via homogeneous nucleation of sulfuric acid and water vapor. Adapted from Curtius et al.[10]

1.2 Effects of Ozone and Aerosol Pollution.

Ozone: Stratospheric ozone is helpful for humans and the climate, as it protects the flora and fauna from harmful radiation from the sun. However, tropospheric ozone is very harmful to flora and fauna. Tropospheric ozone causes many breathing related disorders in humans including shortness of breath, sore and scratchy throat, inflammation of airways, aggravating asthma and bronchitis and makes the lungs more susceptible to infections.

Children are at greatest risk from exposure to ozone because their lungs are still developing and they are more likely to be active outdoors when ozone levels are high, which increases their exposure. Tropospheric ozone also affects plants. As a strong oxidant, ozone causes several types of symptoms including chlorosis and necrosis, leading to discoloration of leaves and fruits. Heagle *et al.* in 1989 showed that crop yields are decreased by 40% when plants such as soybean, peanuts and cotton are exposed to 100ppb ozone.[11] Ozone concentrations in most urban areas of the United States have declined with improved emission controls, but are still high enough to damage crops.[12] Vehicular emissions and coal fired power plant emissions such as NO, and VOC (volatile organic carbon) act as precursors for the formation of ozone. Ozone levels are rising in countries like India and China, as growing populations are able to afford more cars and build more power plants. Another aspect of this concern is that ozone levels will rise in developing countries where people can least withstand the loss of staple foods such as rice and wheat.

Ozone has direct effects on climate. Ozone is one of the greenhouse gases capable of absorbing incoming solar radiation, thus warming the climate.[13-14] Quantifying the greenhouse gas potency of ozone is difficult because it is not present in uniform concentrations across the globe. However, the Intergovernmental Panel on Climate Change (IPCC) suggested the radiative forcing of tropospheric ozone is about 25% that of carbon dioxide.[3, 13] The annual global warming potential of tropospheric ozone is between 918–1022 tons carbon dioxide equivalent/ton tropospheric ozone. This means on a per-molecule basis, ozone in the troposphere has a radiative forcing effect roughly 1,000 times as strong as carbon dioxide. However, tropospheric ozone is a short-lived greenhouse gas, which decays in the atmosphere much more quickly than carbon dioxide. This means that over a 20 year span, the global warming potential of tropospheric ozone is much less, roughly 62 to 69 tons carbon dioxide equivalent/ton tropospheric ozone. Because of its short-lived nature, tropospheric ozone does not have strong global effects, but has very strong radiative forcing effects on regional scales. In fact, there are regions of the world where tropospheric ozone has a radiative forcing up to 150% of carbon dioxide.

<u>Aerosols</u>: Particulate matter (PM) are also known as aerosols. Aerosol are tiny particles (<10μm) of solid or liquid suspended in air. Aerosol particle diameters

range from 0.01-10 μm. Aerosols affect human health, visibility and the global atmosphere on a large scale. Increased mortality rates and other health problems associated with particulate pollution was first demonstrated[15] in the early 1970s and have been reproduced many times since.[2, 5-7] PM pollution is estimated to cause 22,000-52,000 deaths per year in the United States (in 2000)[16], whereas ~370,000 premature deaths were attributed to PM pollution in Europe during 2005 and 3.22 million deaths globally in 2010 per the global burden of disease collaboration.[17] An increase in estimated annual exposure to PM 2.5 of just 5 μg/m^3 was linked with a 13% increased risk of heart attacks.

The effect of inhaling aerosols has been widely studied in humans and animals and include asthma, lung cancer, cardiovascular disease, respiratory diseases, premature delivery, birth defects, and premature death.[7] The effect is largely dependent on the size of the aerosol particles. Particles greater than 10 μm filter out in the nose and mouth via mucus or cilia, and are not as harmful. Particles smaller than 2.5μm are capable of entering the lungs and reaching the alveolus and bronchioles. Pope *et al* [6] indicated that breathing PM$_{2.5}$ leads to high plaque deposits in arteries, causing vascular inflammation and atherosclerosis - a hardening of the arteries that reduces elasticity, which can lead to heart attacks and other cardiovascular problems. A 2014 meta-analysis reported that long-term exposure to particulate matter is linked to coronary events.[18]

The World Health Organization (WHO) estimated in 2005 that "Fine particulate air pollution (PM(2.5)), causes about 3% of mortality from cardiopulmonary disease, about 5% of mortality from cancer of the trachea, bronchus, and lung, and about 1% of mortality from acute respiratory infections in children under 5 years, worldwide."[2] Short-term exposure at elevated concentrations can significantly contribute to heart disease. Nawrot *et al* [19] showed that traffic exhaust is the single most serious preventable cause of heart attack in the general public, the cause of 7.4% of all attacks.

Lastly, particles smaller than 100nm are the most dangerous of all. Nanoparticles can pass through cell membranes and migrate into other organs, including the brain. Particles emitted from modern diesel engines (commonly referred to as Diesel Particulate Matter or DPM) are typically in the size range of 100 nanometers (0.1 micrometer). [8]

Aerosols have both direct and indirect effects on the climate. Aerosols are responsible for cloud formation in the atmosphere; without aerosols there would be no clouds. Clouds are estimated to reflect ~60% of incoming solar radiation causing the planet to cool; this is the indirect effects of aerosols. The most direct effect of aerosols is reduced visibility as aerosol particle can scatter, reflect or absorb incoming solar radiation. Whether the particle will absorb, scatter, or reflect incoming radiation depends on the particle composition. Aerosol particles made of carbon and VOC tend to absorb incoming solar radiation. Water based secondary aerosol particles are capable of reflecting incoming solar radiation. The extent of warming or cooling of aerosol particles is a subject of much research. The latest IPCC report[13] released in November 2014 predicts the effect of aerosol on the climate is towards cooling. The reason associated with the IPCC prediction is due to the indirect effects of the aerosols. Thereby, aerosols are the most important aspect of climate that can counter the global warming effect.

1.3 Radical–Water Complexes and their Effects on the Climate

Although radicals are found in much smaller concentrations in the atmosphere than carbon dioxide, water vapor, oxygen or nitrogen gas, they are very reactive and as such are important components of air. Some of these radicals include hydroperoxy radical (HO_2), hydroxyl radical (OH), chlorine radical (Cl), and alkyl radicals (R). Water molecules significantly influence the properties and reactions of these radicals. In 1975, Hamilton[20] discovered that water vapor increases the self-reaction rate of HO_2. Since then, numerous studies have verified and refined the findings of this first study.[21-27] The complete rate expression, including the temperature and pressure dependence of this reaction, was published in 1984.[24] Hamilton's original work stated that enhancement of the HO_2 self-reaction rate occurs with polar gases and hypothesized that the increased reaction rate was caused by formation of a complex between HO_2 and H_2O. Existence of an HO_2-H_2O complex has since been experimentally verified by Suma *et al.*[28] More recent studies have evaluated the equilibrium constant for the formation of the HO_2-H_2O complex as well as the rate enhancement by NH_3 and CH_3OH.[29-31]

The catalytic effect of water has been discussed at length without agreement on a general theory for predicting a change in the rate of specific reactions in response to changes in water vapor concentration.[32-38] Stockwell[39] modeled the water vapor enhancement of the HO_2 self-reaction as it affects atmospheric HO_x and O_3 budgets, and predicted decreased concentrations of HO_2 and H_2O_2 under saturated water conditions and thereby decreasing the O_3 concentration. The concentrations of O_3 and HO_x were previously overestimated by as much as 75% at the surface and 30% at 10 km. Butkovskaya *et al.*[40] recently showed that 50% relative humidity (4×10^{17} molecules cm^{-3} at 298 K), displaced the branching ratio of the reaction of HO_2 + NO away from NO_2 production and increased the production of HNO_3 by 800%. They hypothesized that a water molecule complexed to HO_2 serves as an energy sink and consequently drives the formation of HNO_3 at the expense of OH and NO_2.

Although the HO_2 self-reaction rate is increased by water, water has no measurable effect on the self-reaction rate of methyl peroxy radical (CH_3O_2) or the reaction of CH_3O_2 + HO_2.[37] The absence of catalysis by water is explained by the small fraction of CH_3O_2 complexed with water, owing to the small binding energy, calculated to be 8.8 kJ mol^{-1}. At 100% relative humidity and 298 K, the percentage of CH_3O_2-H_2O complex is only 0.02%, substantially less than the 8–15% calculated for the HO_2-H_2O complex,[41] which is calculated to be bound by 28.9 kJ mol^{-1}. Recent computational work[42] indicates that other alkyl peroxy radicals can also complex with water vapor. Khan *et al.*[43] in a recent atmospheric global modeling study using the STOCHEM-CRI model, predicted that as much as 17% of peroxy radicals in the upper troposphere exist as compelxes. This dissertation reports studies on the effect of water vapor on the self reaction of β-hydroxyethyl peroxy radical (β-HEP), a product of ethylene oxidation. The effect of water vapor on the self-reaction rate of β-HEP is discusssed in more detail in chapter 2.

The self reaction of peroxy radicals has two major product pathways. One forms alkoxy radicals and the other forms aldehydes and alcohols as products.[44] It is difficult to measure the products formed experiemntally, though some studies have been performed using FTIR as the detector.[45] Various theoretical papers have been published that predict the mechanism involved for both pathways.[46-47] To the best of my knowledge no theoretical studies have been performed on the effect of water vapor on the product branching ratio of peroxy radical self reaction. Chapetr 3 discusses the effect of water vapor on the self reaction of β-HEP. *Ab initio* calculations have been used to predict the products of β-HEP self reaction in the presence and absence of water vapor.

There are several forms of water found in the atmosphere including gaseous water clusters, cloud droplets, and liquid aerosols. Hydrogen-bonding interaction between free radicals and water molecules plays an important role in controlling the abundance and chemical behavior of free radicals in the atmosphere. The behavior of free radical-molecule complexes are of interest to the atmospheric chemist because radical reactions in the atmosphere can be affected by the uptake of radicals by aqueous aerosols and cloud droplets. Theoretically, it has been shown that, water cannot condense on its own to form cloud condensation nuclei to initiate cloud formation. It would take 10^{54} seconds to form a water droplet in $1cm^3$ at 200% relative humidity. Nucleation theory[10] suggests that this is because of the surface energy barrier for formation of a water cluster. This barrier is greatly reduced in the presence of an aerosol particle, ion or a surface on which water molecules can condense. I hypothesize that HO_2 radical, like neutral molecules or ions, can also lower the energy barrier to form a water cluster. Previous computational work has shown that HO_2 radical, due to its strong dipole moment, has a polarizing effect on clusters that form around a nucleus composed of an HO_2 radical. Due to its strong polarizing effect in small water clusters ($n < 20$), it is theorized that HO_2 will serve as a better nucleating agent than just a cluster of water because thermodynamically it is easier to “attach” additional water to a polarized cluster. We believe that HO_2 radical, which is highly acidic, will react with the surrounding polar water molecules and form hydrogen bonds. This would lead to formation of HO_2-H_2O complex, which would act as the nucleating seed for the nucleation process to begin for the formation of the aerosol particle, as predicted by nucleation theory. This is discussed in more detail in chapter 4.

Aerosol production via homogenous nucleation is enhanced 100-1000 times in the presence of a base like ammonia.[48] It is assumed that an acid-base reaction forms a strong complex, which acts as the critical cluster to initiate the nucleation process. To understand the role of ammonia and its radicals (NH_2 and NH) on acid nucleation *ab initio* calculations were used to predict the complex forming capacity of various acids in the atmosphere including sulfuric acid, nitric acid, formic acid and acetic acid. This is work is published in the Journal of chemical physics and is presented in Chapter 5.

Chapter 2

Water Vapor Enhancement of Rates of Peroxy Radical Reactions

Disclaimer: The following chapter is presented here in its entirety (with minor changes) from the published version of the paper in International Journal of Chemical Kinetics. Kumbhani, S. R.; Cline, T. S.; Killian, M. C.; Clark, J. M.; Keeton, W. J.; Hansen, L. D.; Shirts, R. B.; Robichaud, D. J.; Hansen, J. C., Water Vapor Enhancement of Rates of Peroxy Radical Reactions. *International Journal of Chemical Kinetics* **2015,** *47* (6), 395-409. Dr. Taylor Cline constructed the equipment and made the measurements. I wrote the paper, analyzed all the data and performed all the computations. Marie Killian, Dr. Jared Clark and Will Keeton assisted with computations. Dr. Lee Hansen, Dr. Randall Shirts, Dr. David Robichaud and Dr. Jaron Hansen reviewed and edited the work.

Abstract

Peroxy radicals can complex with water vapor. These complexes affect tropospheric chemistry. In this study, β-HEP (hydroxyethyl peroxy radical) serves as a model system for investigating the effect of water vapor on the kinetics and product branching ratio of the self reaction of peroxy radicals. The self-reaction rate coefficient was determined at 274–296 K with water vapor between 1.0×10^{15} and 2.5×10^{17} molecules cm^{-3} at 200 torr total pressure by slow-flow laser flash photolysis coupled with UV time-resolved spectroscopy

and long-path, wavelength modulated, diode-laser spectroscopy. The overall self-reaction rate constant expressed as the product of both a temperature dependent and water vapor dependent term is $k_o = 7.8 \times 10^{-14} exp((8.3 \pm 2.5\ kJ/mol)/\mathrm{R}T) + \{(13.2 \pm 1.56) \times 10^{-44} \times exp((79.3 \pm 17.18\ kJ/mol)/\mathrm{R}T) \times [H_2O]\}$ suggesting formation of a β-HEP-H_2O complex is responsible for the increase in the self-reaction rate coefficient with increasing water concentration. Complex formation is supported by computational results identifying three local energy minima for the β-HEP-H_2O complex. As the troposphere continues to get warmer and wetter, more of the peroxy radicals present will be complexed with water. Investigating the effect of water vapor on kinetics of atmospherically relevant radicals and determining the effects of these altered kinetics on tropospheric ozone concentrations is thus important.

2.1 Introduction

A direct relationship has been established between surface temperature and tropospheric water vapor. As the Earth continues to warm and tropospheric water vapor increases, water mediated chemistry has the potential to perturb the chemistry of the troposphere.[9, 49] Organic peroxy radicals (RO_2) are intermediates in the oxidation of hydrocarbons and are precursors for tropospheric ozone formation.[8] This work provides experimental evidence for an increased self-reaction rate of the organic peroxy radical, hydroxyethyl peroxy radical (β-HEP; $HOCH_2CH_2O_2$), in the presence of water vapor. β-HEP is a derivative of ethylene and plays a significant role in tropospheric chemistry.

Ethylene is released both naturally from vegetation and from combustion of wood and fossil fuels with an estimated total emission of 18–25 Tg yr^{-1}.[50] A typical urban environment contains 50 μg m^{-3} of ethylene with peak concentrations up to 1000 μg m^{-3} during high traffic hours, whereas rural environments range from 1–5 μg m^{-3}. As the troposphere continues to get warmer and wetter, more complexes with water will form, which in turn may perturb the kinetics and product branching ratios of atmospherically important reactions. For example, all unsaturated hydrocarbons will add OH across the double bond, and the addition of O_2 will produce β-hydroxy peroxy radicals. Isoprenes and terpenes are two major examples of biogenic sources that will produce β-hydroxy peroxy radicals. If β-HEP demonstrates a self-reaction rate enhancement, we hypothesize that peroxy radicals formed from other unsaturated hydrocarbons will also show enhanced rates with water vapor.

In 1975, Hamilton[20] discovered that water vapor increases the self-reaction rate of hydroperoxy radical (HO_2). Since then, numerous studies have verified and refined the findings of this first study.[21-27] The complete rate expression, including the temperature and pressure dependence of this reaction, was published in 1984.[24] More recent studies have evaluated the equilibrium constant for formation of the HO_2-H_2O complex as well as the rate enhancement by NH_3 and CH_3OH.[29-31] Hamilton's original work stated that enhancement of the HO_2 self-reaction rate occurs with polar gases and hypothesized that the increased reaction rate was caused by formation of a complex between HO_2 and H_2O. Existence of an HO_2-H_2O complex has since been experimentally verified by Suma *et al.*[28]

The catalytic effect of water has been discussed at length without agreement on a general theory for predicting a change in the rate of specific reactions in response to changes in water vapor concentration.[32-38] Stockwell[39] modeled the water vapor enhancement of the HO_2 self-reaction as it affects atmospheric HO_x and O_3 budgets, and predicted decreased concentrations of HO_2 and H_2O_2 under saturated water conditions and thereby decreasing the O_3 concentration. The concentrations of O_3 and HO_x were previously overestimated by as much as 75% at the surface and 30% at 10 km. Butkovskaya *et al.*[40] recently showed that 50% relative humidity (4×10^{17} molecules cm^{-3} at 298 K), displaced the branching ratio of the reaction of HO_2 + NO away from NO_2 production and increased the production of HNO_3 by 800%. They hypothesized that a water molecule complexed to HO_2 serves as an energy sink and consequently drives formation of HNO_3 at the expense of OH and NO_2.

Although the HO_2 self-reaction rate is increased by water, water has no measurable effect on the self-reaction rate of methyl peroxy radical (CH_3O_2) or the reaction of CH_3O_2 + HO_2.[37] The absence of catalysis by water is explained by the small fraction of CH_3O_2 complexed with water owing to the small binding energy, calculated to be 8.8 kJ mol^{-1}. At 100% relative humidity and 298 K, the percentage of CH_3O_2-H_2O complex is only 0.02%, substantially less than the 8–15% calculated for the HO_2-H_2O complex,[41] which is calculated to be bound by

28.9 kJ mol^{-1}. This is comparable to the binding energy calculated for the β-HEP-H_2O complex (27.4 kJ mol^{-1}). Recent computational work[42] indicates that other alkyl peroxy radicals can also complex with water vapor. Khan *et al.*[43] in a recent atmospheric global modeling study using the STOCHEM-CRI model, predicted that as much as 17% of peroxy radicals in the upper troposphere can exist as compelxes.

β-HEP serves as a model system for investigating the possible role of water vapor in perturbing the kinetics and product branching ratios of other alkyl peroxy radicals. For water vapor enhancement to be observed, a significant portion of reactants must form a radical-molecule complex.[51-52] β-HEP is chosen as a model radical to test the theory that strongly hydrogen-bonded complexes increase the rate of self-reaction. Clark *et al.*[42] demonstrated that the optimized structure predicted for the β-HEP-H_2O complex is stabilized by the formation of two intermolecular hydrogen bonds, as is the HO_2-H_2O complex. The self-reaction rate constant of β-HEP has previously been established in several studies.[53-61] However, the kinetics of the effects of water vapor on the self reaction of β-HEP has not been studied. Khan *et al.*[43] concluded in their modeling study “ the reaction between $RO_2.H_2O$ and NO, RO_2/HO_2 are worthy of investigation.”

This study presents experimental evidence for the catalytic effect of water vapor on the β-HEP self-reaction. We derive an empirical equation from experimental measurements expressing the β-HEP self-reaction rate constant as a function of temperature and water vapor. High level *ab initio* calculations are used to calculate the equilibrium constant for the formation of the β-HEP-H_2O complex. The temperature range and water vapor concentrations were chosen because of their significance to conditions in the troposphere.

2.2 Methods

2.2.1 Computational Methods

Gaussian 03[62] was used to compute the equilibrium constant for complexation of β-HEP with H_2O. Both harmonic and anharmonic vibrational frequencies and rotational constants of both the β-HEP molecule and the β-HEP-H_2O complex were optimized with the B3LYP/aug-cc-pVDZ method and basis set. The energies were refined by performing single-point energy calculations with the MP2 and CCSD(T) methods. One global minimum and one local minimum structure were identified for the β-HEP molecule. These structures are shown in Figure 2. One global and two local minima energy structures for β-HEP-H_2O (Figure 3) complex were identified by Gaussian optimizations through Random Constrained Sampling (RCS) methodology[33] (see Figure 2). The energies of each local and global minimum energy structure were zero-point energy corrected and basis set superposition error corrected[63] from energies calculated with the B3LYP/aug-cc-pVDZ method and basis set in Gaussian 03. All local minima with energies within kT (2.5 kJ/mol) of the global minimum geometry have measurable probability of being populated at room temperature, and therefore all the geometries were used in the equilibrium constant calculation. Appendix 2 includes the Cartesian coordinates of all the geometries in the chapter.

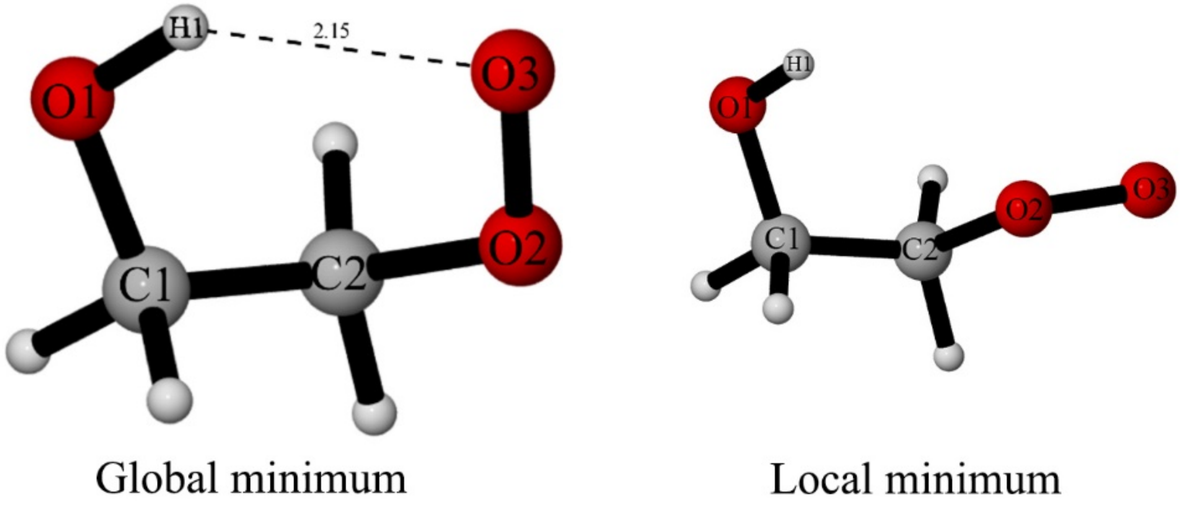

Figure 2 Optimized geometries of β-HEP. Bond lengths reported in Angstroms

- *2.2.1.1 Partition function calculations*

From the Gaussian 03 calculations, the partition function of each conformation of each molecule was calculated according to the theory by McQuarrie and Simon.[43] The overall partition function for a molecule is approximated by the product of its translational, rotational, electronic, and vibrational partition functions, which are assumed to be separable. The expressions for the translational, rotational, and electronic partition functions are:

$$q^T = \frac{V(2\pi mkT)^{3/2}}{h^3} \qquad \text{(Eq 1)}$$

where V is the volume of the reaction cell, m is the mass of the molecule, k is Boltzmann's constant, h is Planck's constant, and T is temperature;

$$q^R = \left(\frac{kT}{hc}\right)^{3/2} \left(\frac{\pi}{ABC}\right)^{1/2} \qquad \text{(Eq 2)}$$

where c is the speed of light and A, B, and C are the rotational constants of the molecule;

$$q^E = ge^{-E/(RT)} \qquad \text{(Eq 3)}$$

where g is the degeneracy of the electronic ground state and E is the zero-point energy of the ground vibrational state. Note that the energy in the partition function for all molecules and geometries must be in reference to the same reference energy.

- *2.2.1.2 Vibrational partition function*

The vibrational partition function for a molecule is the product of the partition functions for each of its vibrational modes, assuming that the normal vibrational modes of the molecule are independent. The partition function of a vibrational mode can be calculated as the sum of the contributions from each vibrational state,

$$q^V = \sum_v e^{-\beta E_v} \qquad \text{(Eq 4)}$$

where $\beta = (kT)^{-1}$. The energies of the vibrational states can be calculated according to several models for the vibrational motions. In this calculation, the harmonic oscillator, Morse oscillator, and hindered rotor models were used for each mode according to the model that best approximated the vibrational motion of the mode.

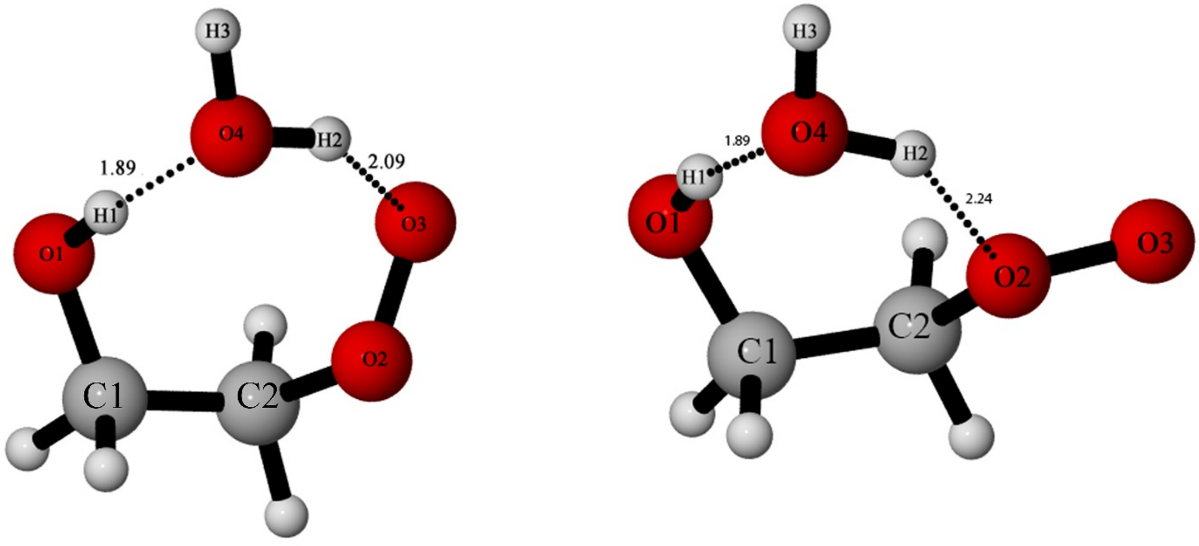

Global Minimum

Local Minimum 1

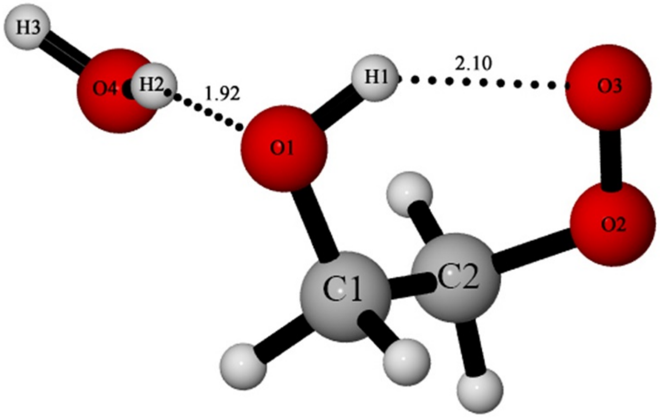

Local Minimum 2

Figure 3 Optimized geometries of β-HEP-H_2O. Bond lengths reported in angstroms.

- *2.2.1.3 Harmonic oscillator*

A harmonic approximation assumes that the energy levels of a vibrational mode are equally spaced. This approximation is accurate for the lowest vibrational states and therefore can be made when only the ground and first excited states are occupied. For a harmonic oscillator, equation 4 becomes

$$q^{V} = \sum_{v} e^{-\beta v h c \tilde{\nu}} = \frac{1}{1 - e^{-\beta h c \tilde{\nu}}} \qquad \text{(Eq 5)}$$

where $\tilde{\nu}$ is the fundamental frequency of the vibrational mode. In this calculation, the fundamental anharmonic frequency calculated in Gaussian was used for $\tilde{\nu}$.

- *2.2.1.4 Morse oscillator*

A Morse oscillator can be used to model vibrational modes that are dissociative. A harmonic oscillator model assumes that all vibrational states are equally spaced and does not account for the possibility that a bond can dissociate with sufficient energy. Therefore, the partition function based on the harmonic oscillator tends to underestimate the true partition function of the mode. The Morse oscillator accounts for the decreasing spacing between the vibrationally excited states and eventually the dissociation of the bond. The energy levels for the Morse oscillator potential are given by,

$$G(v) = v_e\left(v + \frac{1}{2}\right) + x_e\left(v + \frac{1}{2}\right)^2 \qquad \text{(Eq 6)}$$

where v_e is the fundamental harmonic vibrational frequency, v is the vibrational quantum number, and x_e is the diagonal element of the X-matrix corresponding to the vibrational mode. If x_e is negative, the bond will eventually dissociate, whereas if x_e is positive there are infinitely many bound states. The bond will dissociate when $G(v)$ achieves a maximum, or at $v^* = -\frac{v_e}{2x_e} - \frac{1}{2}$.

Therefore, at the highest energy bound state, $v_{max} = \lfloor v^* \rfloor$ and there are $N = v_{max} + 1$ bound states. For some states, if the vibration primarily involved the stretching of a hydrogen bond, $\tilde{x}_e$ was calculated from the dissociation energy for the breaking of the hydrogen bond, D,

$$\tilde{x}_e = -\frac{v_e^2}{4D} \qquad \text{(Eq 7)}$$

N was then calculated as $-\frac{v_e}{2\tilde{x}_e}$ and rounded to the nearest integer. The partition function was then calculated,

$$q^V = \sum_{v=0}^{v_{max}} e^{-hc(G(v)-G(0)/(kT)} \qquad \text{(Eq 8)}$$

from $\tilde{x}_e$ to calculate $G(v)$ and $G(0)$.

- *2.2.1.5 Hindered rotor*

A hindered rotor model was used to model vibrations that involve the rotation of a functional group on the molecule. The calculation of the partition function for a hindered rotor vibration was based on McClurg *et al.*[42]

$$q^V = q_{HO}\left(\frac{r\pi}{\theta}\right)^{1/2} e^{-r/(2\theta)} I_0\left(\frac{r}{2\theta}\right) \qquad \text{(Eq 9)}$$

where q_{HO} is the partition function calculated as a harmonic oscillator using the fundamental harmonic frequency , and r and θ are defined as

$$r = \frac{\sqrt{2Iw}}{\hbar} \qquad \text{(Eq 10)}$$

$$\theta = \frac{kT}{\hbar}\sqrt{\frac{2I}{w}} \qquad \text{(Eq 11)}$$

where w is the barrier height for the hindered rotor (for this complex, the strength of one or two hydrogen bonds), and I is the moment of inertia for the rotation.

- *2.2.1.6 Local minima weighting*

Three local minimum geometries for the complex and two local minimum geometries for β-HEP are all accessible at room temperature. Therefore the partition function for each of these geometries contributes to the overall equilibrium constant for complex formation. The partition function for a molecule is

$$q = \sum_i e^{-\beta E_i/(kT)} \qquad \text{(Eq 12)}$$

where i denotes all of the states for the molecule. Therefore the partition functions for β-HEP-H_2O and β-HEP are equal to the sums of the partition functions for each of the local minimum geometries if they have a common reference energy. Therefore, the equilibrium constant for the complex formation is equal to

$$K_e = \frac{\dfrac{q_{[HEP-H2O]_1} + q_{[HEP-H2O]_2} + q_{[HEP-H2O]_3}}{V}}{(\dfrac{q_{[HEP]_1} + q_{[HEP]_2}}{V}) \times (\dfrac{q_{[H2O]}}{V})} \qquad \text{(Eq 13)}$$

2.2.2 Instrumentation

Figure 4 shows the principal components and layout of the experimental apparatus. The photolysis cell is 244 cm long including the end boxes (20 cm × 18 cm) used to house long-pass Herriott cell optics. The end boxes support the glass photolysis cell and are purged with nitrogen to protect optical surfaces from corrosive gases. The Pyrex cylindrical reaction tube (187 cm in length, 5.1 cm in diameter) between the end boxes constitutes the effective path length for photolysis and absorption experiments. The reaction tube is surrounded by a

Pyrex jacket through which methanol, or a glycol/water mixture is circulated for temperature regulation.

All gases are precooled or heated before entering the reaction cell by a jacketed long-path manifold that is either cooled with methanol or heated with a glycol/water mixture. K-type thermocouples placed at both ends of the cell monitor the temperature of the system. Typically, less than 1°C difference occurs between the gases entering and exiting the cell. CaF_2 windows are used at both ends of the cell to transmit both UV and IR light over the range of interest. Kinematically mounted mirrors in the optical path of the system make it possible to switch between UV and IR detection methods without changing the position and alignment of the flow cell, light sources and detectors. A purge box placed over the IR and UV optics in the path where the excimer-light and D_2-light intersect is purged with a steady flow of nitrogen to reduce production of ozone formed by photolysis of O_2 outside the cell by the excimer laser. Gas mixtures of N_2/O_2/2-chloroethanol/H_2O flow continuously through calibrated Teledyne-Hastings (HFC series) flow controllers at a total flow rate of 14,000 standard cm^3 min^{-1} (sccm). 2-chloroethanol (99% pure) was purchased from Aldrich and used without further purification. Compressed N_2 and O_2 cylinders (99%) were obtained from Airgas. Pressure was maintained at 200 Torr total pressure and measured with an MKS-Baratron 690A pressure transducer.

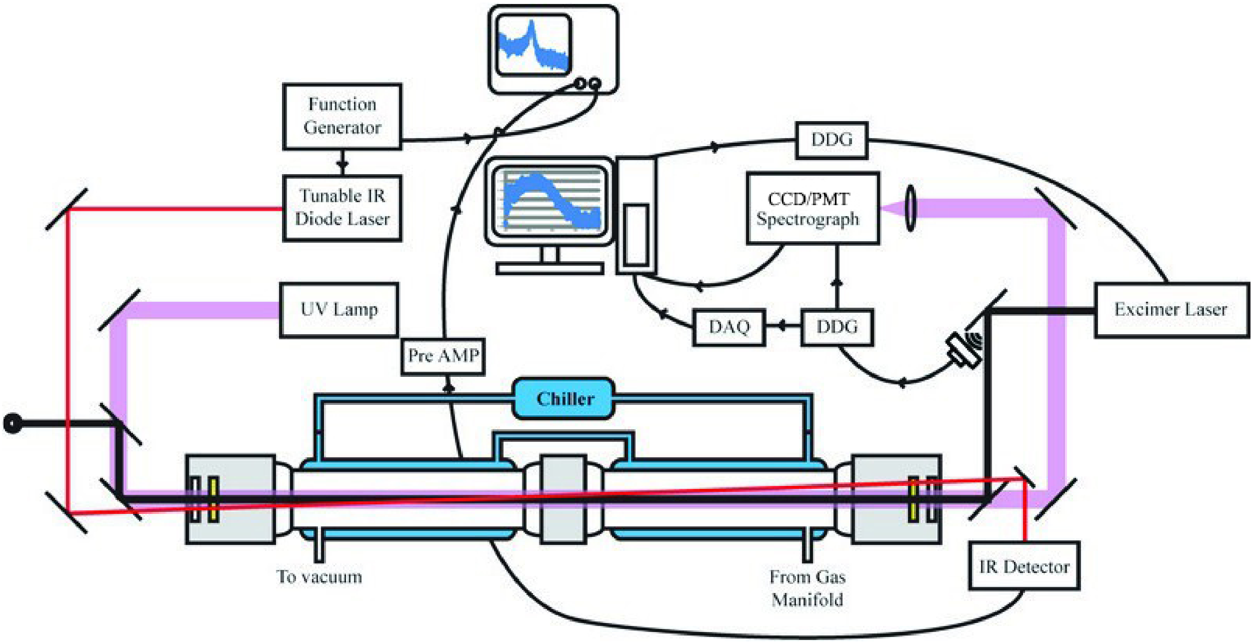

Figure 4 Schematic of UV/flash-photolysis system for kinetic measurements.

2.3. Methods

2.3.1 Radical Generation and Measurement

Flash photolysis/UV absorption spectroscopy was used to create and monitor β-HEP. β-HEP was formed in the reaction cell by introducing a gas mixture containing typically 6.1×10^{18} molecules cm^{-3} of N_2, 6.6×10^{17} molecules cm^{-3} of O_2, and $1–6\times10^{15}$ molecules cm^{-3} of 2-chloroethanol ($HOCH_2CH_2Cl$). $HOCH_2CH_2Cl$ was introduced into the gas mixture via dual 100-mL bubblers in series with N_2 at 2000 sccm as the carrier gas. The amount of $HOCH_2CH_2Cl$ is approximate, other gases were metered. Two bubblers in series provide time for carrier N_2 to be saturated with $HOCH_2CH_2Cl$. The temperature of the bubblers was maintained by immersion in a constant temperature bath maintained at 303 K through use of resistive heaters and a PID controller. Total flow rate was maintained at 14,000 sccm, resulting in a residence time of ~4 s in the reaction cell. A 15 ns pulse from the ArF excimer laser (LamdaPhysik, model EMG201MSC) at 193 nm and energy of 200 to 400 mJ pulse^{-1} photolyzes an area 2.5 cm wide by 1 cm high. The excimer was fired at 0.33 Hz, allowing for a mostly fresh (~95%) mixture of gas to be probed with every laser shot. The pulse photolyzed a small fraction of the $HOCH_2CH_2Cl$ molecules to produce $HOCH_2CH_2$ and Cl radicals.[59, 64] Subsequent reaction of $HOCH_2CH_2$ radical with O_2 produced the β-HEP radical. The initial measured concentration of β-HEP radical is 3–6×10^{13} molecules cm^{-3} depending on the concentration of $HOCH_2CH_2Cl$ and the intensity of the excimer laser pulse. Along with β-HEP formed by the cleavage of the C-Cl bond in $HOCH_2CH_2Cl$, trace amounts of derivatives of β-HEP are made by dissociation of a C-H or C-O bond in $HOCH_2CH_2Cl$. Based on the bond dissociation energies for C-H, C-O and C-Cl bonds in $HOCH_2CH_2Cl$, other peroxy radicals including $ClCH(O_2)CH_2OH$, $ClCH_2CH(O_2)COH$ and $ClCH_2CH_2O_2$ are < 0.01% of the β-HEP radical concentration.

Time-resolved detection of the β-HEP radical is done by directing the output from a 30-Watt D_2 lamp (Oriel model 60010) through the center of the reaction cell. The excimer laser photolysis beam is aligned coaxially with the UV probe beam using dielectric mirrors that reflect a 30-nm wide band centered on the 193 nm photolysis beam while passing all other UV wavelengths. UV light absorption is detected by a monochromator (Andor model SR-303i-B with a 1800 mm^{-1} or 600 mm^{-1} grating, depending on the light intensity, which decreases with decreasing wavelength in the D_2 lamp), and either an intensified and gated CCD camera (Andor model CCD30-11) or a photomultiplier tube (PMT Sens-Tech P30A-14).

The CCD was used in exploratory experiments to identify the major species present. The CCD measured absorption over a wide wavelength range, from 220 to 350 nm, enabling identification of secondary chemistry products. Absorption data at many wavelengths permits a least-squares fit to determine multiple species present in the reaction cell. Time resolved data were collected with the CCD by varying the delay from 1 to 10 ms after the excimer laser was fired. The CCD integrated a 5 μs window after the laser was fired, and 500 shots of the laser were averaged to achieve a sufficient signal-to-noise ratio. These experiments are time-consuming because measurement of a decay of β-HEP requires a minimum of 30 delay times to achieve a reproducible fit. At 0.33 Hz, 12 h are needed to obtain a single fit to the self-reaction decay.

Because of the fast response, the kinetic data for the β-HEP self-reaction reported here were collected exclusively with the PMT. The PMT together with a monochromator and notch filters with selected wavelengths of 220, 230, and 254 nm (Figure 5 adapted from previously published data[58, 65-67]) were used to collect kinetic data. The PMT collected data at 30 MHz after the excimer laser was fired. Deconvolution of species concentrations from the total absorption data collected by the PMT requires a decay curve to be collected at each of the three wavelengths. Sufficient signal to noise was obtained by averaging 300–400 shots of the excimer laser. Dark counts were recorded before each shot, and I_0 was taken as the signal prior to the next laser pulse. Collection of dark counts, blank (I_0) and response (I) was controlled through a LabVIEW routine written in-house.

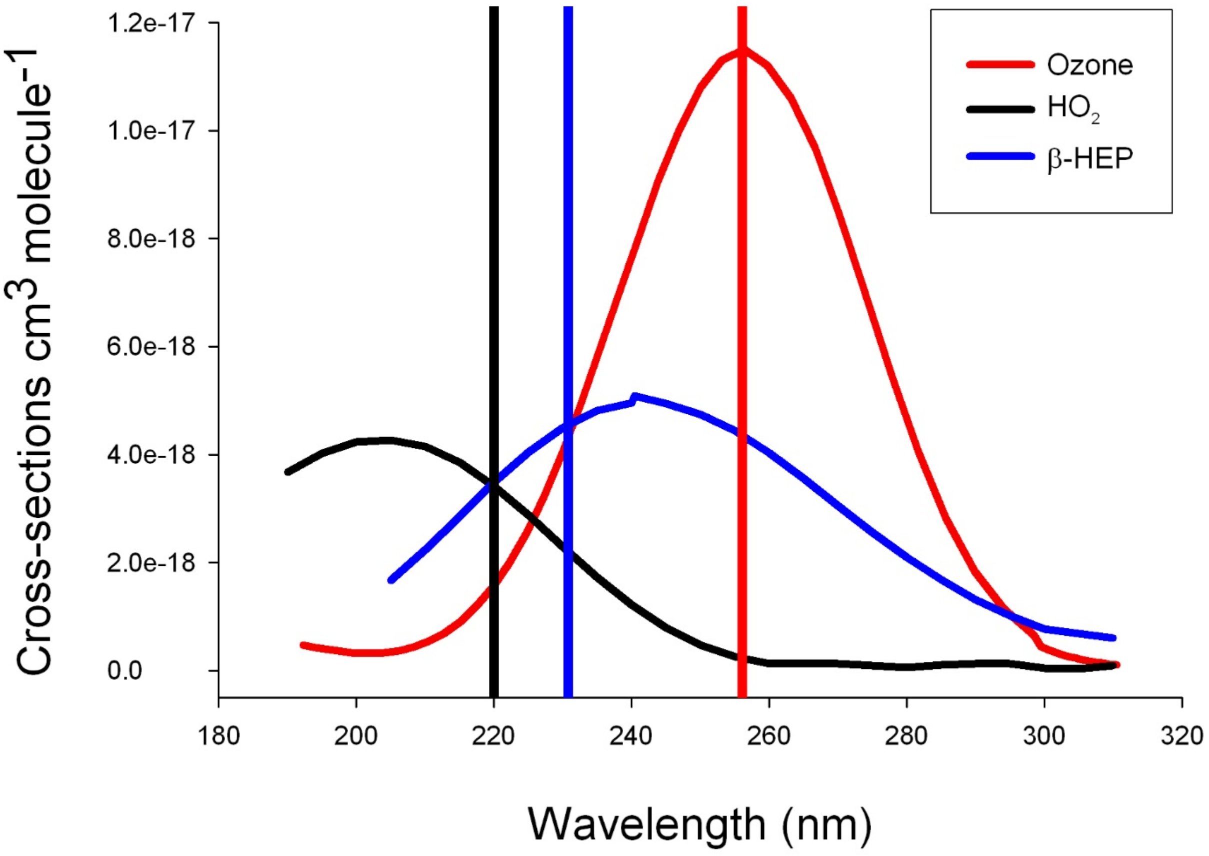

Figure 5 Plot of absorption cross sections of β-HEP, O_3, and HO_2 used to fit absorption data to obtain the concentration of each species. The bars superimposed over the plot are bandpass filters used to select the specific wavelengths used for data analysis.

After collecting decay curves at each of the three wavelengths, recommended cross sections were used from the MPI-Mainz UV-VIS spectral atlas of gaseous molecules[65] to determine concentrations of O_3, HO_2 and β-HEP by a least-squares fit (See section 2.3.4). The β-HEP self-reaction rate constants and β-HEP concentration at time zero were obtained by fitting time-dependent concentrations to a system of differential equations defined by the reactions listed in Table 1.

2.3.2 Water Vapor Generation and Measurement

Water vapor was introduced into the reaction cell by passing N_2 carrier gas through a bubbler immersed in a constant temperature bath. The amount of water vapor in the reaction cell was controlled by both the temperature of the water and the percentage of total flow of the carrier gas passing through the bubbler. The water vapor concentration was varied between 1.0×10^{15} and 2.3×10^{17} molecules cm^{-3}. Water vapor concentration was held constant during each experiment, varying no more than ±8% over the 8 h duration of an experiment.

Wavelength modulated IR diode laser spectroscopy was used to quantify the water vapor in the cell. Figure 4 shows the IR system components. IR light was scanned over a narrow frequency band (100 Hz) centered at the 6790.65 cm^{-1} line such that the entire peak of the selected rovibrational transition of water vapor was observed. The IR beam was produced by a New Focus TLB-6326 tunable diode laser with a line width of < 300 kHz. With the use of

Herriott cell optics, the IR beam was passed five times through the reaction cell and finally directed towards an IR 1-GHz low-noise photoreceiver (New Focus 1611). The signal from the detector was synchronized with the 100 Hz modulation frequency and visualized and recorded by a digital oscilloscope (TeKtronix model TDS 3024B). Data were processed and converted from absorption measurements to concentrations with a LabVIEW routine. Absorption line strengths were obtained from the HITRAN[68] database and converted to cross sections.

Table 1 Reactions used to fit β-HEP decays to obtain the self-reaction rate constant.

#	**Reaction**	***k*(cm³ molecule⁻¹ s⁻¹)**	**% difference in k_{obs} & *k'***	**Ref #**
1.1	$HOCH_2CH_2O_2 + HOCH_2CH_2O_2 \rightarrow 2\ HOCH_2CH_2O + O_2$	from fit	0	--
1.2	$HOCH_2CH_2O_2 + HOCH_2CH_2O_2 \rightarrow HOCH_2CH_2OH + HOCH_2CHO + O_2$	from fit	0	--
1.3	$HOCH_2CH_2O_2 + HO_2 \rightarrow HOCH_2CH_2OOH + O_2$	1.0×10^{-11}	0	36
1.4	$HOCH_2CH_2O + O_2 \rightarrow HOCH_2CHO + HO_2$	$5.0 \times 10^{-26}\ e^{(-34.92\ kJ/RT)}$	0	38
1.5	$HO_2 + HO_2 \rightarrow H_2O_2 + O_2$	$2.2 \times 10^{-13}\ e^{(4.99\ kJ/RT)}$	0	38
1.6	$HOCH_2 + O_2 \rightarrow CH_2O + HO_2$	9.6×10^{-12}	0	25
1.7	$HO_2 + O_3 \rightarrow HO + 2O_2$	$1.1 \times 10^{-14}\ e^{(-4.16\ kJ/RT)}$	0	13
1.8	$HO_2 + Cl \rightarrow O_2 + HCl$	$1.8 \times 10^{-11}\ e^{(-1.41\ kJ/RT)}$	0	13
1.9	$Cl + O_3 \rightarrow ClO + O_2$	$2.8 \times 10^{-11}\ e^{(-2.80\ kJ/RT)}$	±1.1	13
1.10	$O + O_2 \rightarrow O_3$	2.81×10^{-12}	±0.3	13
1.11	$Cl + ClCH_2CH_2OH \rightarrow OHCH_2CH_2O_2 + HCl$	3.08×10^{-11}	±0.9	38*
1.12	$Cl + ClCH_2CH_2OH \rightarrow HO_2 + HCl + CH_3CHO$	3.08×10^{-11}	±0.2	38*
1.13	$HO_2 + OH \rightarrow H_2O + O_2$	$4.8 \times 10^{-11}\ e^{(2.08\ kJ/RT)}$	0	13
1.14	$OH + O \rightarrow O_2 + H$	3.59×10^{-11}	0	13
1.15	$Cl + Cl \rightarrow Cl_2$	1.46×10^{-13}	0	13
1.16	$O + HO_2 \rightarrow OH + O_2$	5.8×10^{-11}	0	13
1.17	$OH + ClO \rightarrow ClOOH$	1.46×10^{-11}	0	38
1.18	$H + O_2 + M \rightarrow HO_2 + M$	5.4×10^{-32}	0	38
1.19	$H + O_3 \rightarrow OH + O_2$	2.84×10^{-11}	0	38
1.20	$Cl + O_2 \rightarrow ClOO$	9.11×10^{-15}	0	13

2.3.3 β*-HEP Self-Reaction Kinetics Measurement*

The experimental set-up was tested and calibrated by measuring the β–HEP self-reaction rate in the absence of water vapor. The dry rate constant measured was (2.25±0.15) × 10^{-12} cm^3 $molecule^{-1}$ s^{-1} at 296 K, which is within the experimental uncertainity of the recommended NIST evaluation value, $(2.31 \pm 0.3)\times10^{-12}$ cm^3 $molecule^{-1}$ s^{-1} (see Figure 6)

The self-reaction of β-HEP follows two product branches, reactions 2.1 and 2.2

$$HOCH_2CH_2O_2 + HOCH_2CH_2O_2 \overset{k1}{\rightarrow} 2\ HOCH_2CH_2O + O_2 \qquad (2.1)$$

$$HOCH_2CH_2O_2 + HOCH_2CH_2O_2 \overset{k2}{\rightarrow} HOCH_2CH_2OH + HOCH_2CHO + O_2 \qquad (2.2)$$

The overall loss of β-HEP from both reactions was measured in these experiments. The observed rate constant, k_{obs}, is the overall rate constant representing the following four elementary reactions:

$$HOCH_2CH_2O_2 + HOCH_2CH_2O_2 \overset{k3}{\rightarrow} \text{Products} \qquad (2.3)$$

$$HOCH_2CH_2O_2 + H_2O = HOCH_2CH_2O_2\text{-}H_2O \qquad (2.4)$$

$$HOCH_2CH_2O_2\text{-}H_2O + HOCH_2CH_2O_2 \overset{k5}{\rightarrow} \text{Products} \qquad (2.5)$$

$$HOCH_2CH_2O_2\text{-}H_2O + HOCH_2CH_2O_2\text{-}H_2O \overset{k6}{\rightarrow} \text{Products} \qquad (2.6)$$

193 nm light was used to initiate production of β-HEP, but O_2 is also photolyzed to form singlet oxygen atoms that combine with O_2 to form ozone. The absorption cross section of ozone overlaps strongly with the cross section of β-HEP and HO_2 (Figure 5)(postulated to be formed due to undesirable secondary chemistry), causing an interference with direct absorption measurements. However, O_2 could not be excluded from the reaction gas mixture because O_2 is essential for the production of β-HEP and is used to convert $HOCH_2CH_2$ to β-HEP. Smaller flow rates of O_2 into the reaction mixture lengthened the conversion time of $HOCH_2CH_2$ into β-HEP, and unwanted secondary chemistry of $HOCH_2CH_2$ increased. Higher concentrations of O_2 in the reaction cell led to increased production of O_3 that complicated the analysis due to the overlapping absorption spectrum of O_3 with β-HEP. To reduce ozone formation and minimize unknown chemistry between $O(^1D)$ radicals and other species while still producing β-HEP in less than 30 μs, the O_2 concentration was decreased until the β-HEP concentration was 3-6 times the detection limit. The ozone concentration was between $3\text{-}5 \times 10^{16}$ molecules cm^{-3} in the experiment.

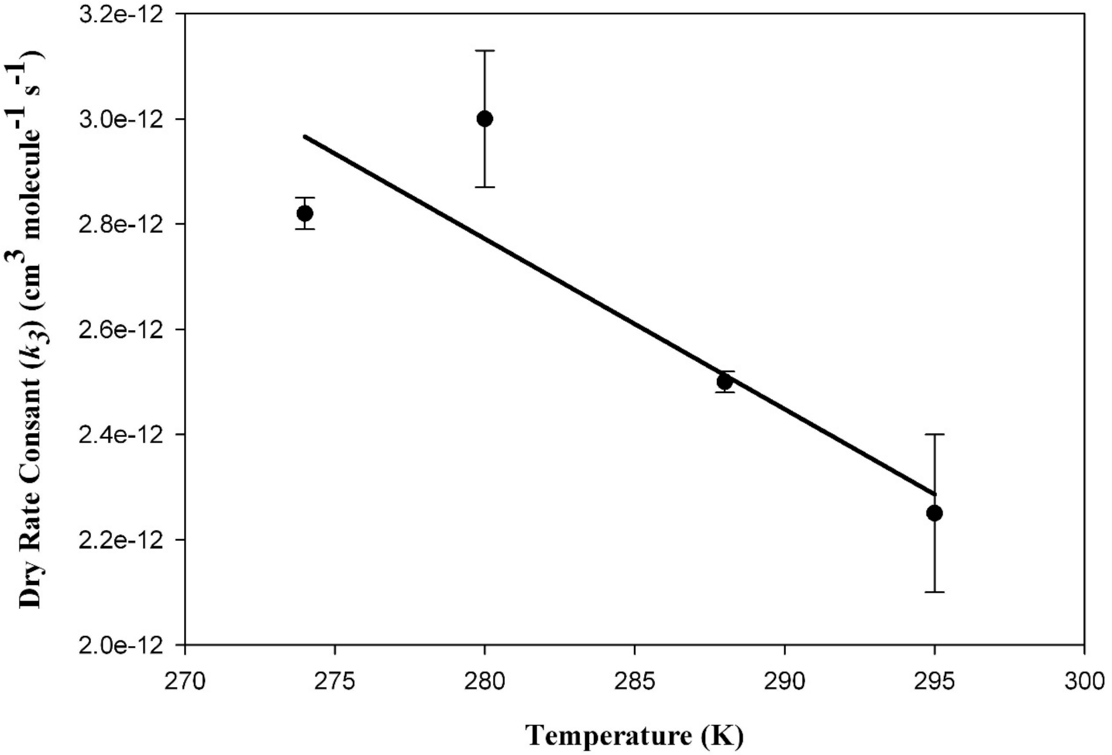

Figure 6 Comparison of the measured β-HEP self-reaction rate constant in the absence of water vapor as a function of temperature with the Atkinson et al.[61] (NIST) published values. NIST values represented as solid line in the figure.

Detection of β-HEP decays was begun 1 ms after the photolysis laser fired because residual reflections from the photolysis pulse interfered with detection by the PMT. Because photolysis of $HOCH_2CH_2Cl$ can form HO_2,[27, 61, 69-70] absorption of HO_2 was also considered. Three collection wavelengths at 220, 230, and 254 nm provide sufficient data for a least-squares fit to obtain the concentrations of O_3, HO_2, and β-HEP (see section 2.3.4 for the equations used for the least squares fit and Figure 7A and 7B for typical decay curves). At each condition, multiple decay curves were measured until k_{obs} was within the 95% confidence interval of the mean.

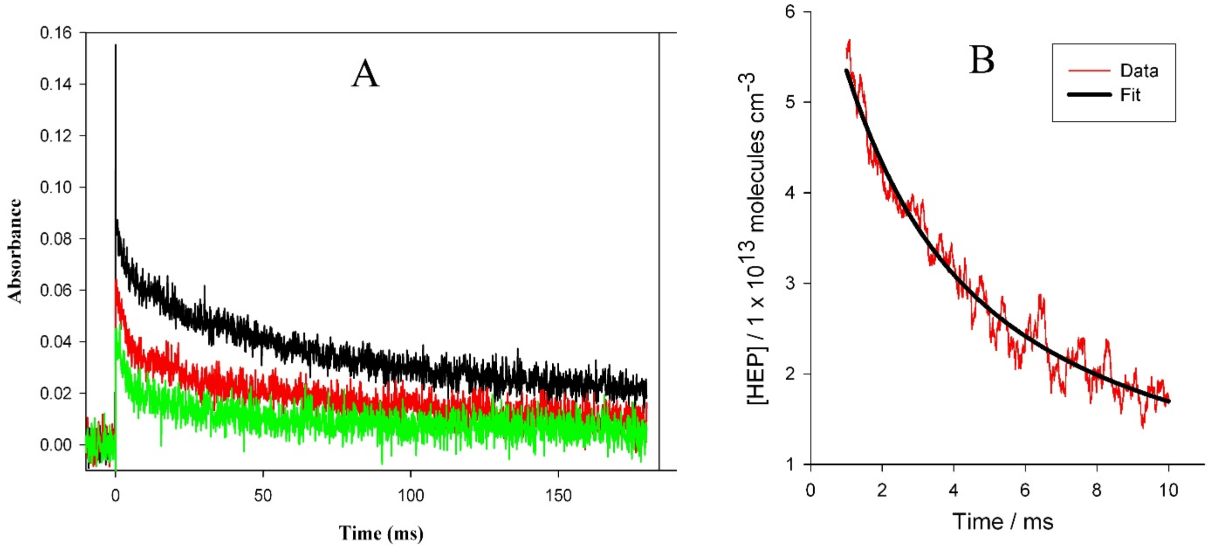

Figure 7 (A) Representative data collected at the three wavelengths (nm) 220 (green), 230 (red), and 254 (black). (B) A typical fit to the measured decay.

Typically, 9 to 34 β-HEP decay curves were collected at different initial β-HEP concentrations at each water vapor and temperature condition. The HO_2 concentration was always found to be below the detection limit (~1 × 10^{13} molecules cm^{-3})(i.e. the detection limit of the CCD and PMT was 0.006 absorbance units, therefore the detection limit for [HO_2] at 220nm=[0.006 ÷ (3.16×10^{-18} cm^2/molecule × 187 cm)]=1×10^{13} molecule/cm^3), and thus the least-squares fit was reduced to a two-parameter least-squares fit (Eqn 14) Derivation of Equation 14 is shown below.

$$A_x = b\,(\sigma_x^{O_3}[O_3] + \sigma_x^{\beta-HEP}[\beta - HEP]) \qquad \text{(Eqn 14)}$$

were b=pathlength, σ=cross section, A=absorbance and x=220, 234 and 254nm.

2.3.4 Derivation of Equation 14

From the Beer-Lambert Law, where b is pathlength, σ is absorption cross section, and [ ] indicates concentrations

$$A_{220} = b\begin{pmatrix}\sigma_{220}^{O_3}[O_3] + \sigma_{220}^{HO_2}[HO_2] + \sigma_{220}^{\beta-HEP}[\beta - HEP] + \\ \sigma_{220}^{\beta-HEP-H_2O}[\beta - HEP - H_2O]\end{pmatrix}$$

(Eqn 15)

$$A_{230} = b\begin{pmatrix}\sigma_{230}^{O_3}[O_3] + \sigma_{230}^{HO_2}[HO_2] + \sigma_{230}^{\beta-HEP}[\beta - HEP] + \\ \sigma_{230}^{\beta-HEP-H_2O}[\beta - HEP - H_2O]\end{pmatrix}$$

(Eqn 16)

$$A_{254} = b\begin{pmatrix}\sigma_{254}^{O_3}[O_3] + \sigma_{254}^{HO_2}[HO_2] + \sigma_{254}^{\beta-HEP}[\beta - HEP] + \\ \sigma_{254}^{\beta-HEP-H_2O}[\beta - HEP - H_2O]\end{pmatrix}$$

(Eqn 17)

Since the cross section of the β-HEP-H_2O complex is unknown, we assume

$$\sigma_x^{\beta-HEP-H_2O} = f_x\,\sigma_x^{\beta-HEP} \qquad \text{(Eqn 18)}$$

Where $f_x \geq 0$ and $x = 200 - 400$ nm.

Substituting Equation 18 into the last two terms of equation Eqn 15, 16 and 17 yields,

$$\begin{matrix} \sigma_x^{\beta-HEP}[\beta - HEP] + \\ \sigma_x^{\beta-HEP-H_2O}[\beta - HEP - H_2O] \end{matrix} = \sigma_x^{\beta-HEP}[\beta - HEP] + f_x\,\sigma_x^{\beta-HEP}[\beta - HEP - H_2O]$$

(Eqn 19)

The equilibrium constant for the formation of the β-HEP-H_2O complex is,

$$K = \frac{[\beta - HEP - H_2O]}{[\beta - HEP][H_2O]}$$

Solving for β-HEP-H_2O gives,

$$[\beta - HEP - H_2O] = K[\beta - HEP][H_2O]$$

(Eqn 20)

Substituting Equation Eqn 20 into Eqn 19 yields,

$$\begin{matrix} \sigma_x^{\beta-HEP}[\beta - HEP] + \\ \sigma_x^{\beta-HEP-H_2O}[\beta - HEP - H_2O] \end{matrix} = \sigma_x^{\beta-HEP}[\beta - HEP] + f_x K \sigma_x^{\beta-HEP}[\beta - HEP][H_2O]$$

(Eqn 21)

Factoring out $\sigma_x^{\beta-HEP}[\beta - HEP]$ yields Equation 22

$$\begin{matrix} \sigma_x^{\beta-HEP}[\beta - HEP] + \\ \sigma_x^{\beta-HEP-H_2O}[\beta - HEP - H_2O] \end{matrix} = \sigma_x^{\beta-HEP}[\beta - HEP][1 + f_x K[H_2O]]$$

(Eqn 22)

Thus the equations for absorbance at 220, 230 and 254 reduce to,

$$A_{220} = b\left(\sigma_{220}^{O_3}[O_3] + \sigma_{220}^{HO_2}[HO_2] + \sigma_{220}^{\beta-HEP}[\beta - HEP]\{1 + f_{220}K[H_2O]\}\right)$$

(Eqn 23)

$$A_{230} = b\left(\sigma_{230}^{O_3}[O_3] + \sigma_{230}^{HO_2}[HO_2] + \sigma_{230}^{\beta-HEP}[\beta - HEP]\{1 + f_{230}K[H_2O]\}\right)$$

(Eqn 24)

$$A_{254} = b\left(\sigma_{254}^{O_3}[O_3] + \sigma_{254}^{HO_2}[HO_2] + \sigma_{254}^{\beta-HEP}[\beta - HEP]\{1 + f_{254}K[H_2O]\}\right)$$

(Eqn 25)

If, $0 \leq f_{220}, f_{230}, f_{254} \leq 10$, the product of $f_{220}K[H_2O], f_{230}K[H_2O], f_{254}K[H_2O] \approx 0$. Thus the observed β-HEP concentration in this experiment is,

$$[\beta - HEP]_{observed} = [\beta - HEP][1 + f_xK[H_2O]] \approx [\beta - HEP]$$

(Eqn 26)

If f_x=0, the two cross sections do not overlap and the observed signal in this experiment is only due to β-HEP. If $f_x > 0$ there is an overlap between the two cross sections and the observed signal in this experiment is due to both β-HEP and β-HEP-H_2O complex. In either case, the equations to solve for the concentrations of ozone, β-HEP and HO_2 reduce to

$$A_{220} = b\left(\sigma_{220}^{O_3}[O_3] + \sigma_{220}^{HO_2}[HO_2] + \sigma_{220}^{\beta-HEP}[\beta - HEP]\right)$$

(Eqn 27)

$$A_{230} = b\left(\sigma_{230}^{O_3}[O_3] + \sigma_{230}^{HO_2}[HO_2] + \sigma_{230}^{\beta-HEP}[\beta - HEP]\right)$$

(Eqn 28)

$$A_{254} = b\left(\sigma_{254}^{O_3}[O_3] + \sigma_{254}^{HO_2}[HO_2] + \sigma_{254}^{\beta-HEP}[\beta - HEP]\right)$$

(Eqn 29)

The HO_2 concentration calculated by solving equation Eqn 27, 28, 29 was always below our detection limit of 1×10^{13} molecules/cm^3. Thus the general form of the measured absorbance is given by Equation 14.

$$A_x = b\,(\sigma_x^{O_3}[O_3] + \sigma_x^{\beta-HEP}[\beta - HEP])$$

(Eqn 14)

2.4 Results

2.4.1 β-HEP Self-Reaction Kinetics

Each curve was fit to a model composed of coupled differential equations describing the reactions given in Table 1. Measured time-dependent concentrations of β-HEP, and calculated concentrations (using the photon flux and quantum yields of O_2 and H_2O photolysis) of oxygen atoms, hydrogen atoms and hydroxy radicals are inputs to the model. The outputs are concentration of β-HEP at time 0, the observed self-reaction rate of β-HEP (k_{obs}), and the HO_2 concentration. Table 2 presents the results of all experiments with 95% confidence intervals for [H_2O], [β-HEP]$_0$, and k_{obs} at 274

K, 280 K, 288 K, and 296 K. Figure 7a shows representative decays collected at 220, 230 and 254 nm. Figure 7b is a typical fit to the measured β-HEP decay. The total experimental error in k_{obs} ranges from 4 to 10% depending on experimental temperature and concentrations of O_3 and water vapor. This error could be reduced by decreasing the amount of O_2 in the cell, but, as noted previously, reducing oxygen would not produce sufficient β-HEP.

Sensitivity of the kinetic model was done to determine the effects of uncertainities in the rate constants on fiting k_{obs}. The rate constants were changed individually by ±30%, and the measured β-HEP decay curves were fit to obtain an adjusted value for k_{obs}, i.e. k'. This k' was compared against the k_{obs} obtained from the fit of the experimental data with the original model. These results are listed in Table 1 as the percent difference between k_{obs} and k'. For example, a 30% change in the rate constant of the O_3 + Cl reaction leads to a 1% change in calculated k_{obs}. The uncertainty in k_{obs} caused by uncertainities in the reactions of the model is estimated to be 2.5% (see Table 1). The sensitivity analysis shows that secondary chemistry is dominated by reactions involving O_3 and Cl radicals.

Table 2 β-HEP rate constants as a function of H_2O vapor concentration.

Temperature in K	$[H_2O]$ molecules cm^{-3}/ 1× 10^{16}	k_{obs} (fit) cm^3 $molecule^{-1}$ $s^{-1}/1\times10^{-12}$	[β-HEP]$_0$ molecules $cm^{-3}/1\times10^{13}$	k_3 (measured) $cm^3 molecule^{-1}$ $s^{-1}/1\times10^{-12}$	# of Trails
274	0.18 ± 0.08	3.77 ± 0.28	3.4 ± 0.1	2.82 ± 0.03	21
	1.57 ± 0.14	6.04 ± 0.48	4.5 ± 0.2		12
	2.60 ± 0.13	8.14 ± 0.68	3.1 ± 0.2		9
	3.32 ± 0.33	8.54 ± 0.71	2.9 ± 0.1		10
280	0.29 ± 0.13	4.16 ± 0.50	3.4 ± 0.2	3.00 ± 0.13	17
	2.10 ± 0.08	5.36 ± 0.42	4.0 ± 0.3		13
	4.70 ± 0.25	5.70 ± 0.50	2.9 ± 0.2		14
	5.86 ± 0.16	6.88 ± 0.67	3.6 ± 0.6		12
	6.76 ± 0.23	8.47 ± 0.97	3.1 ± 0.3		9
288	0.20 ± 0.05	3.38 ± 0.17	3.9 ± 0.1	2.5 ± 0.02	24
	3.80 ± 0.10	4.09 ± 0.28	4.1 ± 0.7		10
	8.21 ± 0.29	4.94 ± 0.28	4.7 ± 0.9		12
	12.20 ± 0.07	6.20 ± 0.57	5.0 ± 0.6		16
295	0.18 ± 0.05	2.92 ± 0.18	3.1 ± 0.1	2.25 ± 0.15	34
	6.26 ± 0.20	3.67 ± 0.45	5.1 ± 0.3		16
	11.80 ± 0.03	3.34 ± 0.46	5.3 ± 0.2		10
	22.50 ± 0.07	4.16 ± 0.14	5.9 ± 0.3		12

In their HO_2 and HO_2-H_2O study, Cox and Burrows,[21] Kircher and Sander,[24] and Lii *et al*[25] applied the assumption that HO_2 and complex absorption cross sections are not resolveable in the UV. But Aliosio *et al,*[71] showed that the complex cross section in the UV is red shifted by 59nm, which contradicts above assumption. Therefore, in this study, we account for both complex and β-HEP cross section by assuming the following relationship,

$$\sigma_x^{\beta-HEP-H_2O} = f_x\,\sigma_x^{\beta-HEP} \qquad \text{(Eqn 18)}$$

where x = 220, 230 and 254 and $f_x \geq 0$.

An expression that describes the water vapor dependence of the β-HEP self-reaction must include the reactions of β-HEP with both β-HEP and β-HEP-H_2O and the reaction of β-HEP-H_2O with β-HEP-H_2O. A reduced form of the rate law is

$$k_{obs} = k_3 + k_5K[H_2O] \qquad \text{(Eqn 30)}$$

where k_3 and k_5 are rate constants for reactions 2.3 and 2.5 respectively, and K is the equilibrium constant for reaction 2.4 (See the following Section for a derivation of Equation 30). The same expression has previously been used to describe water vapor enhancement of the HO_2 self reaction.

Derivation of Equation 30

To derive Equation 30, we define the following variables (only for this section)

Concentration of un-complexed [β-HEP] = $[u]$

Concentration of complexed β-HEP [β-HEP-H_2O] = $[c]$

Concentration of observed β-HEP = $[o]$

Concentration of water = $[w]$

Observed rate constant = k_o

From elementary reactions 2.3 and 2.5, the rate of loss of un-complexed β-HEP is given by

$$\frac{d[u]}{dt} = -2k_3[u]^2 - k_5[u][c]$$

(Eqn 31)

From elementary reactions 2.5 and 2.6, the rate of loss of β-HEP-H_2O is given by

$$\frac{d[c]}{dt} = -k_5[u][c] - 2k_6[c]^2$$

(Eqn 32)

To obtain k_3,k_5 *and* k_6 as functions of k_o we introduce the relationship,

$$\frac{d[o]}{dt} = -2k_o[o]^2$$

(Eqn 33)

Substituting equation 26 (the observed concentration of β-HEP in our experiment) in equation 33 yields,

$$\frac{d[o]}{dt} = -2k_o([u][1 + fK[w])^2$$

$$= -2k_o[u]^2([1 + fK[w])^2$$

(Eqn 34)

Adding Equations 31 and 32 gives the theoretically observed loss of β-HEP in this experiment

$$\frac{d[o]}{dt} = \frac{d[u]}{dt} + \frac{d[c]}{dt} = -2k_3[u]^2 - 2k_5[u][c] - 2k_6[c]^2$$

(Eqn 35)

Equating 34 and 35 gives,

$$-2k_o[u]^2([1 + fK[w])^2 = -2k_3[u]^2 - 2k_5[u][c] - 2k_6[c]^2$$ (Eqn 36)

The equilibrium constant for complex formation is given by

$$K = \frac{[c]}{[u][w]}$$

Thus, $$[c] = K[u][w]$$ (Eqn 37)

Substituting Equation 37 into Equation 36 gives,

$$-2k_o[u]^2([1+fK[w])^2 = -2k_3[u]^2 - 2k_5[u]^2K[w] - 2k_6[u]^2[w]^2K^2$$

(Eqn 38)

Dividing Equation 38 by -2$[u]^2$ on both sides yields,

$$k_o([1+fK[w])^2 = k_3 + k_5[u]K[w] + k_6[u]^2[w]^2K^2$$

Solving for k_o gives,

$$k_o = \frac{k_3 + k_5[u]K[w] + k_6[u]^2[w]^2K^2}{([1+fK[w])^2}$$

(Eqn 39)

From calculated values of the equilibrium constant (Figure 9) and the slopes of the experimental data (Figure 8), $k_6[u]^2[w]^2K^2 << k_3 + k_5[u]K[w]$. Further within the uncertainty, there is no evidence for curvature in data in Figure 8.

Also, if $f = 1$ the cross section of β-HEP and the complex are equal then $1 + fK[w] \approx 1$. If $f = 0$ the cross section of β-HEP and the complex are distinguishable, then $1 + fK[w] = 1$. In either case Equation 39 reduces to Equation 30 in the manuscript as,

$$k_o = k_3 + k_5K[w] \qquad \text{(Eqn 30)}$$

Rearranging Eqn 30 gives,

$$k_o = k_3\{1 + \frac{k_5}{k_3} K\,[w]\}$$

(Eqn 39)

From the Arrhenius expression for the temperature dependence of the rate coefficients and van't Hoff equation for the temperature dependence of the equilibrium constant,

$$k_3 = A_3 e^{\left(\frac{-E_3}{RT}\right)} \qquad \text{(Eqn 40a)}$$

$$k_5 = A_5 e^{\left(\frac{-E_5}{RT}\right)} \qquad \text{(Eqn 40b)}$$

$$K = C * e^{\left(\frac{-\Delta H}{RT}\right)} \qquad \text{(Eqn 40c)}$$

Substituting 40a, 40b, 40c into Equation 39 gives,

$$k_o = k_3\{1 + \frac{A_5 e^{\left(\frac{-E_5}{RT}\right)}}{A_3 e^{\left(\frac{-E_3}{RT}\right)}} C e^{\left(\frac{-\Delta H}{RT}\right)}[w]\}$$

$$k_o = k_3\{1 + \frac{A_5 * C}{A_3} e^{\left(\frac{-(\Delta H + E_5 - E_3)}{RT}\right)}[w]\}$$

(Eqn 41)

Combining parameters, $A_5C/A_3 = A$ and $(E_5+\Delta H-E_3) = E$ reduces Equation 41 to Equation 42.

$$k_o = k_3\,\{1 + Ae^{(\frac{-E}{RT})}[w]\} \qquad \text{(Eqn 42)}$$

Equation 42, which is a functional form of equation 30 was used to obtain the temperature dependence of k_{obs}. The measured k_{obs} were fit with Equation 42, which includes the contribution from the dry rate constant (k_3), the water vapor dependence, and the temperature dependence of the product, k_5K. Fits to the data in Figure 8 with Equation 42 are shown as solid lines. The enhancement from water vapor in Equation 42 is taken from the data collected in this work. The dry rate constant (k_3) values from this work are at 4 different temperatures only, therefore we have used the dry rate constant equation from Atkinson's (NIST) evaluation[61] of all previously available data on dry rates. Our data agree with the NIST evaluation (see Figure 6). Kircher[24] included a pressure dependent term in the model for the HO_2 self-reaction but no data for the pressure dependence of the β-HEP self-reaction is currently available. The best fit to the data in Figure 8 yields the following rate expression:

$$k_{obs}(T,[H_2O]) = 7.8\times10^{-14}\,\exp\left((8.3\pm2.5kJ/mol)/\mathrm{R}T\right)\times\left\{1+(1.7\pm0.2)\times10^{-30}\times[H_2O]\times\exp\left((71\pm17kJ/mol)/\mathrm{R}T\right)\right\}$$

$$= 7.8\times10^{-14}\times\exp\left((8.3\pm2.5\mathrm{kJ/mol})/\mathrm{RT}\right)+(13.2\pm1.56)\times10^{-44}\times\exp\left((79.3\pm17.18\mathrm{kJ/mol})/\mathrm{RT}\right)\times[\mathrm{H_2O}]$$

(Eqn 43)

In their investigation of the kinetics of the HO_2 + HO_2-H_2O reaction, Kanno *et al.*[47] measured *K* and the rate constants independently. In this study, the product of *K* and k_5 is defined by the slopes of plots of k_{obs} vs [H_2O] at each temperature (see Equation 30 and Figure 8), and *K* and *k*$_5$ are inseparable from the data collected. Therefore, the equilibrium constant for the formation of the β-HEP-H_2O complex (*K*) was estimated from *ab initio* calculations, as described previously in the computational method section 2.1. The calculated *K* values as a function of temperature are given in Figure 9. The dashed lines around *K* in figure 9 are the uncertainty limits in K assuming an uncertainty in β-HEP-H_2O complex binding energy of ±6.3 kJ mol^{-1}.

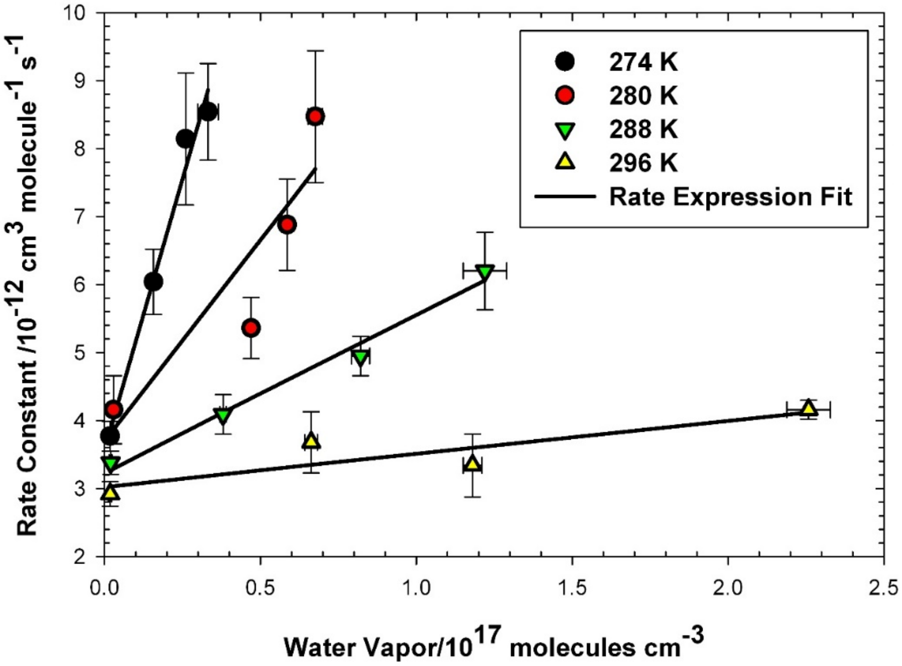

Figure 8 Observed rate constant (k_{obs}) for self-reaction of β-HEP versus water vapor concentration. The lines represent the fit to the rate expression (Eqn 43) describing the rate as a function of both water vapor concentration and temperature.

Dividing the slopes (k_5K) of the fits in Figure 8 by the calculated *K* yields k_5 values as shown in Figure 9. The uncertainty in *K* propogates into the calculation of k_5, shown as dashed lines in Figure 9. Since the calculated k_5 values cannot be larger than the hard sphere collision rate constant shown by the solid line in Figure 9, the calculated K values must be too small. Thus, the true K values must be near the upper uncertainty limit, and consequently, the k_5 values must be near the lower uncertainty limit in Figure 9. Kanno *et al.*[72] also found the *ab initio* calculated K values for the HO_2-H_2O complex to be an order of magnitude smaller than their experimentally determined K values. This Suggest that *ab initio* calulated values of K may in general be an order of magnitude smaller than measured values of K for formation of radical-water complexes. In any case, the rate constant for β-HEP + β-HEP-H_2O (k_5) is 1 to 3 orders of magnitude larger than that for β-HEP + β-HEP (See figure 8). To better estimate the effects of water vapor on the β-HEP self-reaction, the equilibrium consatnt K needs to be determined experimentally, but this is beyond the scope of this paper.

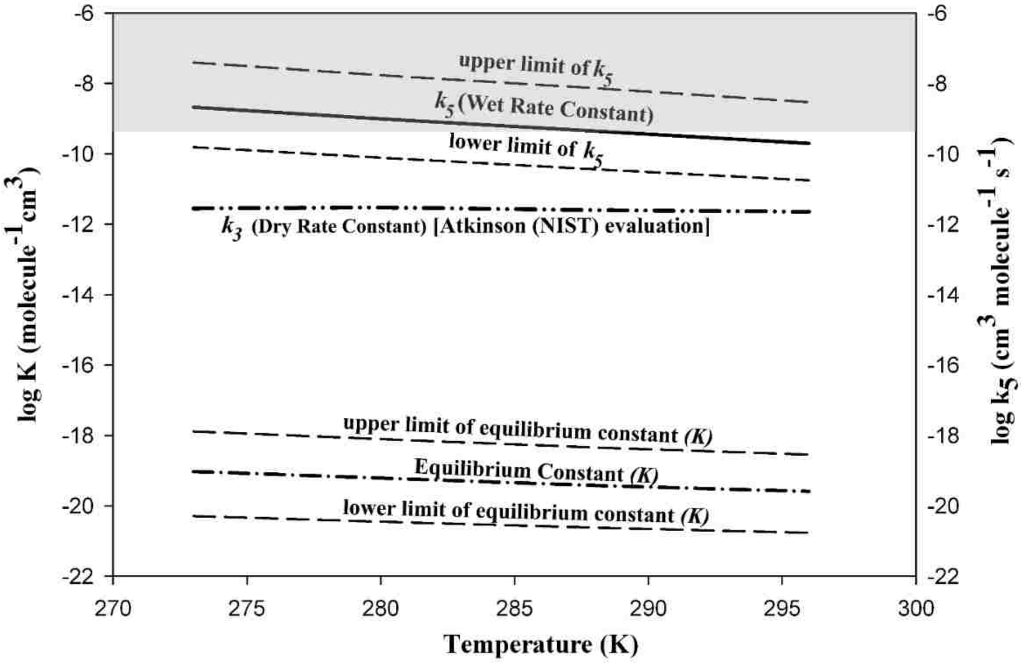

Figure 9 Effect of temperature on *K* and wet rate constant *k*5. The solid line(—) represents the change in the wet rate constant *k*5, and the dotted line (—•–) represents the change in *K*. The dashed lines represent the uncertainty in *K* and *k*5. The highlighted area represents the range of *k*5 values limited by the hard sphere collision rate constant. Atkinson (NIST) evaluation[61] for the dry rate constant (-⋯-) as a function of temperature.

2.4.2 HO_2 Production and Secondary Chemistry

The formation of some HO_2 and Cl radicals in our experiments is inevitable. Determining the concentration of HO_2 and the secondary chemistry occuring due to HO_2 and Cl radicals is thus necessary. $HOCH_2CH_2Cl$ has 3 non-equivalent hydrogen atoms, abstraction of either alcohol hydrogen or a hydrogen alpha to the OH group leads to production of HO_2.

Extraction of the alcohol hydrogen from $HOCH_2CH_2Cl$ followed by reaction with O_2 leads to HO_2 formation via the following reactions:

$$HOCH_2CH_2Cl + Cl \rightarrow OCH_2CH_2Cl + HCl \quad (2.7)$$

$$OCH_2CH_2Cl + O_2 \rightarrow HO_2 + ClCH_2CHO \quad (2.8)$$

The fate of the OCH_2CH_2Cl radical has not been investigated in the presence of oxygen, but reactivity of the analogous OCH_2CH_3 radical in air has been reported by Atkinson *et al*[61]. They reported a rate constant of 1.1×10^{-14} cm^3 $molecule^{-1}$ s^{-1} for extraction of the alpha hydrogen by molecular oxygen.

Extraction of an alpha hydrogen by a Cl atom followed by reaction with molecular oxygen also produces HO_2 radical via the following reactions:

$$HOCH_2CH_2Cl + Cl \rightarrow HOCHCH_2Cl + HCl \quad (2.9)$$

$$HOCHCH_2Cl + O_2 \rightarrow HO_2 + ClCH_2CHO \quad (2.10)$$

Attack of a chlorine atom at a beta hydrogen produces 2-chloro-hydroxyethyl peroxy radical.

$$HOCH_2CH_2Cl + Cl \rightarrow HOCH_2CHCl + HCl \quad (2.11)$$

$$HOCH_2CHCl + O_2 \rightarrow HOCH_2CH(O_2)Cl \quad (2.12)$$

To address the question of the relative significance of these reactions, the product branching ratio for extraction of the alcohol, alpha and beta hydrogen was calculated using high level *ab initio* calculations. A slice of the potential energy surface (PES) is included Figure 10.

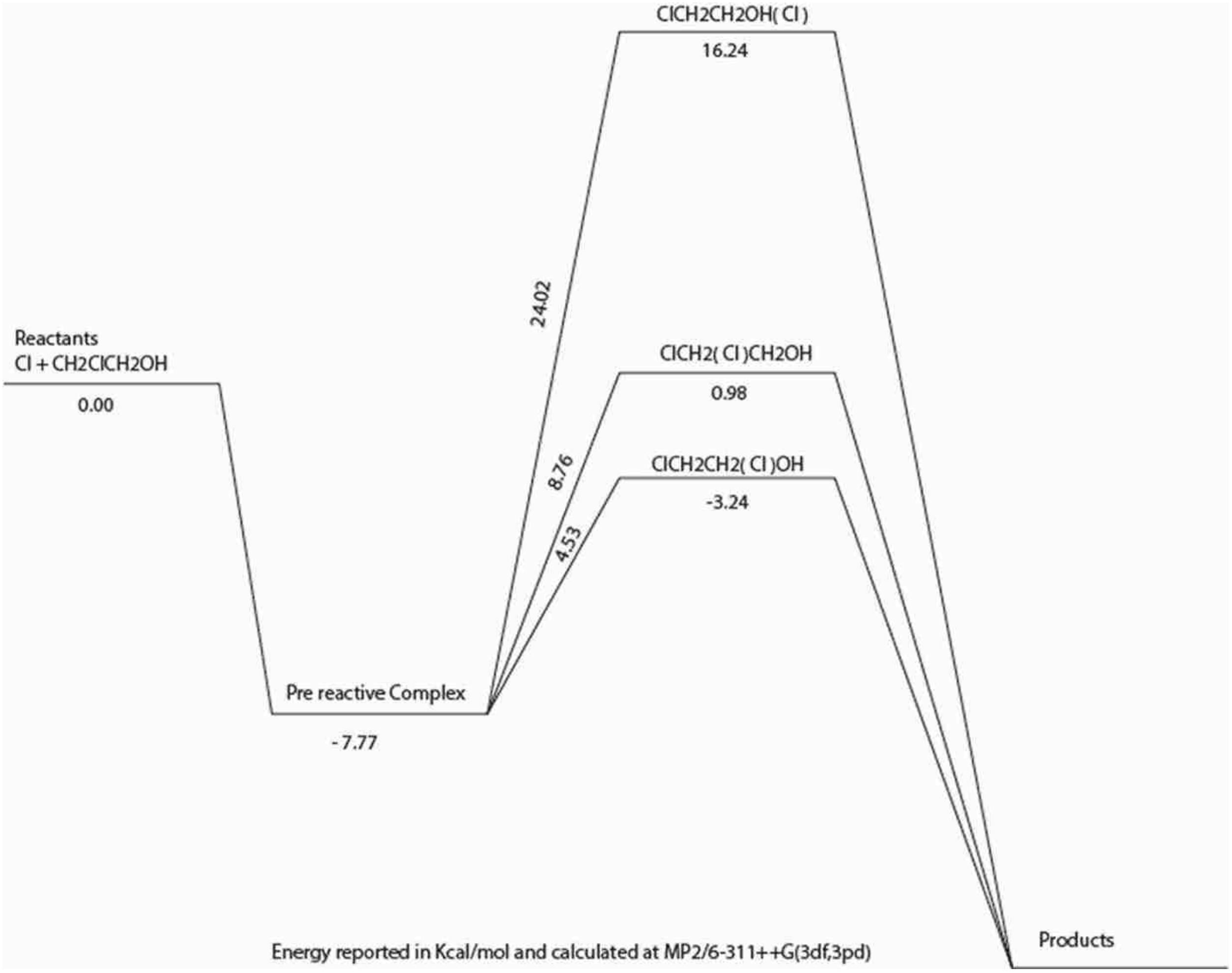

Figure 10 A slice of PES of Cl + $ClCH_2CH_2OH$ reaction for a hydrogen abstraction.

Extraction of an alpha hydrogen from $HOCH_2CH_2Cl$ has the lowest energy barrier (19 kJ mol^{-1}) followed in energy by extraction of the beta hydrogen (37 kJ mol^{-1}) and finally the alcohol hydrogen (100 kJ mol^{-1}). The product branching ratio and the rate constant reported by Garzon *et al*[73] and Taatjes et al[74] for Cl + $HOCH_2CH_3$ were used as a surrogate for Cl + $HOCH_2CH_2Cl$ owing to the similar activation barriers reported (7, 18, 111 kJ mol^{-1}). The kinetic model in Table 1 includes the product branching ratios for the reaction of Cl +

$HOCH_2CH_2Cl$ and the other possible secondary chemistry reactions of Cl and HO_2 radical that are listed in Table 1. The model predicts the amount of HO_2 formed in the reaction mixture and the amount of Cl atoms that are lost as a function of time.

Reactions 1.8 and 1.15 in Table 1 both have large rate constants, but make a negligible contribution to the loss of chlorine atoms because the concentrations of Cl and HO_2 are very small. Reaction 1.20 is a three-body reaction, but because of the relative high concentration of O_2 and the total pressure in the cell, accounts for 3% of the loss of chlorine atoms. Aside from the reactions of Cl with $HOCH_2CH_2Cl$ (reactions 1.11 and 1.12) which account for 52% of Cl atom loss, reaction 1.9 accounts for the largest loss of Cl atoms (44%).

The effect of H and OH radicals on the HO_2 concentration are also included in the model. In this study, 193 nm light was used to initiate photolysis of $HOCH_2CH_2Cl$ in the cell. This wavelength of light is capable of photolyzing both H_2O and O_2 in the cell, leading to formation of H, OH and O radicals. The photon flux and quantum yields for photolysis of H_2O and O_2 predict the formation of 4.5×10^{13} molecules cm^{-3} of H and OH radicals from H_2O photolysis and 3.6×10^{16} molecules cm^{-3} of O atoms from photolysis of molecular oxygen. These values were included as initial concentrations of H, OH and O in the model. HO_2 is formed in the cell from Reactions 1.4, 1.6, 1.12, and 1.18. H and OH radicals have opposing effects on the HO_2 radical concentration. H radical increases the concentration of HO_2 due to the reaction of H and O_2, whereas OH radical remove HO_2 due to the fast reaction between OH and HO_2. H radical is responsible for formation of 34% of HO_2 radical in the cell, whereas OH radical is responsible for 32% of removal of HO_2 radical. Overall, these effects increase formation of HO_2 radical. The model predicts HO_2 concentration to steadily increase after photolysis. But, at 10 ms, the HO_2 concentration is predicted to be 6×10^{12} molecules cm^{-3} and below our detection limit of 1×10^{13} molecules cm^{-3} confirming the experimental observations. HO_2 is not produced in measurable concentration, but can still contribute to the decay of β-HEP and for this reason is included in the model fits.

2.5 Discussion

The current study showed no evidence for significant HO_2 production, but in their investigation of β-HEP self-reaction kinetics with a similar source chemistry, Murrells *et al.*[59] reported measuring significant concentrations of HO_2.. They reported initial concentrations of HO_2 that were twice that of β-HEP and explained that this was due to an unknown source of HO_2 production. One possible explanation for the discrepancy between Murrells *et al.* and this work is that Murrells *et al.* did not include O_3 in their data analysis and it is likely that the signal attributed to HO_2 was instead O_3. No concentrations of precursor gas species were reported by Murrells *et al.* but the published decays of β-HEP have no discernible time delay between the formation of $HOCH_2CH_2$ and β-HEP, suggesting a high concentration of O_2 was used to drive β-HEP formation. A high concentration of O_2 produces a significant amount of O_3 from photolysis at 193 nm. In addition, their wavelength selection of 225 and 260 nm complicates the data analysis. The absorption cross-sections of HO_2, β-HEP, and O_3 are listed in Table 3. At 225 nm the cross sections of HO_2 and O_3 are the same and the cross section of β-HEP is only 28% greater and within 20% of one another, but at 260 nm, the cross section of O_3 is 30 times larger than the cross section of HO_2, and β-HEP's cross section is 11 times larger than the cross section of HO_2. Thus, the use of 225 and 260 nm as probe wavelengths only provides enough information to deconvolve HO_2 and β-HEP from one another. At 225 nm, O_3 absorption overwhelms the signal attributed to HO_2. The absence of treatment of O_3 in Murrells et al.'s work thus explains the discrepancy between the results of Murrells *et al.* and this work.

Table 3 Absorption cross sections of HO_2, β-HEP, and O_3 taken from reference 45. Cross section units: cm^2 $molecule^{-1}$ (1×10^{18})

Wavelength	HO_2	β-HEP	O_3
225 nm	3.16	4.04	3.17
260 nm	0.36	4.03	10.6

Anastasi *et al.*[57] reported a β-HEP self-reaction rate constant of 7.69 (±1.2) $\times 10^{-12}$ cm^3 $molecule^{-1}$ s^{-1} at 300K, 3.4 times larger than the dry rate constant, 2.31×10^{-12} cm^3 $molecule^{-1}$ s^{-1}, others reported.[54-56, 58-59, 75] The difference was attributed to the use of different absorption cross sections for β-HEP[59]. However, Anastasi *et al.*[57] used a water vapor concentration of approximately 1×10^{18} molecules cm^{-3}, resulting in formation of the reactive β-HEP-H_2O complex which they did not account for. The rate constant reported by Anastasi *et al.* agrees with the k_{obs} measured in this work (Equation 43).

The data presented in this work describe the relationship between increasing rates of reaction of peroxy radicals and increasing water vapor. *Ab initio* calculations estimated the equilibrium constant to allow determination of both the percentage of β-HEP complexed with water and the rate constant for β-HEP + β-HEP-H_2O (Reaction 2.5). Enhancement of peroxy radical self-reaction by water depends on the fraction of radical complexed with water and on the nature of the peroxy radical. For example, HO_2 and β-HEP have equilibrium constants of formation with water within an order of magnitude, but at 50% relative humidity and 280 K, the rate constant for β-HEP is 6.1 times larger than the dry rate constant whereas the rate constant for HO_2 is 1.5 times larger than the dry rate constant. The calculated fraction of β-HEP radical complexed with water vapor has a large uncertainty mostly due to the uncertainty in the calculation of K. Future work must measure the K values experimentally to better estimate the enhancement in the β-HEP self-reaction rate.

The contribution of water vapor to the rate of loss of β-HEP and HO_2 is determined by the ratio k_{obs}/k_3 defined here as the enhancement factor. This enhancement factor allows a measure of the contribution of water vapor to the rate of loss of β-HEP and HO_2 at differing temperatures and relative humidities,

Figure 11. For any given water vapor concentration the rate of loss of β-HEP is faster than the loss of HO_2, e.g. at 298 K the rate of loss of β-HEP is twice that of HO_2.

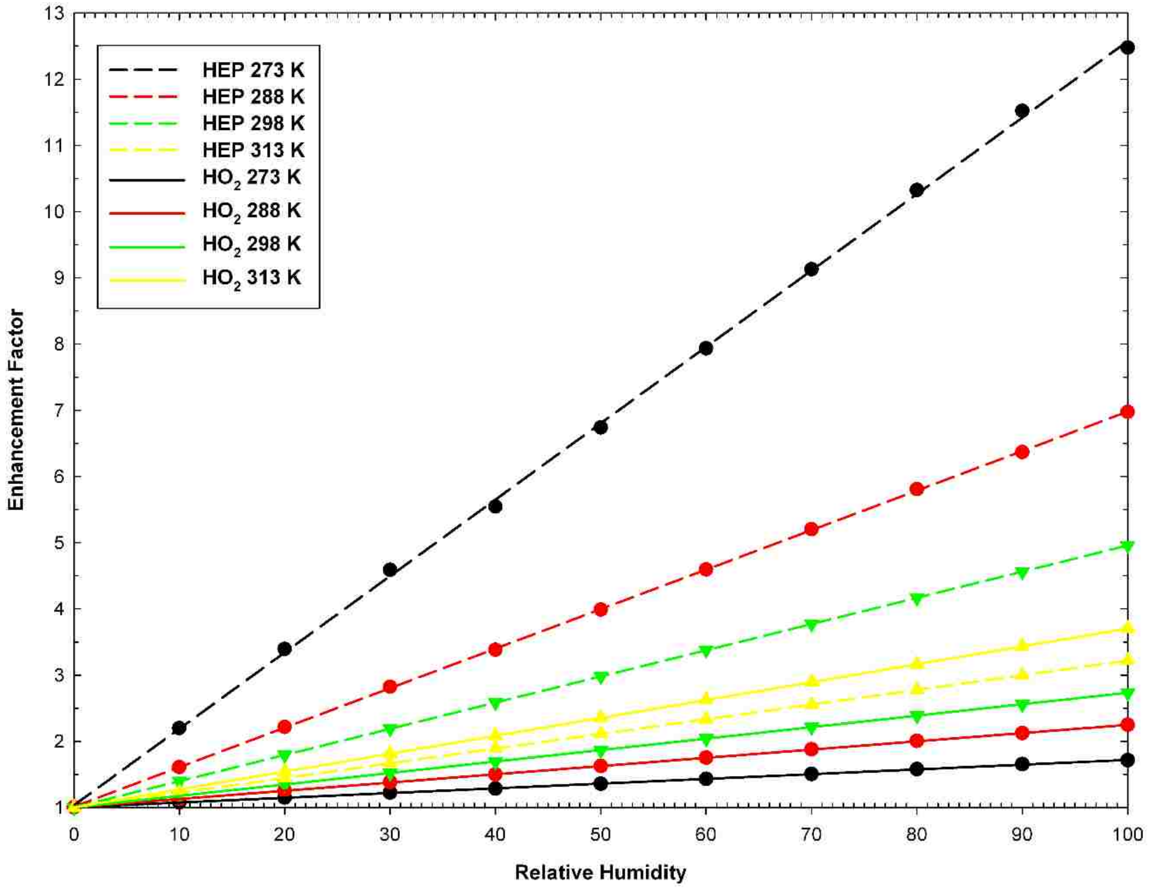

Figure 11 Enhancement of the self-reaction of β-HEP and HO_2 at various relative humidities and temperatures.

2.6 Conclusions

Water vapor catalysis will become increasingly more significant as global warming increases concentration of HO_2 in the atmosphere. As evidenced by the work of Stockwell,[39] inclusion of the effect of water vapor on the self-reaction rate of

HO_2 leads to a 75% decrease in the prediction of tropospheric HO_x and O_3 concentrations. Thus, it is likely that current models overpredict the concentation of β-HEP and other peroxy radicals and consequenlty overestimate the concentration of O_3.

β-hydroxy peroxy radicals are atmospherically important because they are products in the r radicals and should demonstrate a water vapor enhancement of the kinetics. Thus, future studies on the effect of water vapor on the kinetics of peroxy radical reactions should focus on β-hydroxy peroxy radicals and related compounds that form two hydrogen bonds with water and have binding energies greater than 17 kJ mol^{-1}. Most likely inclusion of the effects of water vapor on the kinetics of the β-HEP and HO_2 self-reactions in atmospheric models will lead to predictions of smaller tropospheric O_3 concentations. To correctly predict pollution levels, atmospheric models also need to be adjusted to include the effects of polar molecules such as methanol and ammonia on the rates of radical reactions.

Chapter 3

Ab initio Study of β-HEP Self-Reaction in the Presence and Absence of Water Vapor

3.1 Introduction

RO_2 radicals are formed in the atmosphere by extraction of hydrogen by either Cl, OH or NO_3 radicals from volatile organic carbon (VOC) compounds in the presence of oxygen (Reaction 3.1-3.2). The RO_2 radical thus formed acts as a precursor to ozone formation in the troposphere. (Reaction 3.3a,3.4-3.5)[8]

$$R\text{-}H + OH\bullet \rightarrow R\bullet + H_2O \tag{3.1}$$

$$R\bullet + O_2 \rightarrow RO_2\bullet \tag{3.2}$$

$$RO_2\bullet + NO \rightarrow RO\bullet + NO_2 \tag{3.3a}$$

$$\rightarrow RONO_2 \tag{3.3b}$$

$$NO_2 + h\nu \rightarrow NO + O\bullet \tag{3.4}$$

$$O\bullet + O_2 \rightarrow O_3 \tag{3.5}$$

In high NO_x environments, RO_2 preferentially react with NO to form NO_2 and O_3 (via reaction 3.3a, 3.4 and 3.5). Reaction 3.3b removes the RO_2 radical from the atmosphere by forming stable organic nitrates. In pristine environments with low NO_x concentrations, RO_2 preferentially react with itself or other peroxy radicals in the atmosphere. The self-reaction of the RO_2 radical is known to have three product pathways (reactions 3.6-3.8).[44] All these reactions remove RO_2 radical from the atmosphere, thereby reducing the potential for O_3 production. All three pathways have been observed both theoretically and experimentally for a variety of peroxy radicals including HO_2,[24] alkyl peroxy radicals[44, 46], chloroflorocarbons[47], and other volatile organic carbon compounds.[45, 60, 76]

$$RO_2\bullet + RO_2\bullet \rightarrow 2RO\bullet + O_2 \quad (3.6)$$

$$RO_2\bullet + RO_2\bullet \rightarrow RCHO + ROH + O_2 \quad (3.7)$$

$$RO_2\bullet + RO_2\bullet \rightarrow ROOR + O_2 \quad (3.8)$$

$$RO\bullet + RO\bullet \rightarrow ROOR \quad (3.9)$$

Reactions 3.6 and 3.7 are major products observed in the self-reaction of RO_2, whereas reaction 3.8 is a minor product channel. However, the alkoxy radical (RO) formed in reaction 3.6 further reacts with itself to form peroxides (ROOR) in the atmosphere (reaction 3.9). RO_2 self-reaction (3.6-3.8) proceeds via an RO_4R intermediate to form a variety of products.[8] The intermediate breaks down to form either two RO and an O_2 molecule or re-arranges via single or multiple transition states to form an aldehyde and alcohol as products.

In recent years, it has been shown that the reactivity of RO_2 radical is greatly affected by water vapor in the atmosphere. For example, Butkovskaya et al[40] showed that in the presence of water vapor the branching ratio of reaction 3.3 (a and b) is favored towards production of organic nitrates (3.3b). They used HO_2 radical as the test radical in their study. In a similar study, Kanno et al[29] showed that the HO_2 radical self-reaction rate is enhanced in the presence of water vapor. Both these studies suggest that in presence of water vapor, the HO_2 radical forms a complex with water vapor that enhances the rate of these reactions. As shown in chapter 2, β-hydroxyethyl peroxy radical (β-HEP), a product of ethylene oxidation, complexes strongly with water vapor and the complex enhances the self-reaction rate of β-HEP.

Due to the experimental limitations in chapter 2, it was difficult to identify the products of β-HEP self-reaction in the presence of water vapor. This study aims to identify the possible products and mechanism of β-HEP self-reaction in the presence and absence of water vapor. Barnes et al[45] have experimentally measured the products of β-HEP self-reaction in the absence of water vapor using FTIR spectroscopy. They suggested the major products formed are either the corresponding alkoxy radicals, the corresponding aldehyde and diols (corresponding alcohol), or the corresponding peroxy acids. This observation agrees with the general trend observed in the product distribution for RO_2 self-reactions. This study intends to identify the mechanism by which these products are formed in the absence of water vapor using high level *ab initio* calculations. This study also aims to identify the effects of the β-HEP-water complex on the mechanism of the self-reaction of β-HEP.

3.2 Method

Calculations were performed using the GAUSSIAN 03, Revision D.01system of codes.[77] All geometries for the reactants, products and intermediates were optimized with the B3LYP/aug-cc-pVDZ method and basis set. Harmonic vibrational frequency calculations were performed with the same method and basis set and were used to establish the structures as minima on the potential energy surface and allowed for zero-point energy corrections to be made to the optimized energies. Random constraints sampling method (RCS), which has been described elsewhere,[33, 42] was used to identify the optimum geometry for all the geometries. All calculations were performed on a super-computing Linux cluster consisting of 320 processing nodes equipped with two quad-core Intel Nehalem processors (2.8GHz) and 24GB of memory. All nodes are connected with Infiband, a high-speed, low-latency copper interconnect.

The β-HEP – water complex was also identified using the same method and basis sets. The global minimum and corresponding local minima for the β-HEP – water complexes were calculated in chapter 2 for equilibrium constant calculations. The previously identified global minimum geometry of the β-HEP – water complex was used in this study as the starting reactant in the investigation of the effect of the water vapor on the mechanism of the β-HEP self-reaction. In chapter 2, it was found that a small percentage of β-HEP (7-

15%) complexes with water vapor to form a complex, thus the possibility of two complexes reacting with each other is minimal. Hence, in this study the effect of water vapor on the self-reaction of β-HEP was computed using β-HEP – water complex and β-HEP as reactants. For simplicity, henceforth, the term R represents the $OHCH_2CH_2$ functional group, unless mentioned otherwise. Appendix 3 includes the Cartesian coordinates of all the geometries of this chapter.

3.3 Results

The optimized geometries of the reactants, intermediates and products are shown in Figure 12-16. Relevant parameters such as bond length are included in the figure. The potential energy surface (PES) diagram was created for the self-reaction in the presence and absence of water vapor. The PES were created relative to the energies of the reactants. The PES's are shown in Figures 17 and 18.

Three different geometries for the RO_4R intermediate formed in absence of water were identified, each geometry yielding different products. These intermediates are formed without any activation barrier, thus all three intermediates can co-exist. Since the energies of all three intermediates are within 1.5 kcal/mol of one another, all the product pathways will be competitive with one another. However, computing the preferred product pathway requires application of a molecular dynamics simulation, which is beyond the scope of this work. Each of the product pathways are discussed in detail in following sections. In the presence of water, two RO_4R intermediates were identified that lead to product formation. These intermediates are also discussed in detail in following sections.

All the products formed in the presence or absence of water vapor are exothermic except product I, which is nearly isoenergetic with the reactants. The products predicted in this study are consistent with previously published products of the β-HEP self-reaction, including RO, RCHO, OHR-ROH, RO_2R and O_2.

Figure 12 Reactant geometries.

12a. β-HEP self-reaction in absence of water vapor.

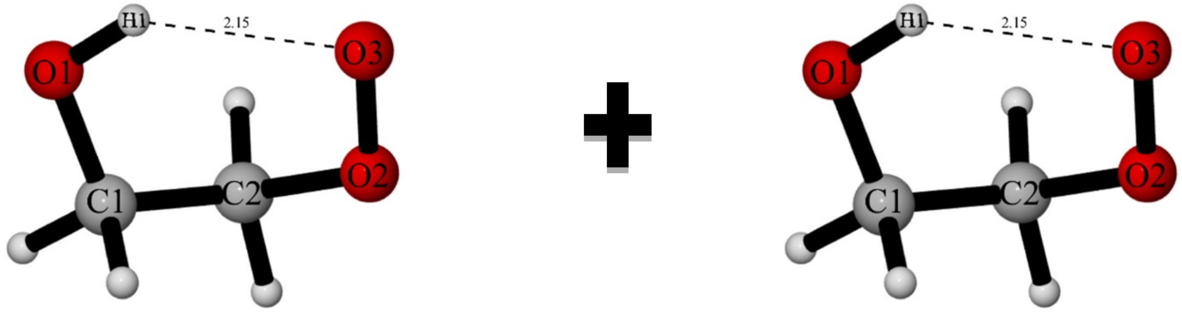

12b. β-HEP self-reaction in presence of water vapor.

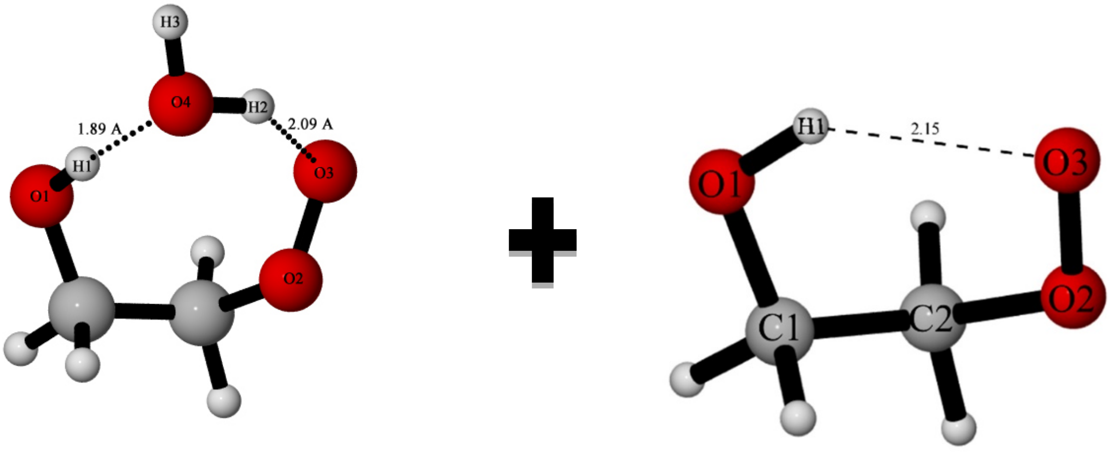

Figure 13 Intermediate geometries of the β-HEP self-reaction in the absence of water vapor.

13a. Intermediate I

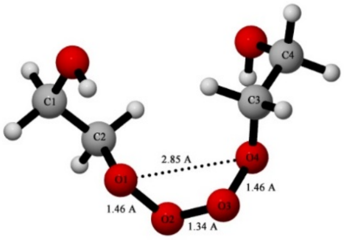

13b. Intermediate II

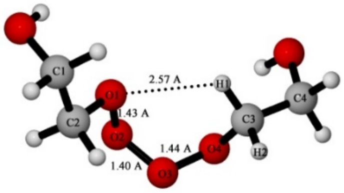

13c. Intermediate III

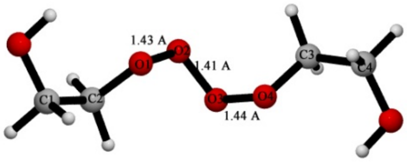

Figure 14 Intermediate geometries of the β-HEP self-reaction in the presence of water vapor.

14a. Intermediate IV

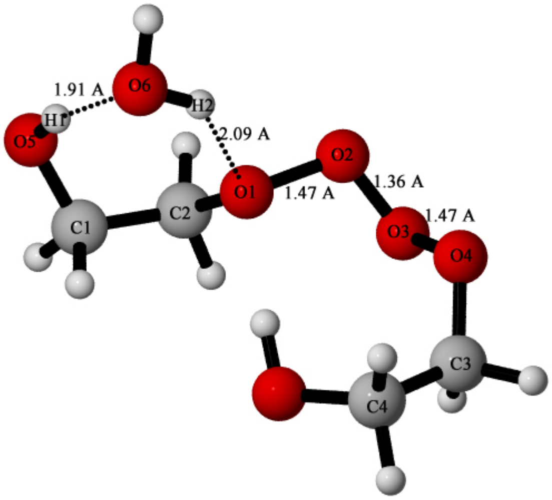

14b. Intermediate V

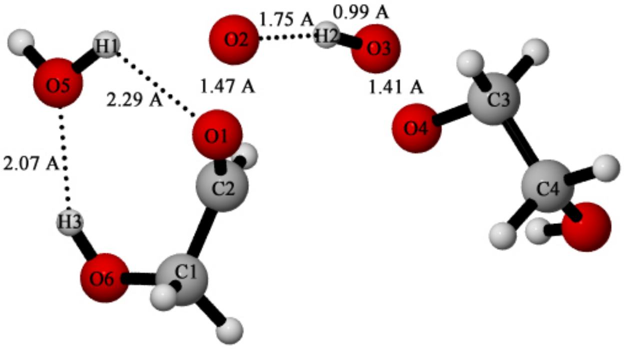

Figure 15 Products of β-HEP self-reaction in the absence of water vapor.

15a. Product I (RO + RO + O_2) arising from Intermediate III

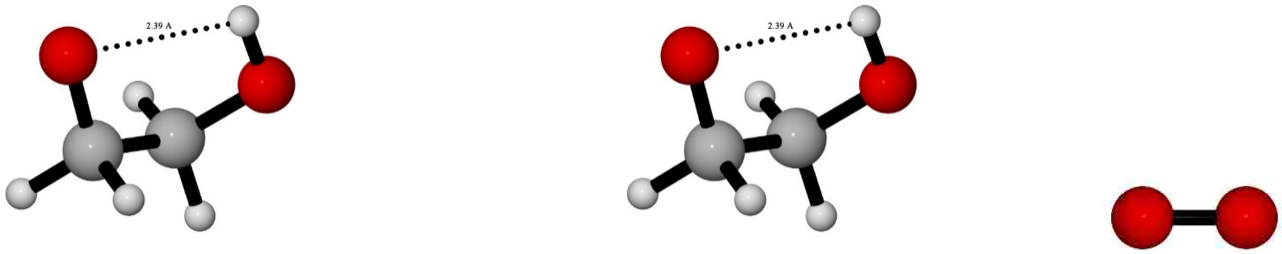

15b. Product II (ROOR + O_2) arising from Intermediate I

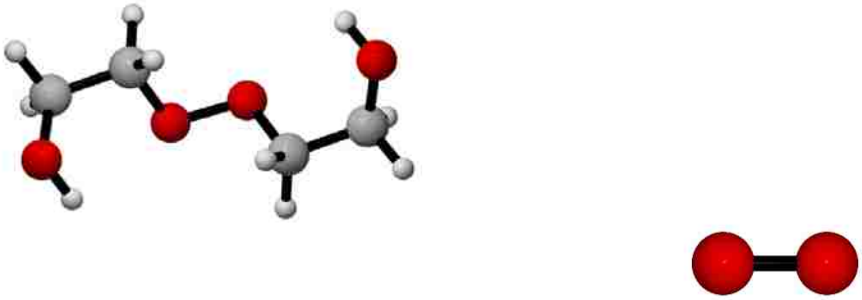

15c. Product III (RCHO + ROH + O_2) arising from Intermediate II

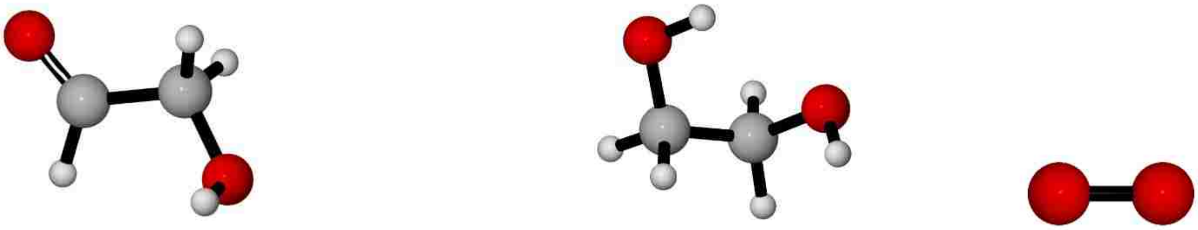

Figure 16 Products of β-HEP self-reaction in the presence of water vapor.

16a. Products IV (RO-H_2O, RO, O_2) arising from Intermediate IV

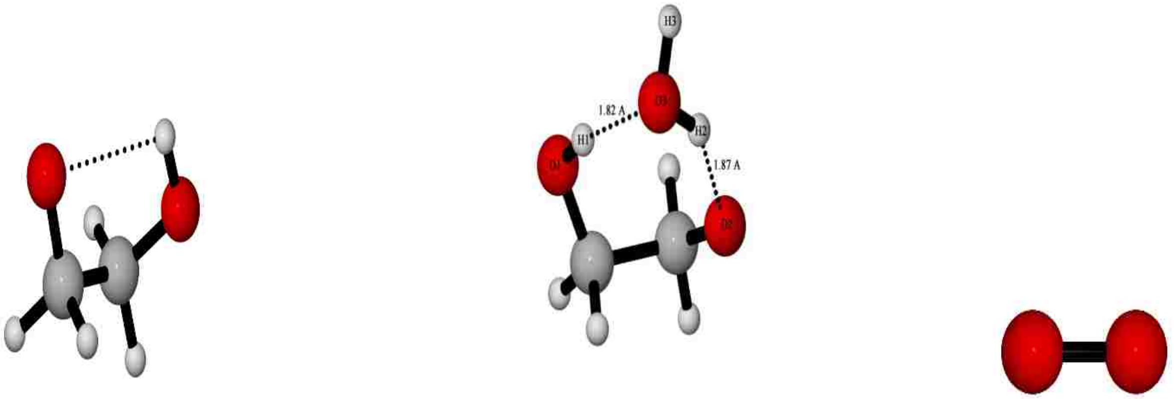

16b. Product V (RCHO, RO, HO_2) arising from Intermediate V

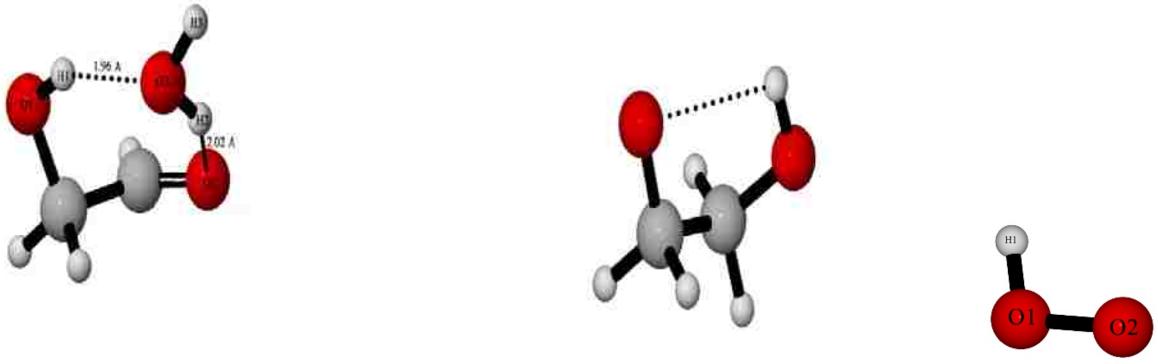

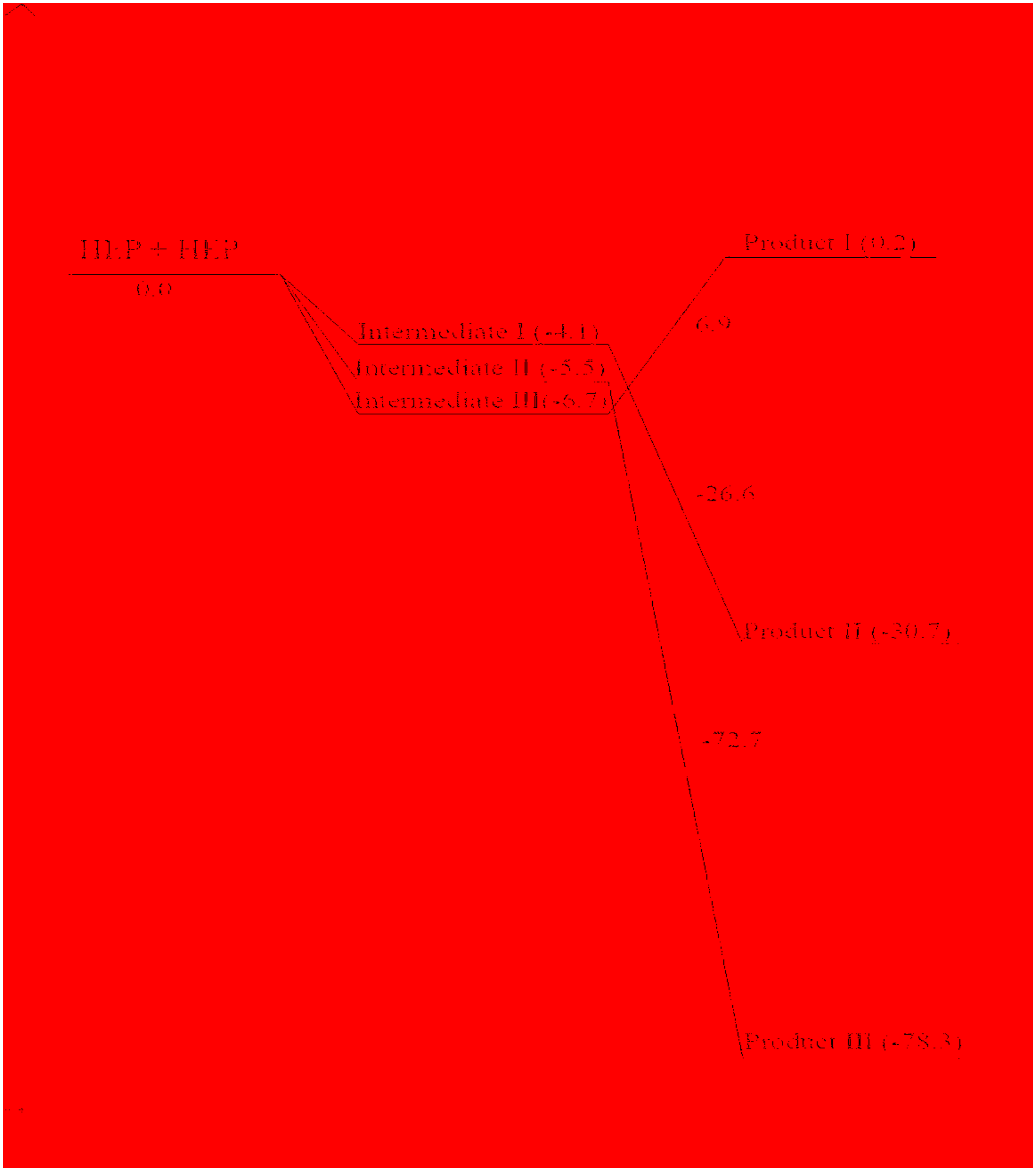

Figure 17 Potential energy surface diagram for β-HEP self-reaction in the absence of water vapor. Energies reported in kcal/mol

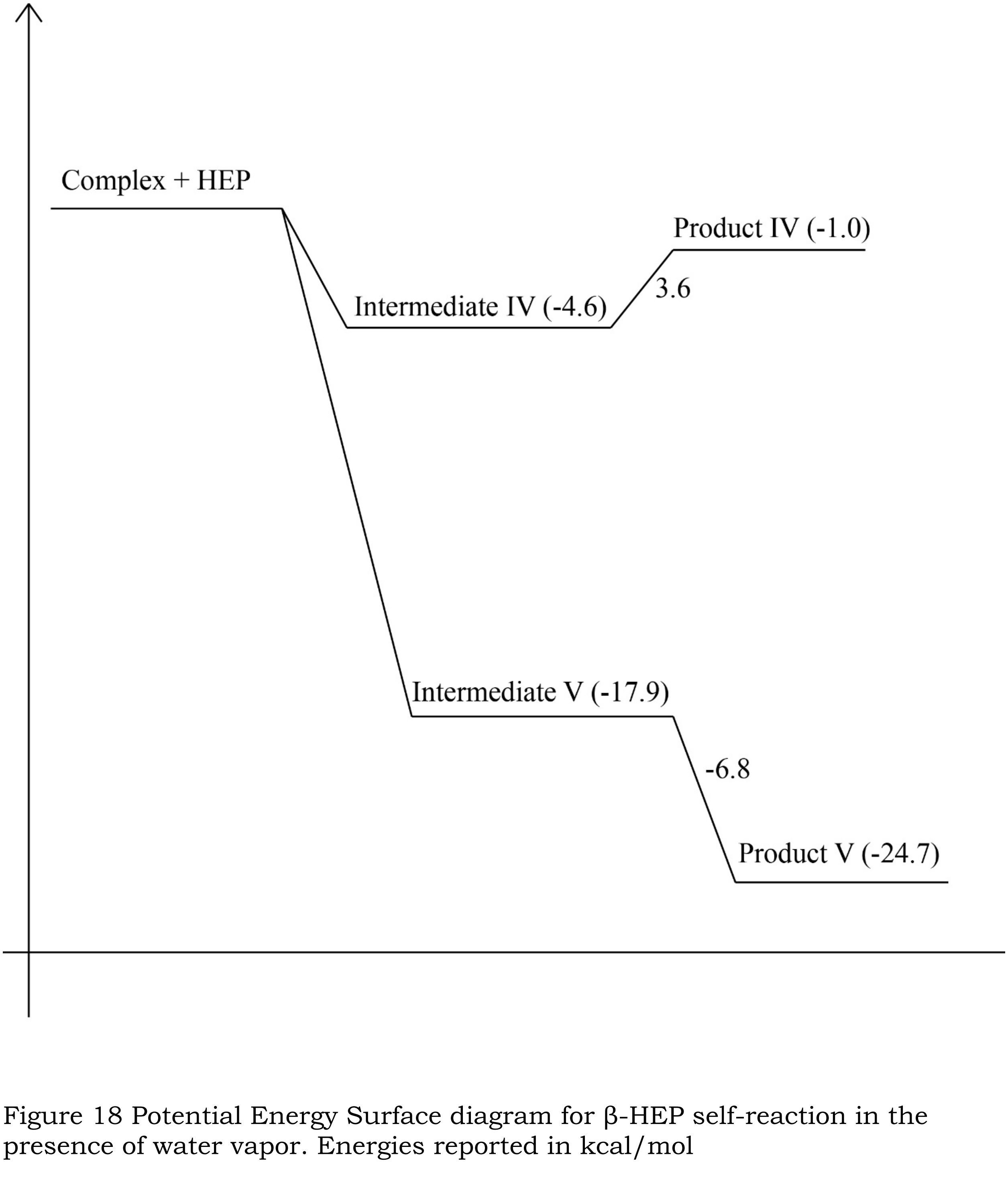

Figure 18 Potential Energy Surface diagram for β-HEP self-reaction in the presence of water vapor. Energies reported in kcal/mol

3.3.1 Product pathway in the absence of water vapor

I. Formation of RO + RO + O_2: These products are formed via intermediate III (Figure 13c). Intermediate III is the lowest energy intermediate of all; 6.7 kcal/mol lower in energy than reactants (Figure 17). This intermediate proceeds to products by rupturing the bond between O1and O2 and between O3 and O4 forming an oxygen molecule and two RO radicals, the geometries of which can be seen in Figure 15. The breaking of these two bonds in the intermediate increases the energy of the products by 6.9 kcal/mol making the products (RO, RO, and O2) (Figure 15a) almost isoenergetic ~0.2kcal/mol with the reactants (Figure 17).

II. Formation of RCHO + ROH + O_2: These products are formed via intermediate II, which is 5.5 kcal/mol exothermic (Figure 17). This intermediate has a cyclic geometry (Figure 13b). The distance between O1 and H1 is reduced to 2.5 Å in the intermediate relative to this distance in the reactant. The distance between O2 and O3 is reduced to 1.4 Å in the intermediate. Thus, when the O1-O2 and O3-O4 bonds rupture to form an oxygen molecule, O1 pulls the hydrogen towards itself forming a diol and an aldehyde (Figure 15c). The products thus formed are much more stable than the intermediate ~78.4kcal/mol (Figure 17).

III. Formation of $RO_2R + O_2$: These products are formed from Intermediate I (Figure 13a), which is 4.0 kcal/mol lower in energy than the reactants, and the highest energy intermediate of all the intermediates (Figure 17). As the reaction proceeds through this intermediate, the O1-O4 distance is reduced to 2.5 Å. When the O1-O2 and O3-O4 bond breaks to form molecular oxygen, the O1-O4 bond shortens to form a new O-O bond, resulting in formation of the RO_2R molecule (Figure 15b), which is 30.7 kcal/mol lower in energy than the reactants (Figure 17). The bond length of the O-O bond in the newly formed peroxide is 1.45 Å.

3.3.2 Product pathways in the presence of water vapor

IV. Formation of $RO\text{-}H_2O + RO + O_2$: These products are formed via Intermediate IV (Figure 14a) which is 4.5 kcal/mol lower in energy than the reactants (β-HEP-water+β-HEP) (Figure 18). Surprisingly, the water bound to the complex remains attached to the R moiety throughout the reaction, resulting in an intermediate that is hydrogen bound to water and an RO that is also hydrogen bound to water (Figure 16a). Intermediate IV has the same parameters as Intermediate I except that it is hydrogen bound to water (Figure 14a).

The products formed from this channel are slightly exothermic relative to the reactant by ~1 kcal/mol (Figure 18).

V. Formation of RCHO-H_2O + HO_2 + RO: These products are formed via Intermediate V (Figure 14b) which is exothermic by 17.89 kcal/mol relative to reactant level (Figure 18). This intermediate is different from the rest of the intermediates found in this PES. Due to multiple hydrogen bonds formed in the intermediate, it is thermodynamically the most stable intermediate. The stability of this intermediate can be attributed in part to the doubly hydrogen bound water to the complex, thus allowing the lengthening of the O-O bond in the complex and granting access to the alpha hydrogen. Access to the alpha hydrogen in the complex allows the second HEP molecule to easily pull off the alpha hydrogen as it is highly acidic. In doing so, the O-O bond in HEP is also lengthened to 2.4 Å nearly breaking it, causing an intermediate where an OH moiety is also hydrogen bound to the O atom in HEP, providing an extra stabilization to the intermediate. This OH-O hydrogen bonded moiety rearranges to form the HO_2 radical in the product, leaving RCHO-H2O and RO as the other products (Figure 16b). Water remains doubly hydrogen bound to the aldehyde product. These products are stable by 24.7 kcal/mol compared to reactants (Figure 18).

3.4 Conclusion

The absence of treatment of the enhancement of water vapor on the β-HEP self-reaction in current atmospheric pollution models leads to prediction of more β-HEP in the troposphere than is measured. As is the case with the self-reaction of HO_2,[39] the over prediction of β-HEP will lead to overestimation in ozone formation rates. Previous experimental work[45] observed both product pathway I (2 alkoxy radicals) and product pathway III (an aldehyde and a diol), but did not detect the RO_2R pathway (product II). Although the computational results from this study, indicate a thermodynamically favorable pathway for RO_2R formation. Without direct measurements of the three product pathways I can only speculate as to the product branching ratio of β-HEP-H_2O + β-HEP. With the addition of water, the potential energy surface is different from the dry potential energy surface but has similarities. Product IV is analogous to product I with slightly different energies due to the presence of water. Product V is dramatically lower in energy (23.7 kcal/mol) but here only one alkoxy radical is produced, and instead of a second alkoxy radical and O_2, an aldehyde and an HO_2 radical are produced. With the addition of water vapor, a new thermodynamic pathway exists (Product V). Product pathways IV and I create two additional alkoxy radicals, product pathway II creates a stable organic molecule, and pathway V creates a stable organic, an alkoxy radical and HO_2. A change in the product branching from product I to either product IV or V does not lead to large change in ozone formation rates because the products are alkoxy radicals that photoxidize to produce HO_2 or HO_2 directly and will eventually lead to ozone formation. On the other hand, a change in the product branching from product III to products IV or V leads indirectly to an increase in ozone formation. Experimental evidence for a change in the product branching ratio would substantiate the results of the computational study and give concrete information about the effect on ozone production.

3.5 Future Work

The study of the PES of β-HEP self-reaction in the presence of water vapor is incomplete. The study is missing the transition state between reactant and Intermediate V. Intermediate V undergoes a proton transfer from the carbon (C2) to β-HEP oxygen (O3) to form HO_2. The transfer has to undergo a transition state from the reactant to intermediate. However, using various ab initio methods including transition state calculation, intrinsic reaction coordinate study and fixed atom transition state calculation, the transition state was not identified. Due to the number of atoms involved, the method and large basis set used, and other computational limitations, this study failed to identify the transition state. I am working in collaboration with Dr. Joe Francisco’s lab at University of Nebraska to identify this transition state.

Chapter 4

Role of Radical-Water Complexes in Particle Formation

4.1 Introduction

Aerosols with an aerodynamic radius of < 2.5μm are also known as particular matter ($PM_{2.5}$), are very important in the atmosphere, as they can influence climate, visibility, trace gas levels, and human health.[6-7, 48] Gaseous molecule conversion to aerosol particles is the most common mechanism for particle formation in the atmosphere.[78-80] These newly formed particles can grow in size and act as cloud condensation nuclei (CCN), contributing to climate cooling.[10, 81] The majority of global cooling of the atmosphere is due to clouds formed from aerosol particles.[3] Although aerosols play an integral role in climate, formation of new particles in the atmosphere is not well understood.[13] This limits the ability to quantify the effects of aerosol particles on visibility, human health and climate change as well as to develop effective control strategies.[3, 13, 48]

Field measurements have shown that sulfuric acid is a major contributor to new particle formation in the atmosphere.[48] Sulfuric acid is known to form new particles in the presence of both organic compounds[82] and bases such as ammonia and amines.[48, 83] However, the atmospheric concentrations of sulfuric acid, ammonia and VOC are not sufficient to account for observed aerosol concentration in the atmosphere.

The most accepted theory for formation of aerosols is classical nucleation theory,[10] in which formation of aerosols is described by a two-step process. The first step is nucleation step where molecules cluster together to form a critical cluster. The second step is subsequent growth of the critical cluster through coagulation or condensation (Figure 1). Using these models, current predictions of atmospheric aerosol content seriously underestimate the actual measured concentration of aerosols in the atmosphere.[10] Many studies involving non-sulfuric acid compounds have been performed in an effort to bridge the gap between modeled and observed aerosol concentrations. Organic compounds such as formic acid, acetic acid, isoprene, and α-pinene have been identified as precursors for aerosol formation. [84-85]

This study aims to identify new species that can act as a critical cluster to form aerosol particles in the atmosphere. This work examines the ability of radical-water complexes to act as the critical cluster. Although radicals are found in much smaller concentrations in the atmosphere than CO_2, water vapor, oxygen or nitrogen gas, they are very reactive and as such are important components of air. Some of these radicals include hydroperoxy radical (HO_2), hydroxyl radical (OH), chlorine radical (Cl), and alkyl radicals (R). Water molecules significantly influence the properties and reactions of these radicals. Radical-water complexes play an important role in controlling the abundance and chemical behavior of these species in the atmosphere.[29, 40, 72, 86] Both experimental and theoretical studies have been performed to prove the existence of a HO_2-water complex.[72, 86 41, 87] It is thermodynamically favorable for more water molecules to hydrogen bond with the existing HO_2-water complex. The acidic proton present in the complex allows for more water molecules to hydrogen bond with the complex, allowing the complex to act as the critical cluster to form the aerosol particle. Thus, an initial binary nucleation of HO_2 with a water molecule is expected to act as the nucleating seed for forming the critical cluster required for particle growth and aerosol formation. This hypothesis is tested experimentally in this work using a fast flow reactor coupled with a scanning mobility particle sizer (SMPS). The results indicate that at atmospherically relevant temperature and pressures, HO_2–water complex does not act as a nucleating agent to form aerosol particles.

4.2 Instrument set-up

Figure 19 shows the principle components and layout of the experimental setup. The photolysis cell is 256 cm long (2.5 cm i.d.) including the end boxes. The end boxes support the Pyrex glass cell and are purged with 99.9% pure O_2 gas to dilute the chlorine gas entering the scanning mobility particle sizer (SMPS). The boxes also hold windows for UV and IR light to pass through the cell. The gases are pre-mixed in a manifold before being introduced into the reaction cell and are heated using heating tape coiled around the manifold. CaF_2 windows (ThorLabs) are used at both ends of the cell to transmit both UV and IR light over the range of interest. Kinematically mounted mirrors in the optical path of the system make it possible to switch between UV and IR detection methods without changing the position and alignment of the flow cell, light sources, and detectors. Gas mixtures of $CH_3OH/O_2/Cl_2/H_2O$ flow continuously through calibrated flow controllers [Teledyne – Hasting Technologies (HFC series)] and Magnehelic controllers [Dwyer Instruments Inc.] at a flow rate of 10 liters per minute (LPM). Anhydrous CH_3OH was purchased from Macron fine chemicals and used without further purification. 5% Cl_2 in N_2, O_2 (99.9%) and N_2 (99.9%) cylinders were purchased from Airgas (Salt Lake City, Utah). The optics and the track to move the photolysis source were purchased from ThorLabs. A diluting nozzle adapted from Karlsson et al.[88] was built to dilute the Cl_2 gas entering the SMPS and to quench further growth of aerosol particles (discussed in detail in the following section). The sampling gas was further diluted in the diluting nozzle using 99.9% pure N_2 gas at 4 LPM (2X dilution). All the gases pass through a particle filter placed at the mouth of the cylinder and the photolysis cell. The study was conducted at room temperatures and atmospheric pressures (~650 torr). An ammonia scrubber purchased from Perma Pure Inc. was placed at the mouth of the photolysis cell where the gases enter to remove any ammonia from the gases.

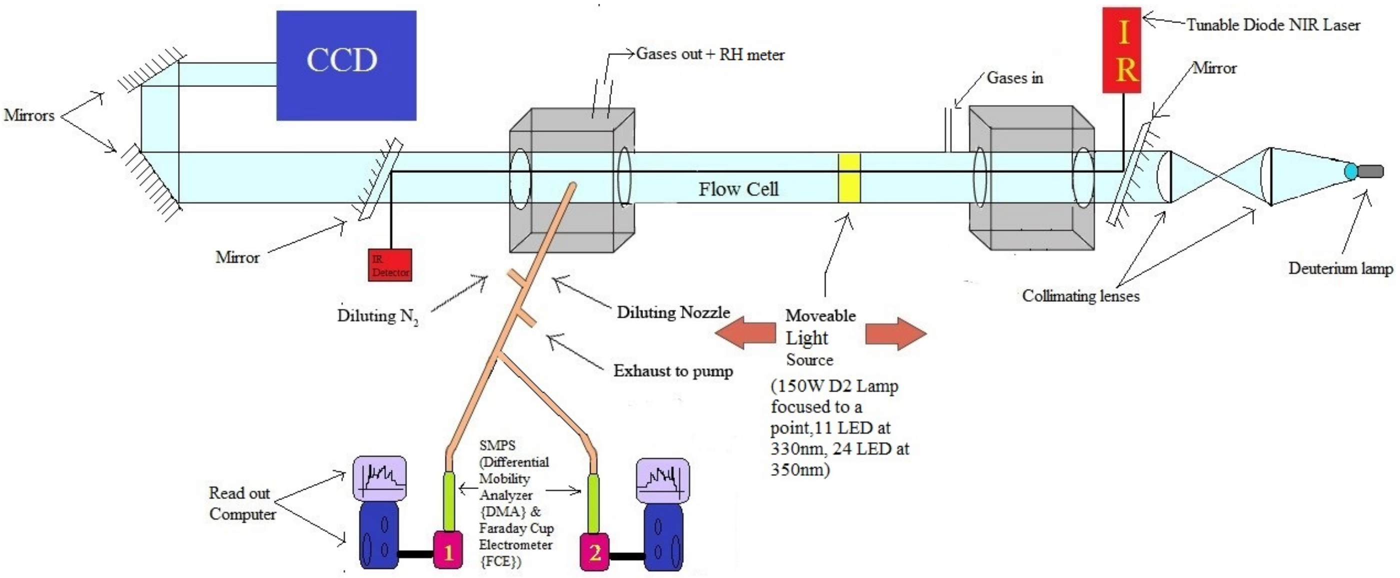

Figure 19 Experimental set-up to generate and measure radical and aerosol particles

4.2.1 Radical generation

HO_2 radical was formed in the reaction cell by introducing a gas mixture containing 80 Torr of CH_3OH, 3.5 Torr of Cl_2, 400 Torr O_2 and balance N_2 gas (~165 torr). CH_3OH was introduced in the gas mixture via two 500mL bubblers placed in series with N_2 flowing at 2LPM as the carrier gas. The bubblers temperature was maintained at 45 ºC by immersing it in a constant temperature water bath. HO_2 radical was generated in the cell via the following reactions.

$$Cl_2 + h\upsilon \longrightarrow Cl\bullet + Cl\bullet \tag{4.1}$$

$$CH_3OH + Cl\bullet \longrightarrow CH_2OH\bullet + HCl \tag{4.2}$$

$$CH_2OH\bullet + O_2 \longrightarrow HO_2\bullet + CH_2O \tag{4.3}$$

Initially a 150 W deuterium lamp coupled with collimating lens was used to photolyze the Cl_2 gas in the cell, which is positioned on a track that runs parallel to the reaction cell. Sliding the light assembly (lamp + collimating lenses) along the track, provides reaction times in the flow cell ranging from 0.6 to 6.5 seconds. The collimating lenses collimate the UV light in the flow cell with a diameter of roughly 1cm. This assembly produced ~8.3×10^{11} photons cm^{-2} s^{-1}. Assuming a photolysis of 0.1-1% of the radical precursor, only 8-10 x 10^8 molecules/cm^3 of HO_2 was produced, which was below the detection limits of the CCD (3×10^{13} molecule/cm^3). Thus, additional light sources were introduced to increase the number of photons in the cell. Eleven LEDs emitting 330 nm light with 3 mW of power each were added and 4 banks of 13 LEDs at 375nm (2.5mW each) were also added. Together they generated ~ 2×10^{17} photons/s, which produced at least 1×10^{14} molecules/cm^3 of HO_2 radical (assuming 0.1% photolysis of Cl_2 gas). By adjusting the concentration of methanol and chlorine gas in the flow cell the amount of HO_2 radical generated in the flow cell could be varied.

4.2.2 Scanning Mobility Particle Sizer

HO_2 radicals react with water vapor in the flow cell to form the HO_2-H_2O complex. This complex is assumed to act as the nucleating site for aerosol particle formation. The complex further reacts with more water molecules in the flow cell to form aerosol particles. The proposed mechanism for formation of aerosol particles is shown by the following reactions:

$$HO_2\bullet + H_2O \longrightarrow HO_2\text{-}H_2O \qquad (4.4)$$

$$HO_2\text{-}H_2O + nH_2O \longrightarrow \text{Aerosol particle} \qquad (4.5)$$

Where n can be anything greater than 3 in reaction (4.5). The size of the aerosol particle formed will depend on the reaction time available for the complex to react with water molecules. The reaction time is a function of the distance of light assembly from the sample inlet. At the exit of the flow cell the aerosol particles are sampled at a rate of 1 LPM using a diluting nozzle. The sampled aerosol particles are diluted with N_2 gas and are then sent to the detector where they are detected for their size distribution and absolute number densities. An SMPS is composed of two main parts namely: (1) a differential mobility analyzer (DMA) and (2) a faraday cup electrometer (FCE). A GRIMM technologies SMPS + E system was used in this work. Aerosol particles formed in the flow cell enter the sample inlet tube of the DMA. The DMA consists of a Kr-85 bipolar charger that is used to neutralize the charges on the aerosol particles. The DMA separates the particles based on electrical mobility. The separated particles then enter the FCE. It consists of an electrometer and a filter inside a Faraday cage. The particles are collected by a filter in the FCE, which in turn, generates an electric current that is measured by the electrometer. The current generated is directly proportional to the particle concentration. The particle distribution and absolute concentrations are recorded and displayed on a PC. The size range that the DMA can measure is a function of the ratio of aerosol sample flow and the sheath flow in the DMA. The smallest particle that the instrument can measure is 0.8nm, and the range is 0.8-39nm. However, the noise below 2nm is very high and instrument accuracy is also less than 10% below 2nm. To measure the range of particles of interest in this project (0.8-1100nm) requires the use of two SMPS detectors. The second SMPS used in this study measures the smallest particle size at 10nm and the range is 10-1100nm. Due to very short reaction times, particle size growth above 600nm is not expected. Thus, particle size range from 2-600nm was studied. The gas flow leaving the reaction cell was collected with a diluting nozzle that was split into two equal flows and each flow was introduced into a SMPS as shown in the Figure 19. The wall loss in the photolysis cell and diluting nozzle was measured to be less than 10% by introducing NH_3Cl particles (generated using a nebulizer) into the cell. Appendix 4 explains how to use the SMPS instrument.

4.2.3 Diluting Nozzle

After the prescribed reaction distance, the gas mixture was sampled through a diluting nozzle in order to quench further aerosol chemistry. Figure 20 shows the schematic representation of the diluting nozzle. The diluter consists of two concentric cylinders with a blunt nose cone. From this cone, a small fraction of the aerosol (2.0 L/min) is pulled through a small orifice into the central tube, which is constructed of sintered stainless steel. Pressurized N_2, introduced into the outer annulus, enters through the sintered walls to dilute the sample. The total flow relative to the N_2 diluent flow, both controlled using flow controllers, determines the dilution ratio, which can be varied from

0:1 to >50:1 (typically 4:1). Dilution is necessary because of the corrosive nature of Cl_2 gas. Cl_2 gas is known to damage the DMA in the SMPS. Diluting the sample flow reduces the Cl_2 concentration in the sample making it less harmful to the DMA.

Figure 20 Schematic of diluting nozzle.

4.3 Results

4.3.1 Radical Measurement

UV absorption spectroscopy was used to measure the HO_2 radical concentration in the cell. An Andor manufactured charged coupled device (CCD) with a spectrograph was used as the detector, which measured from 225nm-350nm. A 30 W D_2 lamp collimated with multiple concave lenses was used as the probe beam which entered the photolysis cell coaxially as shown in Figure 19. The background light intensity (I_0) of the probe beam was measured before the photolysis light was turned on. The light intensity (I) was measured after turning the photolysis lamps on. The logarithmic ratio of I/I_0 gave the absorption of HO_2 in the cell. HO_2 absorbs UV radiation from 200-260nm with a peak absorption at 205nm (Figure 21). In this experiment, HO_2 absorption was measured from 235nm – 250nm. Absorption data at multiple wavelengths permits a least-squares fit for accurate concentration measurement. A typical absorption fit for HO_2 is given in Figure 22. Depending on the carrier gas flow rate and water bath temperature, $7 \times 10^{13} - 3 \times 10^{14}$ molecule/cm^3 of HO_2 radical was measured in the experiment.

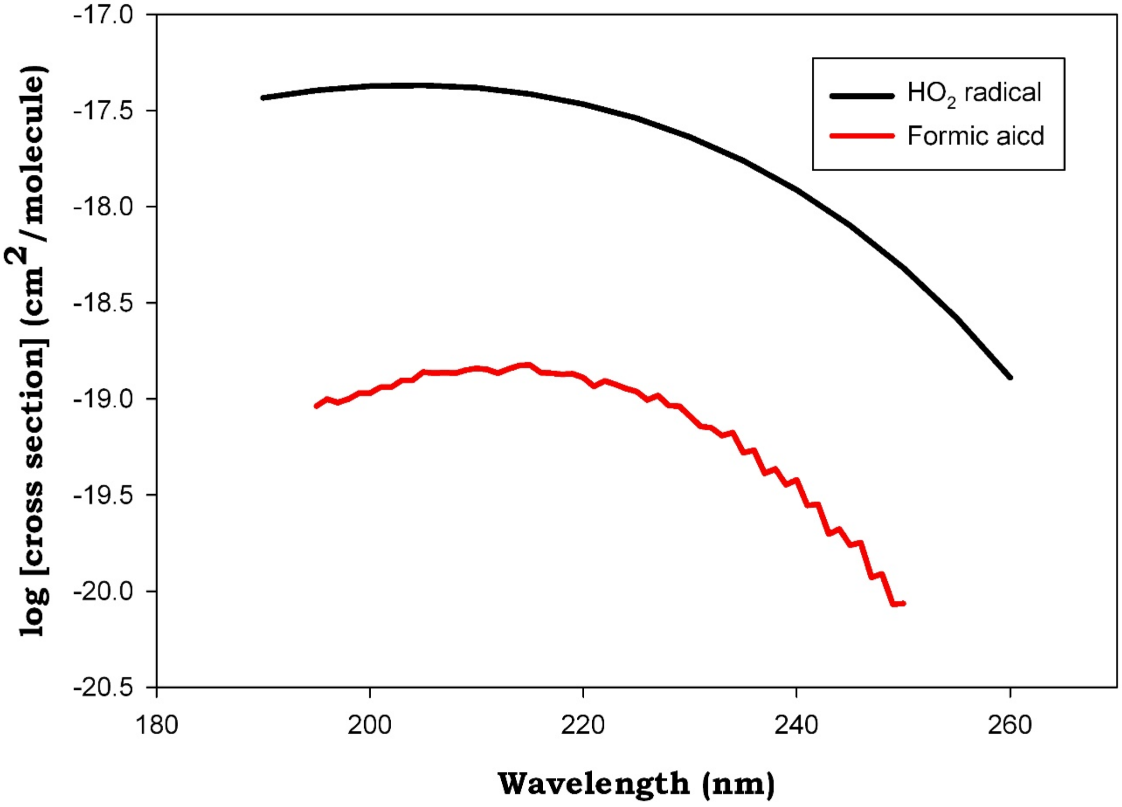

Figure 21 Cross section of HO_2 radical and formic acid.

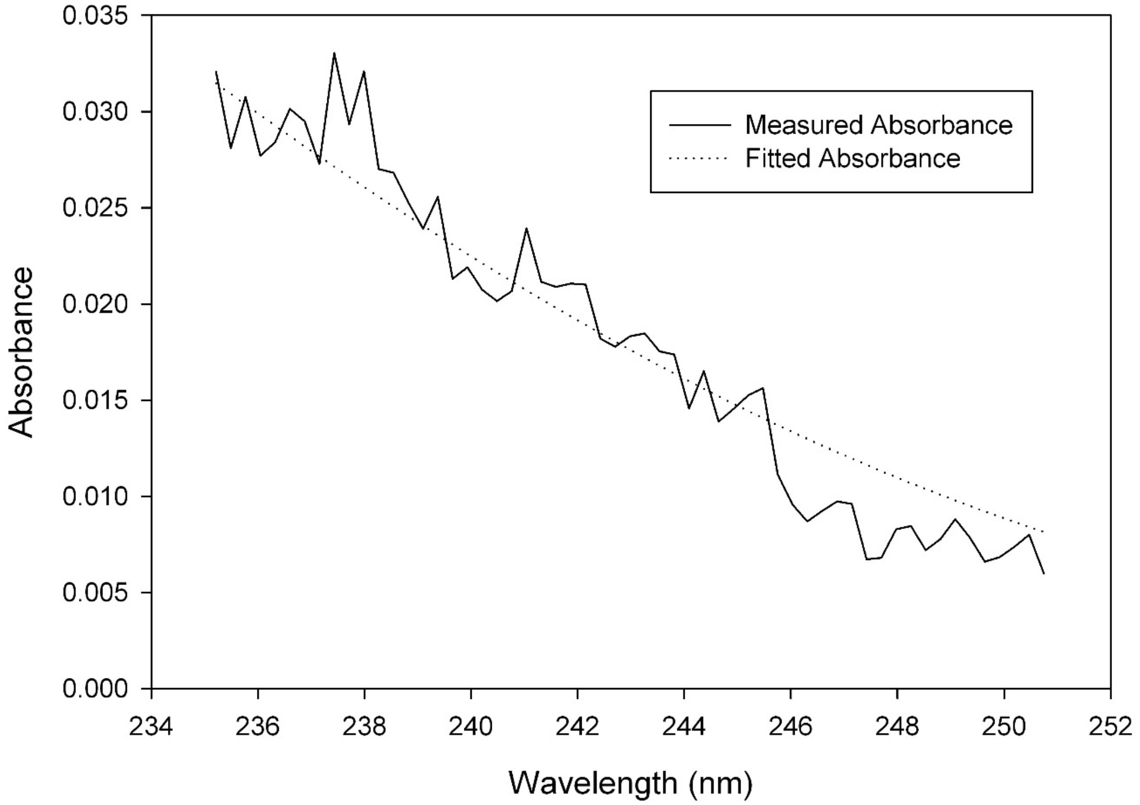

Figure 22 Typical fit to measured HO_2 absorbance.

4.3.2 Water generation and Measurement

Water vapor was introduced into the reaction cell by passing N_2 carrier gas through a bubbler immersed in a constant temperature bath. The amount of water vapor in the reaction cell was controlled by both the temperature of the water and the percentage of total flow of the carrier gas passing through the bubbler. The water vapor concentration was varied between 1.0×10^{17} and 2.3×10^{17} molecules cm^{-3} (RH = 40%-55%). The water vapor concentration was held constant during each experiment, varying no more than ±8% over the duration of an experiment.

Wavelength modulated IR diode laser spectroscopy was used to quantify the water vapor concetnration in the cell. Figure 19 shows the IR system components. IR light was scanned over a narrow frequency band (100 Hz) centered at the 6600 cm^{-1} line such that the entire peak of the selected rovibrational transition of water vapor was observed. The IR beam was produced by a New Focus TLB-6326 tunable diode laser with a line width of <300 kHz and directed towards an IR 1-GHz low-noise photoreceiver (New Focus 1611). The signal from the detector was synchronized with the 100 Hz modulation frequency and visualized and recorded by a digital oscilloscope (TeKtronix model TDS 3024B). Data were processed and converted from absorption measurements to concentrations with a LabVIEW routine is explained in chapter 2. Absorption line strengths were obtained from the HITRAN[68] database and converted to cross sections. An Omega relative humidity meter was also used to independently verify the spectroscopically measured water vapor concentrations.

4.3.3 Aerosol Measurement

Both SMPS's were synchronized to measure the aerosol concentration and size distribution to <1 second difference during data collection. A total of 5 runs (67 seconds each) were averaged for each setting. A background aerosol count was measured first, which consisted of all the gases flowing ($CH_3OH+O_2+Cl_2+N_2+H_2O$) and photolysis lamp turned off. A background of 2 x 10^5 particles/cm^3 was typically observed. Typical particle size distribution and concentration plots are shown in Figure 23. No significant increase in particle formation was observed after generating HO_2 radical in the system by turning the photolysis lamp on. No new particle formation was seen after varying the HO_2 concentration between 7 x 10^{13} and 3 x 10^{14} molecule/cm^3 and water vapor relative humidity between 40 and 55%. Changing the position of the photolysis lamp allowing for reaction times ranging between 2s and 6s also had no effect on particle formation.

A recent study from Chen et al.[80] suggested that water vapor can condense and form aerosol particles on any surface it encounters including glass walls. This indicates that water vapor should not be included when measuring the background aerosol concentration. A new background aerosol concentration was measured, which consisted of all the gases except water vapor and the photolysis lamp turned on (HO_2+CH_3OH+Cl_2+O_2+N_2+secondary radicals). The background concentration was still measured at 3-5 x 10^5 particles/cm^3. Addition of water vapor to the background did not change the particle concentration. Once again, no new particle formation was observed after varying the HO_2 concentration, H_2O concentration and the position of the photolysis lamp. This set of experiments indicates that the HO_2 – water complex does not have the ability to act as a nucleating site under the conditions probed. Possible reasons for this behavior of HO_2 radical is discussed in the next section.

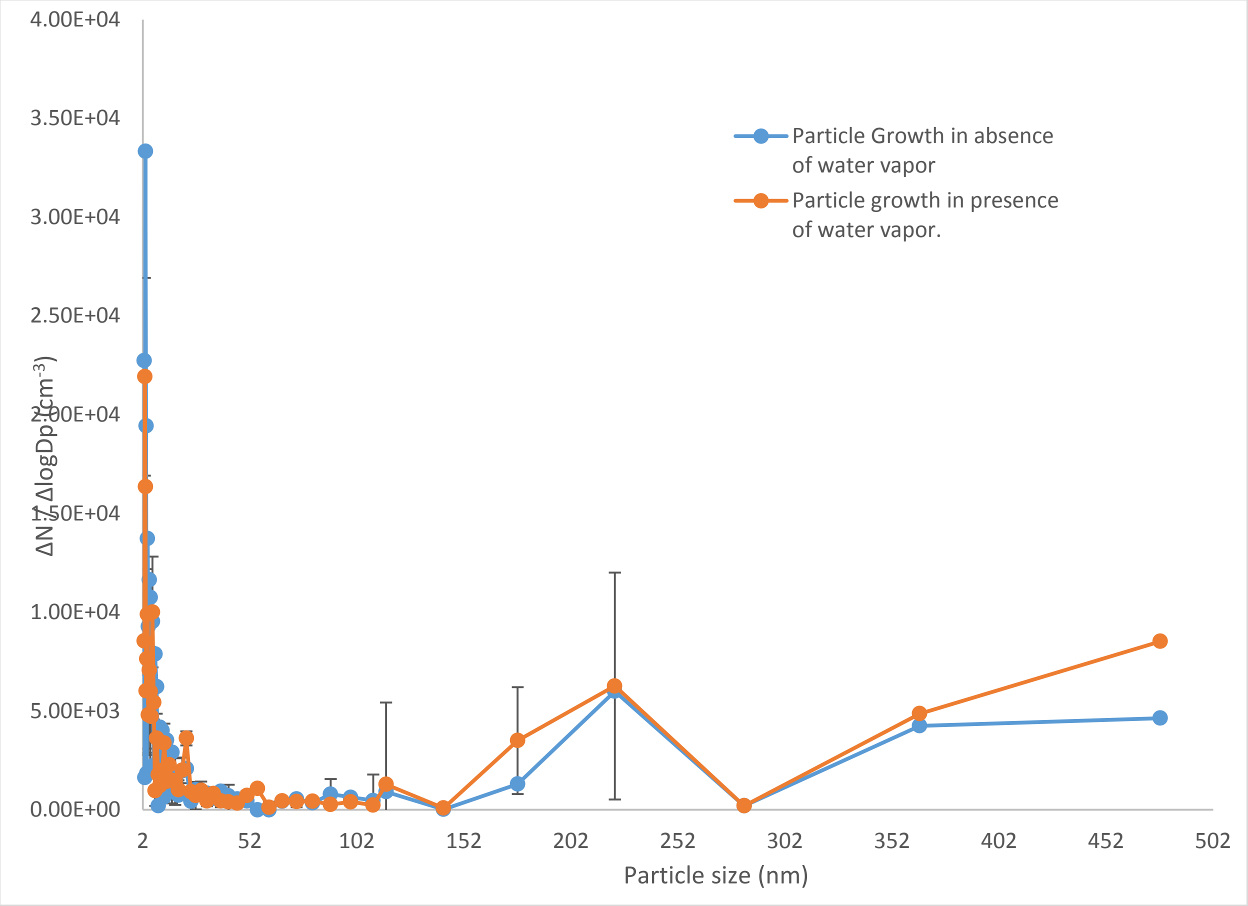

Figure 23 HO_2 initiated particle formation in the presence and absence of water vapor at RH 45% and reaction time of 6.5s.

4.4 Discussion

New particle formation in the atmosphere is best explained by classical nucleation theory. It suggests that a critical cluster must be formed to generate an aerosol particle in the atmosphere. However, a nucleation barrier must be overcome in order to form the critical cluster needed for particle growth. This barrier is reduced if the nucleating species are ions or highly polar molecules. Thus, ion-induced nucleation is favored over neutral nucleation. H_2SO_4 – water is the most studied system for aerosol formation in the atmosphere. Recent studies on the sulfuric acid-water system challenge the current understanding of aerosol formation by sulfuric acid and in turn for other systems.[80, 89-92]

Recent studies suggest that binary nucleation of sulfuric acid - water is most favorable at stratospheric temperatures (216K – 273K) rather than tropospheric temperatures (273K – 313K),[92] suggesting that the equilibrium constant for complex formation increases with decreasing temperature allowing for more sulfuric acid to complex at lower temperatures. The calculated binding energy of sulfuric acid water complex is approximately 10 kcal/mol and linearly becomes more exothermic with addition of more water molecules. Hussar et al[89] in another computational study suggested that, at 298 K, bisulfate ions are the primary species involved in particle formation. They also showed that bisulfate ion – water nucleation is favored over sulfate ion – water nucleation as bisulfate ion is more polar than sulfate ion, allowing for easier hydrogen bonding of multiple water molecules to form a critical cluster. Another study by Temelso et al[91] they found that sulfuric acid dimers nucleate better with water vapor than sulfuric acid alone. They explained when the dimer-water complex is hydrogen bonding to a second water molecule it begins the deprotonation of one of the sulfuric acid molecules in the complex resulting in formation of a di-ionic species similar to bisulfate ion causing the nucleation barrier to drop dramatically. Temelso et al[92] in another study also stated that "The progression of the nucleation mechanism (for sulfuric acid) from purely binary at 248K to a mixture of binary and ternary (with ammonia and amines) at 278K to purely ternary at 298K is expected". This computational study was confirmed by CLOUD studies performed by Kirkby et al.[48]. Chen et al.[80] studied methane sulfonic acid (MSA) nucleation at room temperature in an experimental set-up similar to the current system. They observed that binary nucleation of MSA – water does not produce any aerosol particles. They also studied the ternary nucleation of MSA by dimethyl amine (DMA) and trimethyl amine (TMA) in the presence and absence of water vapor, and observed significant particle formation in the presence of both amines (with TMA favored over DMA). They concluded that both water vapor and amines (base) are necessary to form aerosol particles at room temperature. This observation is also true for sulfuric acid ternary nucleation with either ammonia or amines with amines favored over ammonia.[90]

These recent publications suggest that binary nucleation at room temperatures is unlikely to form aerosol particles. However, at colder temperatures binary nucleation is a major pathway to form aerosol particles. For particles to be formed at ambient pressures and temperatures, the acid-water complex must be stabilized further by a base (NH_3 or an amine), which lowers the nucleation barrier to form the critical cluster. Ternary nucleation involving a base like ammonia or amines is the primary reason for particle formation at room temperature.

This study primarily focused on the binary nucleation of HO_2 radical with water vapor. When this experiment was designed, the afore-mentioned studies had not yet been published, and thus that binary nucleation of HO_2 radical would not occur at room temperature was not expected. A water jacket around the reaction cell to control the temperature of the cell was not designed in this initial experiment. A jacketed cell was not used because the photolysis light was placed perpendicular to the cell, and the light would have had to pass through the jacket causing it to diverge, making it difficult to focus the 150W D_2 Lamp or the LED lights into the cell to photolyze the HO_2 radical precursors. Therefore, in the absence of a jacketed reaction cell to reduce the temperature of the reaction mixture, the current study cannot confirm that HO_2 radical binary nucleation can form aerosol particles at lower temperature.

Ternary nucleation of HO_2 radical is also not possible to study with the current setup for the following reason. HO_2 radical is generated in the system in situ by reacting chlorines atom with methanol in the presence of molecular oxygen. Any addition of a base like ammonia or amines would instantly react with the chlorine gas (which is 3 orders of magnitude higher concentration than HO_2) in the cell and form ammonium chloride particles. In an attempt to address this issue, HO_2 radical was made by photolysis of formaldehyde. Formaldehyde photolyzes between 310nm-360nm to form HO_2 radical via the following reactions

$$HCHO + h\upsilon \longrightarrow H\bullet + HCO\bullet \tag{4.6}$$

$$H\bullet + O_2 \longrightarrow HO_2\bullet \tag{4.7}$$

$$HCO\bullet + O_2 \longrightarrow HO_2\bullet + CO \tag{4.8}$$

Both formalin (saturated solution of formaldehyde (37%) in water) and paraformaldehyde (solid polymeric form of formaldehyde) were tested to generate HO_2 radical. Formalin was introduced into the reaction cell similar to the way methanol was introduced into the cell. HO_2 radical was observed in the reaction cell with formalin but, when paraformaldehyde was used to generate HO_2 radical, no radical was measured. On further investigation, it was found that formaldehyde easily oxidizes to form formic acid in the presence of water. Formic acid has almost an identical cross section as HO_2 radical, the only difference being HO_2 radical absorbs UV radiation more strongly (by two order of magnitude) than formic acid (figure 21). Thus what was assumed to be HO_2 radical was actually formic acid in the cell or a mixture of HO_2 radical and formic acid. It is impossible to distinguish between the two using UV absorption spectroscopy owing to their similar cross sections. There are other ways to generate HO_2 radical in situ, but those would require a major change in the current experimental set-up, which is beyond the scope of this study. A possible new experimental design and a method to study the binary and ternary nucleation of HO_2 radical is discussed in future work.

4.5 Future work

The binary nucleation of HO_2 radical with water vapor will only occur at low temperatures (<248K). Thus, the new experimental setup requires a cooling jacket to be introduced onto the reaction cell. To introduce a jacket, a different way to photolyze the precursor gas must be used such that the reaction time in the cell can still be varied. One possible way to do that is shown in Figure 24. Instead of creating radicals at different positions along the reaction cell, water can be introduced at different positions along the reaction cell while maintaining a steady state concentration of HO_2 in the cell. This can be achieved by introducing multiple inlet holes along the length of the cell as shown in Figure 24. For photolysing the precursor gas, one can use an XeCl excimer laser (308nm) or XeF excimer laser (351nm) (at 500mJ/pulse with a repetition rate of 100Hz) to initiate HO_2 radical formation while using a D_2 probe beam introduced coaxially into the cell.

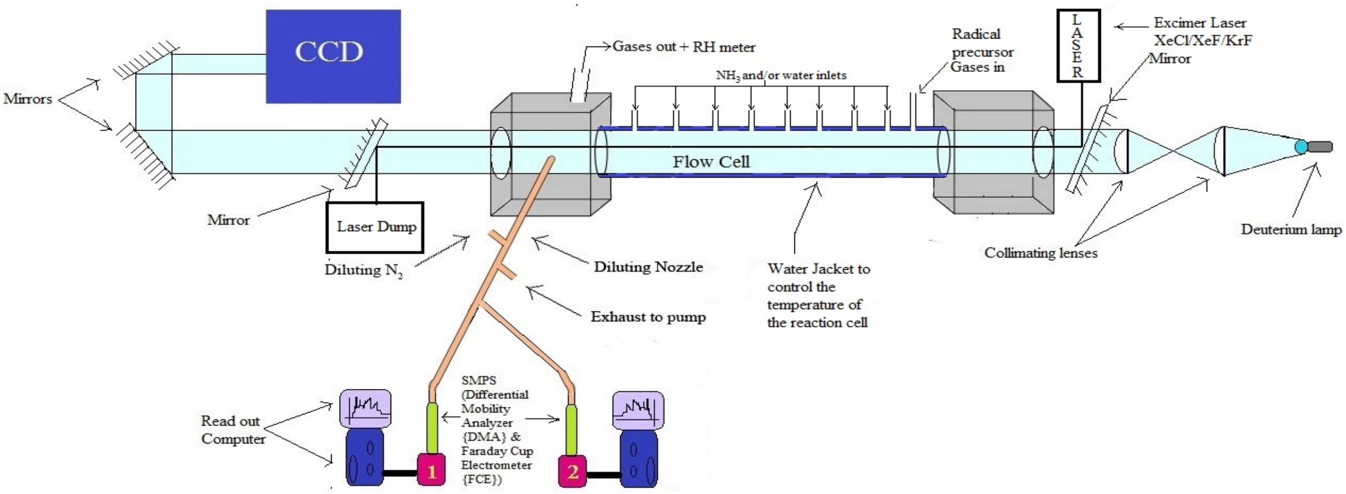

Figure 24 Future experimental set-up to measure binary and ternary nucleation of HO_2 radical with water and ammonia.

To study the ternary nucleation of HO_2 radical in presence of NH_3 and water vapor, a clean way (with minimum secondary chemistry) to produce HO_2

radical must be used. Halogen gases cannot be used as precursor gases to generate HO_2 radical as they would react with NH_3 and form NH_4X (X=F,Cl,Br,I) particles. HO_2 can also be generated by microwave discharging H_2 gas in the presence of O_2. However, a microwave discharge apparatus requires pressures <200 Torr, whereas ternary nucleation must be studied at atmospheric pressures. Other detection methods such as mass spectrometry (MS) can be used to detect HO_2 radical in the system, and in that case, formalin can also be used as a precursor gas to generate HO_2 radical as HO_2 and formic acid will have different m/z signals. But, once again, MS would require very low pressures to be able to detect any signal, which can be a deterrent for use of MS as a detection system.

Another possible method to produce HO_2 is by use of secondary chemistry, where HO_2 is a byproduct of a primary reaction. One such method is to use acetaldehyde as the precursor gas and a KrF excimer laser (248nm) to initiate HO_2 radical via the following reactions.

$$CH_3CHO + h\upsilon \longrightarrow CH_3\bullet + HCO\bullet \tag{4.9}$$

$$CH_3\bullet + O_2 \longrightarrow CH_3O_2\bullet \tag{4.10}$$

$$HCO\bullet + O_2 \longrightarrow H\bullet + CO \tag{4.11}$$

$$H\bullet + O_2 \longrightarrow HO_2\bullet \tag{4.12}$$

These reactions would produce methyl peroxy (CH_3O_2) and hydroperoxy (HO_2) radicals in a 1:1 ratio. Both experimentally and computationally, it has been proven that methyl peroxy radical does not hydrogen bond strongly with water vapor.[37, 42] Thus, the possibility of methyl peroxy radical acting as a nucleating site is minimal. The only species produced from these reactions that can lead to particle formation is HO_2 radical. In conclusion, this new experimental setup has potential for measuring the particle formation initiated by HO_2 radical.

Chapter 5

HNO_3–NH_x, H_2SO_4–NH_x, CH(O)OH–NH_x, And CH_3C(O)OH–NH_x Complexes and Their Role in the Formation of Condensation Nuclei

Disclaimer: The following chapter is presented here in its entirety (with minor changes) from the published version of the paper “Clark J., Kumbhani S., Hansen J., Francisco J. HNO_3NH_x, $H_2SO_4NH_x$, CH(O)OHNH_x, CH_3C(O)OHNH_x complexes and their role in the formation of condensation nuclei. *J. Chem. Phys.* (**2011),** 135, 244305”. I have worked on identifying the global minimum geometries of all the NH_x-acid complexes (section 5.2, 5.3.1, 5.3.2, 5.3.3 and 5.4.1)

Abstract

The formation of sulfuric acid (H_2SO_4), nitric acid (HNO_3), acetic acid (CH_3C(O)OH) and formic acid (HC(O))H) complexes with ammonia (NH_3), amidogen radical (NH_2) and imidogen radical (NH) was studied using Natural Bond Orbital (NBO) calculations. The equilibrium structures, binding energies, and harmonic frequencies were calculated for each acid−NH_x complex using hybrid density functional (B3LYP) and second-order Møller-Plesset perturbation approximation (MP2) methods with the 6-311++G(3df,3pd) basis set. The results presented here suggest that the effects of NH_3 on the formation of new condensation nuclei will be initiated by NH_2, but to a lesser degree and confined primarily to complexes with H_2SO_4 and HNO_3. The NH radical is not expected to play a significant role in the formation of new atmospheric condensation nuclei.

5.1 Introduction

Tropospheric aerosol particles directly affect the radiative balance of the Earth through processes such as light absorption and scattering. Furthermore, aerosol particles indirectly affect the terrestrial radiation budget because they are the precursors to the formation of clouds. Aerosols have also been implicated in adverse human health effects,[93] in the reduction of visibility in urban and regional areas,[94-96] and in acid deposition. At present, researchers do not fully understand the formation of aerosol particles at the molecular level.[97] This lack of understanding creates one of the largest sources of uncertainty in atmospheric models and climate predictions.[98]

The rate of formation of condensation nuclei and the rate at which spontaneous nucleation occurs is dependent upon the specific chemical makeup of the critical nucleus and the atmospheric concentration of the involved gases.[99] The later rate, that of spontaneous nucleation, is significant for simulations of aerosol formation in atmospheric models.[100] Sulfuric acid (H_2SO_4), nitric acid (HNO_3) and ammonia (NH_3) are important precursors in the formation of tropospheric condensation nuclei, precursors to aerosol formation. Atmospheric H_2SO_4 is largely the result of SO_2 emissions from both anthropogenic and biogenic sources. SO_2 is readily oxidized in the atmosphere by OH radical and other oxidizing agents to form SO_3. In the presence of water vapor, SO_3 is quickly converted to H_2SO_4.[101] Nitric acid is a final product of the NO_x oxidation process that is involved in photochemical smog formation.[8]

Ammonia is primarily the result of animal waste, nitrogen based fertilizers and industrial emissions.[102]

It is commonly accepted that the formation of condensation nuclei is the result of gas phase acid/base reactions that take place in the presence of water vapor.[48] The reaction of H_2SO_4 and NH_3 is responsible for the creation of a family of sulfur containing particulates (e.g. NH_4HSO_4 and $(NH_4)_2SO_4$), while the reaction of HNO_3 and NH_3 leads to the formation of particulate ammonium nitrate (NH_4HNO_3). Theoretical methods indicate that the initial step in the reaction of either H_2SO_4 or HNO_3 with NH_3 is thought to take place via the formation of a hydrogen-bonded acid/base complex.[103-105] This structure is described as having a linear or near-linear hydrogen bond involving the acid proton and the lone pair on the ammonia. Rozenberg et al.,[106] using matrix isolation Fourier transform infrared spectroscopy (MIS-FTIR) confirmed the hydrogen-bonded structure of the $H_2SO_4{-}NH_3$ to be that predicted by theory. Namely, a hydrogen-bonded structure with a nearly linear hydrogen-bond.[106] Leopold and Ott obtained microwave spectra of the $HNO_3{-}NH_3$ complex via Fourier transform spectroscopy in a supersonic jet. Their results were consistent with a hydrogen-bonded structure with a near-linear hydrogen bond.[107]

The role of water appears to be the stabilization of the forming acid-ammonia ion pairs. In the case of sulfuric acid, the presence of one molecule of water was shown to be sufficient to convert the $H_2SO_4{-}NH_3$ system from a hydrogen bonded system to one that exists only as an ion pair, the result of complete proton transfer from acid to base.[108] A similar effect was shown for nitric acid, with the exception that two or more water molecules were required to convert the hydrogen bonded HNO_3−NH_3 system to an ion pair.[103, 108]

The oxidation of NH_3 by a hydroxyl radical (OH) leads to the formation of an amidogen radical (NH_2)[109]:

$$NH_3 + OH \rightarrow NH_2 + H_2O \tag{5.1}$$

The formation of NH_2 is not only an important step in the oxidation of NH_3 but is known to be important in the combustion of fossil fuels.[110] NH_2 also plays a key role in the NO_x cycle.[8] When the concentration of NH_3 is elevated, NH_2 may also play a role in the formation of condensation nuclei.

The purpose of the present work is to identify acid−NH_2 [acid = H_2SO_4, HNO_3, HC(O)OH, and $CH_3C(O)OH$] complexes and to compare them to the acid−NH_3 complexes. In addition, acid complexes of the imidogen radical (NH) are also explored. NH concentrations are expected to be low under normal atmospheric conditions and are not expected to play a significant role in the formation of condensation nuclei, but are included for completeness and to help elucidate the manner in which NH_x species affect gas phase acids. Complex formation is analyzed through geometric and natural bond orbital (NBO) analysis. The Gibb's free energy of formation, ΔG_f, is estimated for each complex over the temperature range of 220 – 300 K. Equilibrium constants and dissociation rate constants, as well as, atmospheric lifetime estimates are also presented spanning the same temperatures.

5.2 Method

Calculations were performed using the Gaussian 03, Revision D.01 system of codes.[111] All geometries were fully optimized at the UMP2(full)/6-311++G(3df,3pd) computational level. Harmonic vibrational frequency calculations performed at the B3LYP/6-311++G(3df,3pd) level established the structures as minima and allowed for zero-point corrections to be made to the optimized energies. The counterpoise (CP) procedure[112] was used to further correct the energies for basis set superposition error (BSSE). Electron correlation refinements based on the UMP2 optimized global minimum structures were performed using quadratic configuration interaction with single, double, and triple excitations, QCISD(T), coupled cluster with single, double, and perturbative triple excitations, CCSD(T) methods, and Brueckner Doubles with a triples contribution, BD(T).

Natural energy decomposition analysis (NEDA) calculations were performed at the UB3LYP/6-311++G(3d,3p) level using NBO.5G[113] implemented in Firefly QC package,[114] which is partially based on the GAMESS (US)[115] source code.

Electron density maps with a surface resolution of 0.0009 e/a.u^3 were generated at the MP2(full)/6-311++G(3df,3pd) level using geometries optimized at the same level. Natural bond orbital (NBO) analysis was performed under UMP2(full)/6-311++G(3df,3pd) conditions using the Gaussian implementation of NBO 3.1.[116-121]

The global minimum structure for each complex was arrived at through an extensive RCS methodology. The RCS method generates acid−NH_x complex geometries by randomly packing a previously optimized NH_x molecule within a constrained 3.5-Å radius sphere encompassing the entire optimized acid structure. Each of the twelve optimized complexes presented herein was arrived at via 2,000 random acid−NH_x initial geometries.

All calculations were performed on a super-computing Linux cluster consisting of 320 processing nodes equipped with two quad-core Intel Nehalem processors (2.8 GHz) and 24 GB of memory. All nodes are connected with Infiniband, a high-speed, low-latency copper interconnect

The optimized geometries and harmonic vibrational frequencies are given in Appendix A-3.

5.3 Results and Discussion

5.3.1 Calibration Structures

The gas-phase reactions of H_2SO_4 and HNO_3 with NH_3 are responsible for the creation of sulfur- and nitrogen-containing particulates such as NH_4HSO_4, $(NH_4)_2SO_4$, and NH_4NO_3. Together with H_2SO_4 and HNO_3, these species represent the major forms of sulfur- and nitrogen-containing aerosols[103, 108] and play a key role in the formation of cloud condensation nuclei. H_2SO_4 and HNO_3 form hydrogen bonded complexes with ammonia that may facilitate the formation of condensation nuclei, especially in the presence of water.

Figure 25 schematically represents the MP2(full)/6-311++G(3df,3pd) optimized structures for the H_2SO_4−NH_3 and HNO_3−NH_3 complexes. Included in Figure 25 are the hydrogen bond lengths and angles, gives the change in the O—H bond length, and corrected (zero-point and basis set superposition error) molecular binding energy for each complex. Both complexes are primarily stabilized through strong hydrogen bond interactions with the inorganic acid acting as the hydrogen bond donor and the NH_3 as the acceptor. The bond distances of the main hydrogen bond interactions, r(OH···N) for the H_2SO_4−NH_3 and HNO_3−NH_3 systems are 1.56 Å and 1.66 Å, respectively. Both bond lengths are considerably shorter than the 1.96 Å hydrogen bond length of the water dimer, considered the prototypical hydrogen bonding system.[122-123] Although they look the part, the $O_4 \cdots H_{10}-N_8$ interaction in H_2SO_4−NH_3 and the $O_5 \cdots H_7-N_6$ interaction in HNO_3−NH_3 are not true hydrogen bonding interactions. This will be discussed in a later section. All energy and geometry values are in good agreement with previously published work for the H_2SO_4−NH_3[108] and HNO_3−NH_3[103] systems.

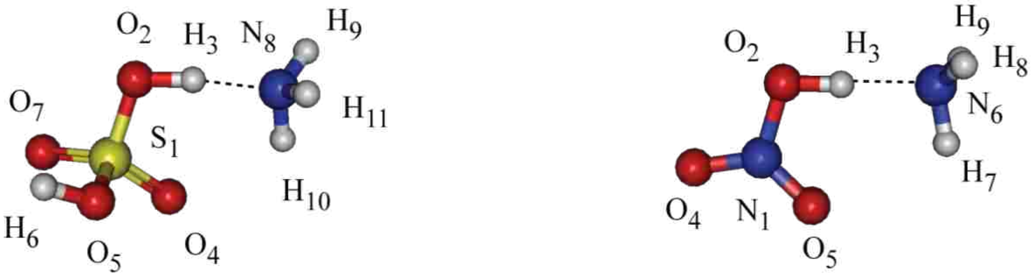

NH_3–H_2SO_4
(-13.6 kcal/mol)

$r(H_3N_8) = 1.56$ Å
$\Theta(O_2H_3N_8) = 172.5°$
$r(O_2H_3) = 1.04$ Å (+ 0.07 Å)

NH_3–HNO_3
(-10.5 kcal/mol)

$r(H_3N_6) = 1.65$ Å
$\Theta(O_2H_3N_6) = 179.4°$
$r(O_2H_3) = 1.02$ Å (+ 0.05 Å)

Figure 25 MP2(full)/6-311++G(3df,3pd) optimized structures for the H_2SO_4–NH_3 and HNO_3–NH_3 complexes. Hydrogen bond lengths and angles for each complex are listed along with the change in the acid-O—H bond length.

Qualitatively, the presence and strength of the hydrogen bond present in each complex can be visualized through electrostatic potential difference maps (EPDMs). EPDMs for the H_2SO_4–NH_3 and HNO_3–NH_3 complexes are shown in Figure 2. Each map has a surface contour resolution of 0.002 e/au^3. Areas of electron density gain are represented by blue regions and those of electron density loss by red regions. Generally, O—H···N hydrogen bonds are evidenced by a region of electron density loss around the proton acceptor atom.[124-125] Moving along the axis of the hydrogen bond towards the bridging hydrogen atom, a region of electron density gain is observed and is followed by another region of electron density loss around the bridging proton. The relative strength of the O—H···N hydrogen bond for each complex can be assessed by comparing the extent of change in the electrostatic potential that results from complex formation. As observed from Figure 26, the amount of electron density change is most severe in the H_2SO_4– NH_3 complex and is less so in HNO_3–NH_3, consistent with the hydrogen bond lengths of the two complexes. It is of note that the EPDMs do not indicate H-bonding for the $O_4 \cdots H_{10}$ and $O_5 \cdots H_7$ interactions.

Quantitatively, the presence and strength of the hydrogen bond interaction can be satisfactorily assessed using Natural Bond Orbital (NBO) theory. From an NBO point of view, a hydrogen bond corresponds to a two-electron intermolecular donor-acceptor interaction of the type, nB → σAH*, where nB typically represents a lone pair of the Lewis base B and σAH* is the unfilled anti-AH bond of the Lewis acid. This type of interaction results in the change of certain geometric, energetic, and dielectric observables that can be used to assess the extent of hydrogen bonding. Table 4 represents details of the interacting nB (in this instance, nB represents lone pair, bonding, and anti-bonding orbitals) and σAH* NBOs and their diagonal and off-diagonal Fock matrix elements. Figure 27 depicts the nB → σAH* (P)NBO 2D-contour diagrams of the leading overlap interaction for each complex and the associated second-order perturbation stabilization energies, $E^{(2)}$, arising from them. The contour diagrams in Figure 27 shows only the atoms that lie in the plane of the O—H···N bonding system. The donating nB (P)NBOs are show in red and the acceptor σAH* (P)NBOs are shown in black. The contours of the $O_4 \cdots H_{10}$–N_8 and $O_5 \cdots H_7$–O_6 interactions are also shown in Figure 27 to demonstrate that these interactions to not represent hydrogen bonding interactions. The (P)NBO overlap integral of the $O_4H_{10}N_8$ is 0.0175 and that of the $O_5H_7O_6$ is 0.0082. To put these values in context, the value of the (P)NBO overlap integral for prototypical hydrogen bond interactions is generally found to be in the range of 0.25 to 0.60, depending on the strength of the interaction.

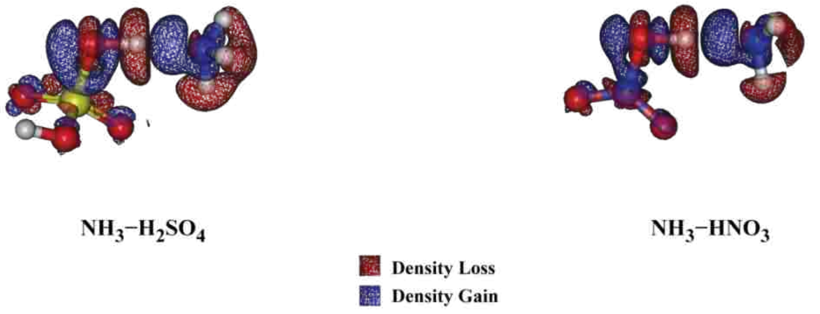

Figure 26 EPDMs for the H_2SO_4–NH_3 and HNO_3–NH_3 complexes, shown with surface contour resolution of 0.002 e/au^3.

Table 4 Summary of major stabilizing NBO interactions between HNO_3, H_2SO_4 and NH_3

Complex	Donor		Acceptor				
	n_B	ε_n (a.u.)	σ_{AH}^*	ε_{σ^*} (a.u.)	$F_{n\sigma^*}$	$E^{(2)}$	$\Sigma(E^{(2)})$
NH_3–H_2SO_4							
major	$(sp^{3.62})_{N(8)}$	-0.557	$0.43(sp^{2.11})O_{(2)} - 0.91(s)H_{(3)}$	0.5423	0.261	74	83.8
minor	$0.84(sp^{2.75})_{N(8)} + 0.55(s)_{H(10)}$	-0.888			0.063	3.5	
other	$0.84(sp^{3.31})_{S(1)} - 0.55(s)_{O(2)}$	0.4526			0.045	2.5	
other	$0.83(sp^{2.86})_{N(8)} + 0.56(s)_{H(9)}$	-0.891			0.042	1.6	
other	$0.83(sp^{2.87})_{N(8)} + 0.56(s)_{H(11)}$	-0.891			0.040	1.4	
other	$0.91(sp^{2.11})_{O(2)} + 0.43(s)_{H(3)}$	-1.036			0.029	0.6	
other	$0.57(sp^{2.35})_{S(1)} + 0.82(s)_{O(7)}$	-1.328			0.028	0.5	
NH_3–HNO_3							
major	$(sp^{3.50})_{N(6)}$	-0.563	$0.44(sp^{2.16})_{O(2)} - 0.90(s)_{H(3)}$	0.5791	0.223	52.5	59.7
minor	$0.83(sp^{2.82})_{N(6)} + 0.56(s)_{H(7)}$	-0.884			0.050	2.1	
other	$0.83(sp^{2.87})_{N(6)} + 0.56(s)_{H(8)}$	-0.886			0.032	0.9	
other	$0.83(sp^{2.87})_{N(6)} + 0.56(s)_{H(9)}$	-0.886			0.032	0.9	

Note: $E^{(2)}$ values reported in kcal mol^{-1}.

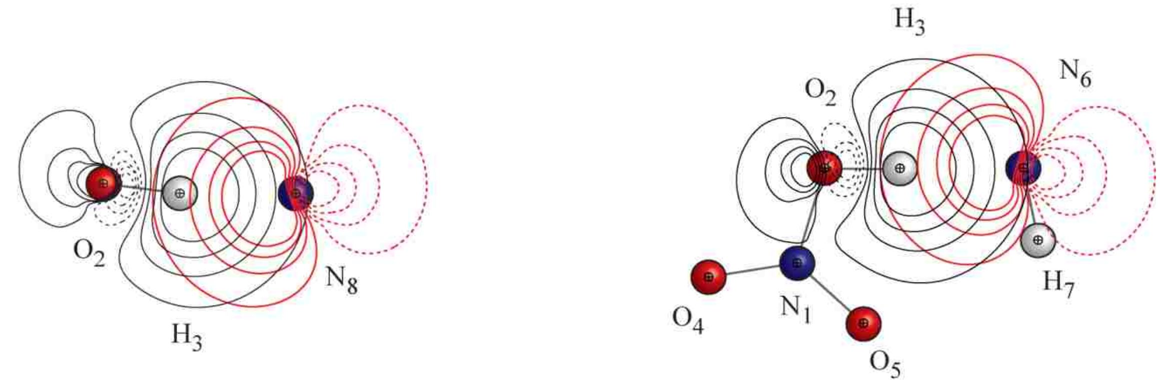

$NH_3 \cdots H_2SO_4$

$n_B \rightarrow \sigma_{AH}^*$ (major)
(73.7 kcal/mol)

$NH_3 \cdots HNO_3$

$n_B \rightarrow \sigma_{AH}^*$ (major)
(52.5 kcal/mol)

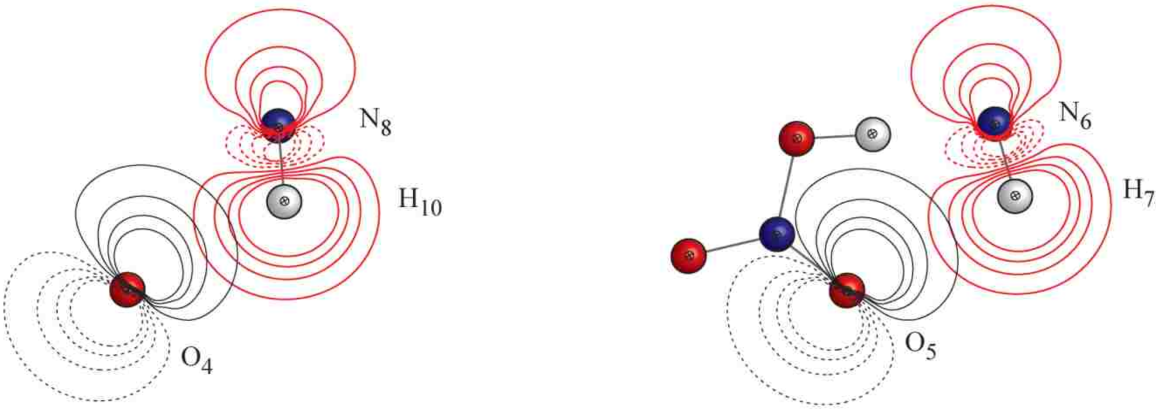

$n_{O4} \rightarrow \sigma_{H10N8}^*$
(0.31 kcal/mol)

$n_{O5} \rightarrow \sigma_{H7N6}^*$
(0.07 kcal/mol)

Figure 27 2D-(P)NBO contour maps of the primary NBO interaction for each complex. The contours of the $O_4 \cdots H_{10}-N_8$ and $O_5 \cdots H_7-N_6$ are also included (bottom half).

The Lewis base and acid of a hydrogen bonded complex will tend towards a linear geometry, as this corresponds to the strongest intermolecular interaction between the acid/base pair as a consequence of maximum nB/σAH* orbital overlap. As can be seen in Figure 25, the (O—H)···N angle for each complex is nearly linear. The bond angle for the O2H3N8 interaction is 172.5° and that of the O2H3N6 interaction is 179.4°. Additionally, the O—H bond length of the Lewis acid will lengthen as a result of the increased occupancy of the σOH* anti-bonding orbital. This lengthening of the O—H bond, shown in Figure 25, leads to the characteristic red-shifting of the O—H vibrational frequency and bond weakening; a change of -1398.8 cm^{-1} and -925.3 cm^{-1} for H_2SO_4−NH_3 and HNO_3−NH_3, respectively. These frequency shifts are in good agreement with those published previously.[103, 108]

Table 5 summarizes the charge transfer, (P)NBO overlap integral for the leading nN→σHO* interaction and the A—H bond ionicity for each complex. In hydrogen bonding, the Lewis acid is expected to become slightly anionic as the Lewis base becomes equally cationic; a result of the nN→σHO* intermolecular charge transfer. The extent of charge transfer from nN to σOH* can be correlated with the extent of overlap between the interacting NBOs. The H_2SO_4−NH_3 complex demonstrates the largest amount of charge transfer as a result of the greatest nN/σOH* overlap. Consequently, the σOH* anti-bond will attempt to repolarize in order to maximize the overlap between the nN and σOH* NBOs, resulting in a withdrawal of electron density from the proton, increasing the ionicity of the O—H bond ($\Delta i_{OH} > 0$). As expected, both complexes experience a positive change in O—H bond ionicity, with that of the H_2SO_4−NH_3 complex being most pronounced.

The formation of H_2SO_4 and HNO_3 hydrogen bonded complexes of NH_3 weakens the O—H bond of the acid. The net result is that the inorganic acid becomes more anionic while the ammonia becomes more cationic, making each complex resemble the ionic forms found in aerosol particles.

Table 5 NBO descriptors showing net intermolecular charge transfer ($\Delta Q_{B \to A}$), bond ionicity (i_{AH}), and the (P)NBO overlap integrals for attractive n_B-σ_{AH}* ($S_{n\sigma}$*) interactions.

Complex	$\Delta Q_{B\to A}$	$S_{n\sigma}$*	Δi_{AH}
NH_3–H_2SO_4			
major	0.1101	0.6078	0.1209
NH_3–HNO_3			
major	0.0803	0.5536	0.1047

NH_x-Acid Complex

As the concentration of NH_3 becomes more elevated in the atmosphere through increases in agricultural activities, on-road vehicle use and other processes,[126] the importance of the gas-phase oxidation products of ammonia become more significant. These products include the amidogen (NH_2) and imidogen (NH) radicals. As the concentration of these radicals increase, so does the likelihood that they may play a more pronounced role in the formation of condensation nuclei. In an effort to ascertain the importance NH_x radicals in the formation of atmospheric condensation nuclei, the gas-phase structures of H_2SO_4−NH_x and HNO_3−NH_x have been identified and are presented here for the first time. In addition, the NH_x complexes of formic acid [HC(O)OH] and acetic acid [$CH_3C(O)OH$] are presented here for the first time.

5.3.2 Equilibrium Structures

Figure 28 presents the three-dimensional structures of the twelve minimum energy acid− NH_x complexes presented in this work. Each complex can be easily described as a typical hydrogen bonded structure stabilized by the presence of a single O—H···N interaction. The hydrogen bond length *r*(H ··· N) and angle Θ(O—H ··· N) of each complex are tabulated in Table 6 (columns 1 and 2). As expected, the hydrogen bond angle approaches linearity, consistent with a maximum in the overlap of n_B and σ_{AH}*. The extent of this overlap is manifest in the magnitude of the corresponding hydrogen bond lengths. In the present context, hydrogen bond length are shortest for those complexes of NH_3 and longest for those of NH, suggesting that the overlap of n_B and σ_{OH}* is greater for NH_3.

Table 6 also lists the *r*(O—H) bond length and the change in this bond length compared with that of the monomer structure (columns 3 and 4). For a given acid series, the *r*(O—H) bond length increases and the hydrogen bond length decreases. The largest change in *r*(O—H) bond length is seen in the H_2SO_4−NH_3 complex, 0.07Å. Such a large change in the O—H bond length results in the weakening of the bond and sets up a scenario where proton transfer from H_2SO_4 is facilitated. Previous work by Larson et al.[108] has shown that the addition of a single water molecule to the system, increases *r*(O—H) by 0.42 Å to 1.46 Å. Such a large *r*(O—H) bond distance indicates that the O—H bond is broken. The net result is the transfer of a proton from H_2SO_4 to NH_3, giving the ion pair, NH_4^+ and HSO_4^-. This suggests that the nucleation of H_2SO_4 in the presence of H_2O is enhanced by the presence of NH_3 because the H_2SO_4−NH_3 structure strongly resembles the ion pair. To a first approximation, the *r*(O—H) bond distance can be taken as a rough indictor as to the effect NH_x has on the nucleation of atmospheric acids.

Table 6 Geometric parameters for the NH_x-Acid complexes

	r(H ··· N), Å	Θ(O—H ··· N), deg.	r(O—H), Å	Δr(O—H), Å	Δν(O—H), cm^{-1}
NH_3–HNO_3	1.66	179.4	1.02	0.05	-925.3
NH_2–HNO_3	1.74	179.6	1.00	0.03	-542.5
NH–HNO_3	1.91	172.5	0.98	0.01	-200.5
NH_3–H_2SO_4	1.56	172.5	1.04	0.07	-1398.8
NH_2–H_2SO_4	1.67	170.3	1.00	0.04	-779.2
NH–H_2SO_4	1.84	176.0	0.98	0.01	-297.6
NH_3–CHO(OH)	1.73	169.0	1.00	0.03	-724.0
NH_2–CHO(OH)	1.81	166.2	0.99	0.02	-407.8
NH–CHO(OH)	1.96	180.0	0.97	0.01	-155.8
NH_3–CH_3CO(OH)	1.75	168.5	1.00	0.03	-651.5
NH_2–CH_3CO(OH)	1.83	165.9	0.98	0.02	-365.7
NH–CH_3CO(OH)	1.98	161.8	0.97	0.01	-148.9
H_2O–H_2O	1.93	173.1	0.97	0.01	-101.3

The final column of Table 6 lists the change in the vibrational frequency of the acid O—H bond. As expected, the most significant change takes place with the NH_3−H_2SO_4 complex, $\Delta\nu = -1398.8\ cm^{-1}$. This is significant, especially when viewed against the change computed for the water dimer, $-101\ cm^{-1}$ (also shown in Table 3 for comparison). This discrepancy can be explained in terms of the magnitude of electron density delocalized into the O−H anti-bond of the acid moiety. In the case of the H_2SO_4−NH_3 complex, an increase of 0.10553 e is observed compared to an increase of only 0.00015 e for the H−O bond of the water dimer. The strength of the O—H···N hydrogen bonding anticipated for the acid−NX_x systems evaluated here demonstrates the importance of the heterogeneous nucleation of acid−NX_x complexes as compared with the homogeneous nucleation of the water dimer.

5.3.3 Binding Energies

Table 7 presents the total corrected binding energy for each complex. The binding energy D_e is determined as the difference between the total energy of the complex and the sum of the total energies of the isolated monomers. The zero-point energy correction is added to D_e to give the zero point energy corrected binding energy D_0. Finally, the basis set superposition error, calculated via the counterpoise method is added to D_o to give the final total corrected binding energy $D_{0,cp}$. As expected, those complexes that manifest the shortest intermolecular hydrogen bond have the largest stabilization energy. The binding energy reveals the stability of each complex. Of all the NH_x complexes examined, the H_2SO_4−NH_3 complex is the most stable, as indicated by the large binding energy, $D_{0,cp}$ = -13.6 kcal/mol. For comparison, a typical hydrogen bond energy, such as in the water dimer, is $D_{0,cp}$ = -2.3 kcal/mol (as calculated and corrected for at the MP2(full)/6-311++G(3df,3pd) level). This large stabilization energy is indicative of a strong hydrogen bond interaction between H_2SO_4 and NH_3, which is in agreement with the unusually short hydrogen bond distance discussed earlier. The significance of the larger association energies of the NH_x–acid complexes leads to the conclusion that the heterogeneous nucleation of these complexes may be much more pronounced than for the homogenous nucleation of water.

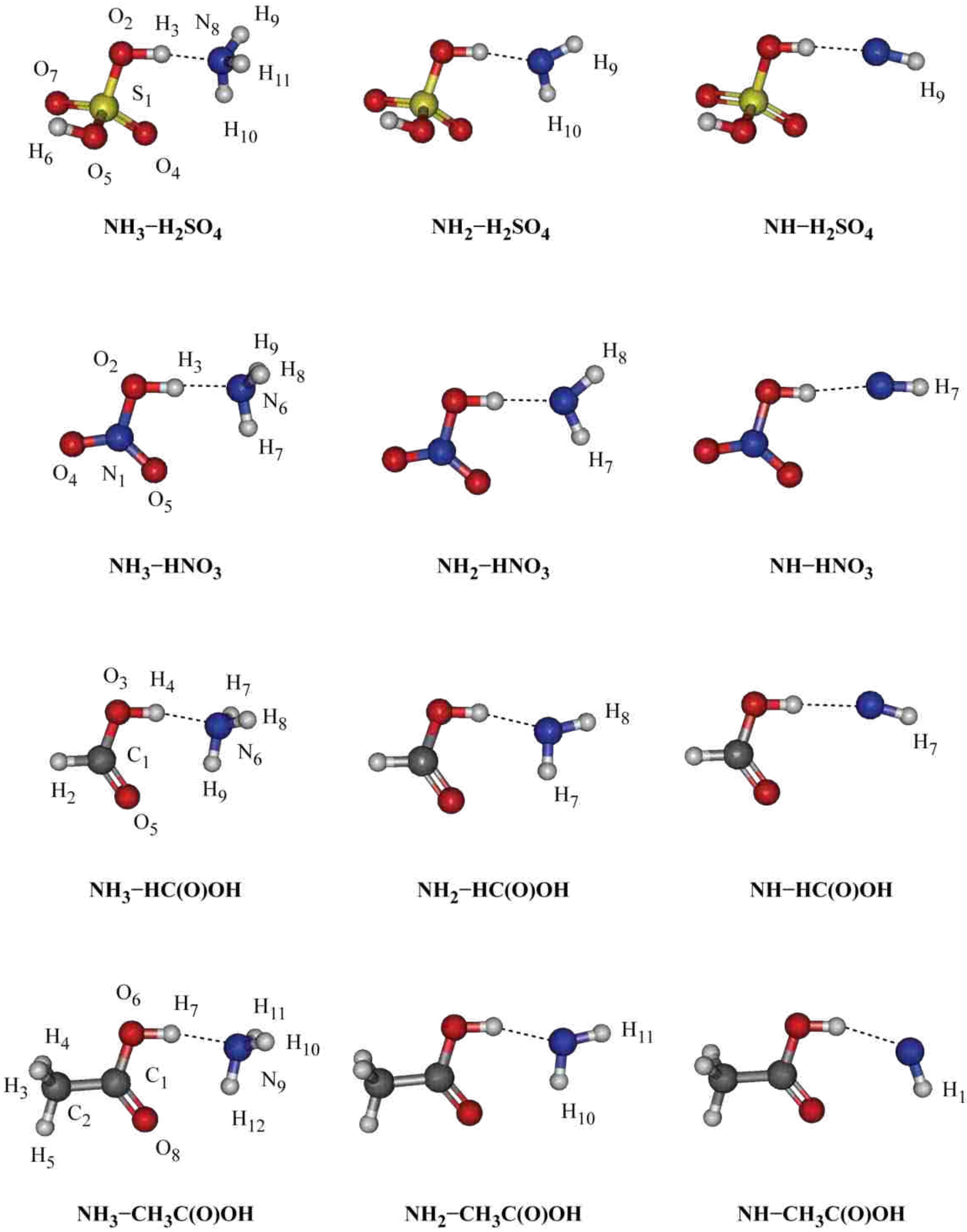

NH_3–H_2SO_4 **NH_2–H_2SO_4** **NH–H_2SO_4**

NH_3–HNO_3 **NH_2–HNO_3** **NH–HNO_3**

NH_3–HC(O)OH **NH_2–HC(O)OH** **NH–HC(O)OH**

NH_3–$CH_3C(O)OH$ **NH_2–$CH_3C(O)OH$** **NH–$CH_3C(O)OH$**

Figure 28 Lowest energy NH_x–acid complexes optimized at the MP2(full)/6-311++G(3df,3pd).

Table 7 Binding energies (kcal/mol) of the NHx–acid complexes. Energies are zero-point energy and BSSE corrected.

	MP2(full)/*//			
	MP2(full)/*	QCISD(T)/*	CCSD(T)/*	BD(T)/*
NH_3–HNO_3	-10.5	-10.1	-10.2	-10.2
NH_2–HNO_3	-7.5	-7.1	-7.1	-7.2
NH–HNO_3	-3.8	-3.5	-3.5	-3.5
NH_3–H_2SO_4	-13.6	-12.8	-12.8	-12.8
NH_2–H_2SO_4	-9.8	-9.1	-9.1	-9.1
NH–H_2SO_4	-4.8	-4.4	-4.4	-4.4
NH_3–CHO(OH)	-8.8	-8.3	-8.2	-8.3
NH_2–CHO(OH)	-6.3	-5.8	-5.8	-5.8
NH–CHO(OH)	-2.9	-2.6	-2.6	-2.6
NH_3–CH_3CO(OH)	-8.3	-7.9	-7.9	-7.9
NH_2–CH_3CO(OH)	-6.0	-5.6	-5.6	-5.6
NH–CH_3CO(OH)	-2.9	-2.9	-2.9	-2.9

* Denotes the 6-311++G(3df,3pd) basis set.

5.3.4 Electron Density difference maps

As shown before in the case of the H_2SO_4−NH_3 and HNO_3−NH_3 complexes, a qualitative way of viewing the extent of the hydrogen bond interaction is by viewing the relevant electron density difference maps. The maps for the 12 NH_x complexes are shown in Figure 29. Looking across an acid series, it is immediately apparent that the extent of change in the electron density is most pronounced in the NH_3 complexes and less so as the multiplicity of the NH_x species increases. This decrease in change as one moves from NH_3 to NH indicates that the n_B and σ_{OH}* overlap is more efficient in the case of complexes of NH_3. These maps also corroborate that each complex is stabilized through the formation of a hydrogen bond, indicated by a region of electron gain around the nitrogen, a region of loss around the proton, and a sequence of regions of electron gain, loss, an gain.[125] The extent of this hydrogen bonding is correlated with the amount of electron density shared between two monomer units.

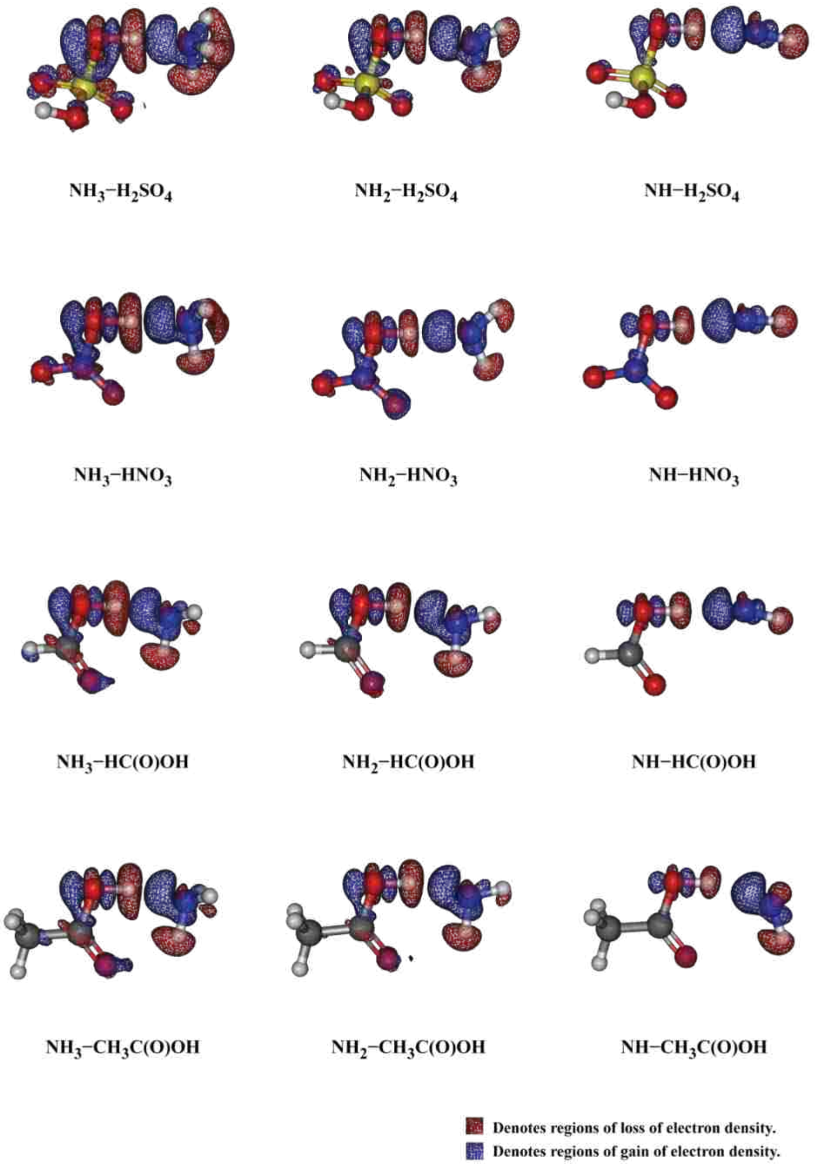

Figure 29 EPDMs for the H_2SO_4–NH_x and HNO_3–NH_x complexes, shown with surface contour resolution of 0.002 e/au^3.

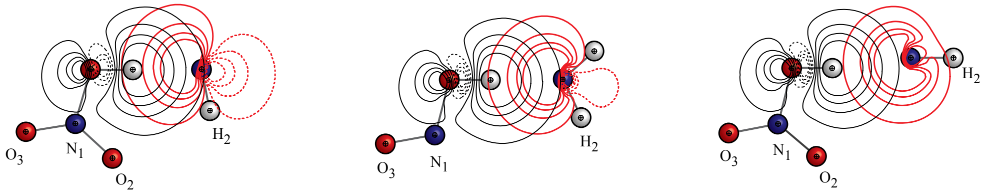

$n_N \rightarrow \sigma_{HO}^*$ (52.5 kcal/mol)
$S_{n\sigma}^*$ (0.5536)
$NH_3 \cdots HNO_3$

$n_N \rightarrow \sigma_{HO}^*$ $(39.3\ \text{kcal/mol})_{total}$
$S_{n\sigma}^*$ (0.4721)
$NH_2 \cdots HNO_3$

$n_N \rightarrow \sigma_{HO}^*$ $(16.7\ \text{kcal/mol})_{total}$
$S_{n\sigma}^*$ (0.2978)
$NH \cdots HNO_3$

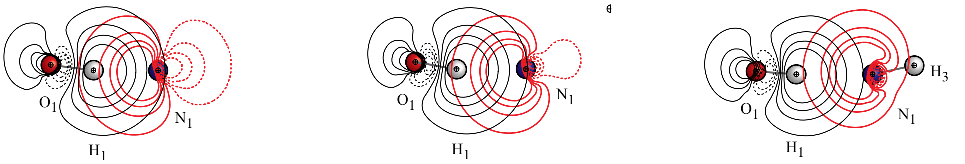

$n_N \rightarrow \sigma_{HO}^*$ (73.7 kcal/mol)
$S_{n\sigma}^*$ (0.6078)
$NH_3 \cdots H_2SO_4$

$n_N \rightarrow \sigma_{HO}^*$ $(50.4\ \text{kcal/mol})_{total}$
$S_{n\sigma}^*$ (0.5201)
$NH_2 \cdots H_2SO_4$

$n_N \rightarrow \sigma_{HO}^*$ $(23.1\ \text{kcal/mol})_{total}$
$S_{n\sigma}^*$ (0.3400)
$NH \cdots H_2SO_4$

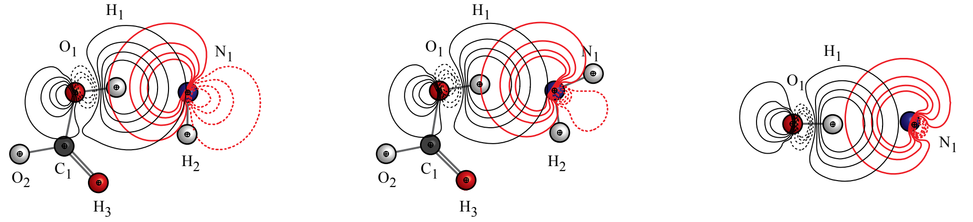

$n_N \rightarrow \sigma_{HO}^*$ (38.7 kcal/mol)
$S_{n\sigma}^*$ (0.4968)
$NH_3 \cdots CHO(OH)$

$n_N \rightarrow \sigma_{HO}^*$ $(26.9\ \text{kcal/mol})_{total}$
$S_{n\sigma}^*$ (0.4042)
$NH_2 \cdots CHO(OH)$

$n_N \rightarrow \sigma_{HO}^*$ $(12.5\ \text{kcal/mol})_{total}$
$S_{n\sigma}^*$ (0.2718)
$NH \cdots CHO(OH)$

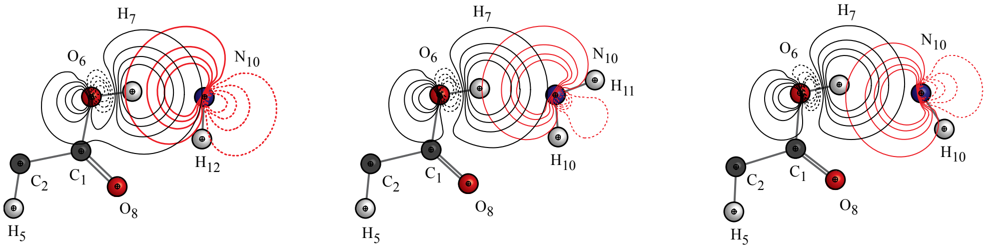

$n_N \rightarrow \sigma_{HO}^*$ (35.4 kcal/mol)
$S_{n\sigma}^*$ (0.4860)
$NH_3 \cdots CH_3CO(OH)$

$n_N \rightarrow \sigma_{HO}^*$ $(24.0\ \text{kcal/mol})_{total}$
$S_{n\sigma}^*$ (0.3881)
$NH_2 \cdots CH_3CO(OH)$

$n_N \rightarrow \sigma_{HO}^*$ $(11.2\ \text{kcal/mol})_{total}$
$S_{n\sigma}^*$ (0.2918)
$NH \cdots CH_3CO(OH)$

Figure 30 2D (P)NBO contour maps of the leading interactions between NH_x and the corresponding acid. The 2nd-order perturbative stabilization energy for each interaction is listed in parenthesis. The orbital overlap integral sum is also listed for each interaction.

5.3.5 Orbital Overlap Diagrams

The leading $n_N \rightarrow \sigma_{XH}^*$ interaction for each complex is illustrated in Figure 30 (only those atoms that lie in the X—H···N plane are depicted). In the case of the NH_2 and NH complexes, only the leading α-spin interaction is depicted. Listed with each overlap image is the second-order perturbative estimate *E(2)* of the stabilization energy arising from the shown interaction and the associated overlap integral $S_{n\sigma}$*. For the NH_2 and NH complexes, the *E(2)* estimate is the total of the α- and β-spin contributions; whereas, $S_{n\sigma}$* represents the interaction shown and is comparable for both spin states. As a point of reference, *E(2)* and $S_{n\sigma}$* for the water dimer are 8.1 kcal/mol and 0.2048, respectively. It is clear from Figure 30 that the short hydrogen bond distances of these complexes is the result of ideal orbital overlap.

As can be seen in Figure 30, the $n_N \rightarrow \sigma_{XH}^*$ interaction becomes less pronounced as the radical nature of the NH_x species increases. As an example, *E(2)* for the H_2SO_4−NH_3 is estimated to be 52.5 kcal mol^{-1}. This interaction is lowered to 39.3 kcal mol^{-1} for NH_2 and 16.7 kcal mol^{-1} for NH. The decrease is a result of poorer overlap between the interacting orbitals. The orbital overlap integral for the $n_N \rightarrow \sigma_{XH}^*$ interaction of the H_2SO_4−NH_x complexes is reduced by 14.7% and 46.2% for NH_2− and NH−, respectively. The result of this reduction is a complex that is less "salt-like" than H_2SO_4−NH_3. However, the resulting NH_x−acid complexes are more "salt like" than the acid monomers taken alone. The result of this reduction is a complex that is less "salt-like" than H_2SO_4−NH_3. However, the resulting NH_x−acid complexes are more “salt like” than the acid monomers taken alone with the result that both NH_2 and NH are expected to play a role in the enhancement of the nucleation of each acid.

5.4 Thermodynamics

5.4.1 Gibbs Free Energies

The binding energies listed in Table 7 represent the BSSE corrected Gibb’s free energy of formation, ΔG_f for each of the acid−NH_x complexes as determined at 0 K ($\Delta G = \Delta H - \Delta S(0\ K)$). To ascertain the importance of complex formation at more elevated, atmospherically relevant temperatures, estimations of ΔG_f for each complex in the temperature range of 220-300 K were made and are listed in Table 8. Complexes of NH_3 with all the acids have strong ΔG_f, even at temperatures as high as 300 K. This is significant because the formation of atmospheric condensation nuclei may be enhanced by complex formation even at elevated temperatures. The Gibb’s energy for complexes of NH_2 is significant for HNO_3 and H_2SO_4 at all of the temperatures listed. Complexes of formic acid and acetic acid are expected to form at temperatures below ~260 K. Above this temperature, the Gibb’s energy is only slightly positive and it may be argued that complex formation is probable for those temperatures within the error of the calculations. Complexes of NH are only predicted to be significant within the temperature range probed for sulfuric acid, and only then at temperatures colder than ~260 K. The data suggest that in general NH complexes are not significant under atmospheric conditions.

5.4.2 Equilibrium and Dissociation Constants

The equilibrium constant, K_{EQ}, and the dissociation rate constant, k_{DISS}, were determined for each NH_x complex and are reported in Table 9. The dissociation rate constant, which uses N_2 as the sole collisional partner, can be seen to increase with temperature as well as the radical nature of the NH_x, which is consistent with the increased thermal energy present at higher temperatures and with the increasingly lower binding energies of NH_2 and NH as compared with NH_3. For $HNO_3{-}NH_3$, k_{DISS} increases from 1.54×10^{-18} cm^3 molecule^{-1} s^{-1} at 220 K to 9.00×10^{-16} cm^3 molecule^{-1} s^{-1} at 300 K. In addition to the expected decrease in k_{DISS} over the temperature range of 220 K to 300K, K_{EQ} is observed to decrease. For $HNO_3{-}NH_3$, K_{EQ} decreases from a value of 1.01×10^{-14} at 220 K to 7.86×10^{-18} at 300 K. The change in both of these quantities will effect the ultimate abundance of each complex under atmospheric conditions.

The abundance of $H_2SO_4{-}NH_3$ and $HNO_3{-}NH_3$ was estimated by employing the K_{EQ} values calculated for each complex and by using concentrations of NH_3,[127] H_2SO_4,[128-129] and HNO_3[130] that are typical of those values measured in the atmosphere. Although the abundance of these species will change with temperature and pressure, constant values for the concentrations of NH_3 (2.46×10^{11} molecules cm^{-3}), H_2SO_4 (2.00×10^{6} molecules cm^{-3}), and HNO_3 (3.35×10^{10} molecules cm^{-3}) were used in all estimates of complex abundance, solely for illustrative purposes. The abundance of the HNO_3–NH_3 complex at 220 K and 300 K was determined to be 9.06×10^7 molecules cm^{-3} and 6.48×10^4 molecules cm^{-3}, respectively. Similarly, the concentration of H_2SO_4–NH_3 was calculated to lie between 4.07×10^6 molecules cm^{-3} at 220 K and 4.33×10^2 molecules cm^{-3} at 300 K.

5.4.3 Lifetime and Collisional Frequency

Atmospheric lifetimes and collisional frequencies for each NH_x complex were calculated over the same 220-300 K temperature range and the results are listed in Table 10. For complexes of NH_x to have an effect on the formation of atmospheric condensation nuclei, they need to exist long enough to experience sufficient collisions with water as to form condensation nuclei. It can be seen by comparison of Tables 7 and 10 that those complexes with the largest binding energies have the longest atmospheric lifetimes. The lifetime of H_2SO_4–NH_3 at 220 K is quite large, 4 s. The collisional frequency will be dependent on the amount of water vapor present and this is in large part dependent of the prevalent temperature. For the estimates given here, a relative humidity of 50% at each temperature was assumed. The lifetime for H_2SO_4–NH_2 complexes are in the millisecond timeframe from 220 – 240 K. This should have both *in situ* and laboratory significance for their direct observation.

Table 8 Gibb's free energy of formation for the NHx acid complexes, as determined at the MP2(full)/6-311++G(3df,3pd) computational level.

	HNO_3			H_2SO_4			HC(O)OH			$CH_3C(O)OH$		
	NH_3	NH_2	NH	NH_3	NH_2	NH	NH_3	NH_2	NH	NH_3	NH_2	NH
220	-6.3	-3.2	0.2	-9.8	-5.7	-1.2	-4.2	-1.7	0.9	-3.6	-1.3	1.4
230	-6.1	-2.9	0.4	-9.5	-5.4	-0.9	-3.9	-1.4	1.2	-3.3	-1.0	1.7
240	-5.8	-2.6	0.7	-9.2	-5.1	-0.7	-3.6	-1.1	1.4	-3.0	-0.7	1.9
250	-5.5	-2.3	0.9	-8.9	-4.8	-0.4	-3.4	-0.8	1.6	-2.7	-0.4	2.2
260	-5.2	-2.1	1.2	-8.6	-4.5	-0.2	-3.1	-0.6	1.9	-2.5	-0.1	2.4
270	-4.9	-1.8	1.4	-8.3	-4.2	0.1	-2.8	-0.3	2.1	-2.2	0.2	2.6
280	-4.6	-1.5	1.6	-8.0	-3.9	0.3	-2.5	0.0	2.3	-1.9	0.5	2.9
290	-4.4	-1.2	1.9	-7.7	-3.6	0.6	-2.2	0.3	2.5	-1.6	0.7	3.1
300	-4.1	-1.0	2.1	-7.4	-3.4	0.8	-1.9	0.6	2.8	-1.3	1.0	3.4

Note: Values are reported in kcal/mol

Table 9 Equilibrium and Dissociation Constants for the NH_x-acid complexes

	HNO_3						H_2SO_4					
	NH_3		NH_2		NH		NH_3		NH_2		NH	
T, K	K_{EQ}	k_{DISS}	K_{EQ}	k_{DISS}	K_{EQ}	k_{DISS}	K_{EQ}	k_{DISS}	K_{EQ}	k_{DISS}	K_{EQ}	k_{DISS}
220	1.01E-14	1.54E-18	1.04E-17	2.65E-16	8.74E-20	3.40E-14	8.27E-12	3.81E-20	3.79E-15	2.19E-17	1.48E-19	9.25E-15
230	3.11E-15	4.51E-18	4.44E-18	5.60E-16	5.08E-20	4.94E-14	1.85E-12	1.54E-19	1.22E-15	5.84E-17	8.39E-20	1.47E-14
240	1.06E-15	1.19E-17	2.05E-18	1.10E-15	3.10E-20	6.91E-14	4.69E-13	5.47E-19	4.30E-16	1.41E-16	4.99E-20	2.22E-14
250	3.95E-16	2.90E-17	1.01E-18	2.03E-15	1.98E-20	9.33E-14	1.33E-13	1.73E-18	1.66E-16	3.15E-16	3.10E-20	3.21E-14
260	1.59E-16	6.51E-17	5.24E-19	3.55E-15	1.31E-20	1.22E-13	4.16E-14	4.96E-18	6.88E-17	6.51E-16	2.00E-20	4.45E-14
270	6.88E-17	1.37E-16	2.87E-19	5.90E-15	8.92E-21	1.56E-13	1.42E-14	1.30E-17	3.06E-17	1.26E-15	1.34E-20	5.96E-14
280	3.16E-17	2.70E-16	1.64E-19	9.39E-15	6.27E-21	1.94E-13	5.25E-15	3.13E-17	1.44E-17	2.30E-15	9.22E-21	7.75E-14
290	1.54E-17	5.05E-16	9.82E-20	1.44E-14	4.53E-21	2.36E-13	2.08E-15	7.02E-17	7.17E-18	3.99E-15	6.53E-21	9.79E-14
300	7.86E-18	9.00E-16	6.08E-20	2.12E-14	3.35E-21	2.82E-13	8.79E-16	1.48E-16	3.75E-18	6.59E-15	4.75E-21	1.21E-13

	HC(O)OH						$CH_3C(O)OH$					
	NH_3		NH_2		NH		NH_3		NH_2		NH	
T, K	K_{EQ}	k_{DISS}	K_{EQ}	k_{DISS}	K_{EQ}	k_{DISS}	K_{EQ}	k_{DISS}	K_{EQ}	k_{DISS}	K_{EQ}	k_{DISS}
220	3.99E-19	1.54E-17	2.56E-19	9.33E-16	1.70E-21	8.57E-14	1.27E-19	1.07E-16	1.15E-19	2.40E-15	1.15E-21	2.75E-14
230	1.87E-19	3.78E-17	1.26E-19	1.76E-15	1.21E-21	1.12E-13	6.23E-20	2.35E-16	5.85E-20	4.15E-15	8.18E-22	3.38E-14
240	9.35E-20	8.51E-17	6.58E-20	3.12E-15	8.97E-22	1.43E-13	3.26E-20	4.80E-16	3.16E-20	6.78E-15	5.98E-22	4.04E-14
250	4.96E-20	1.78E-16	3.63E-20	5.25E-15	6.80E-22	1.77E-13	1.80E-20	9.14E-16	1.79E-20	1.05E-14	4.50E-22	4.71E-14
260	2.77E-20	3.50E-16	2.11E-20	8.41E-15	5.29E-22	2.14E-13	1.04E-20	1.64E-15	1.07E-20	1.56E-14	3.47E-22	5.38E-14
270	1.62E-20	6.49E-16	1.28E-20	1.29E-14	4.20E-22	2.54E-13	6.32E-21	2.78E-15	6.63E-21	2.22E-14	2.74E-22	6.02E-14
280	9.85E-21	1.14E-15	8.04E-21	1.91E-14	3.40E-22	2.96E-13	3.98E-21	4.50E-15	4.27E-21	3.06E-14	2.20E-22	6.64E-14
290	6.21E-21	1.92E-15	5.23E-21	2.74E-14	2.80E-22	3.40E-13	2.59E-21	6.98E-15	2.84E-21	4.09E-14	1.80E-22	7.21E-14
300	4.05E-21	3.11E-15	3.52E-21	3.81E-14	2.34E-22	3.84E-13	1.74E-21	1.04E-14	1.94E-21	5.31E-14	1.50E-22	7.73E-14

* K_{EQ} is reported in cm^3 $molecule^{-1}$.

Table 10 Lifetime and Collisional frequencies for the NHx-acid complexes.

	HNO_3						H_2SO_4					
	NH_3		NH_2		NH		NH_3		NH_2		NH	
T, K	**τ**	v_{coll}	**τ**	v_{coll}	**τ**	v_{coll}	**τ**	v_{coll}	**τ**	v_{coll}	**τ**	v_{coll}
220	1.03E-01	8.85E+03	5.99E-04	1.02E+04	4.67E-06	1.10E+04	4.17E+00	9.89E+03	7.25E-03	1.05E+04	1.72E-05	1.10E+04
230	2.91E-02	3.66E+04	2.34E-04	4.23E+04	2.65E-06	4.55E+04	8.51E-01	4.09E+04	2.25E-03	4.36E+04	8.92E-06	4.54E+04
240	9.18E-03	8.84E+04	9.94E-05	1.02E+05	1.58E-06	1.10E+05	2.00E-01	9.88E+04	7.74E-04	1.05E+05	4.93E-06	1.10E+05
250	3.18E-03	2.34E+05	4.53E-05	2.71E+05	9.87E-07	2.92E+05	5.31E-02	2.62E+05	2.92E-04	2.79E+05	2.87E-06	2.91E+05
260	1.20E-03	6.19E+05	2.19E-05	7.16E+05	6.37E-07	7.71E+05	1.57E-02	6.92E+05	1.19E-04	7.37E+05	1.75E-06	7.68E+05
270	4.86E-04	1.44E+06	1.12E-05	1.67E+06	4.26E-07	1.80E+06	5.12E-03	1.61E+06	5.26E-05	1.72E+06	1.11E-06	1.79E+06
280	2.10E-04	2.99E+06	6.05E-06	3.46E+06	2.93E-07	3.72E+06	1.82E-03	3.34E+06	2.47E-05	3.56E+06	7.33E-07	3.71E+06
290	9.68E-05	5.70E+06	3.41E-06	6.60E+06	2.07E-07	7.10E+06	6.97E-04	6.37E+06	1.23E-05	6.79E+06	4.99E-07	7.08E+06
300	4.70E-05	1.03E+07	2.00E-06	1.19E+07	1.50E-07	1.28E+07	2.86E-04	1.15E+07	6.42E-06	1.23E+07	3.50E-07	1.28E+07

	HC(O)OH						$CH_3C(O)OH$					
	NH_3		NH_2		NH		NH_3		NH_2		NH	
T, K	**τ**	v_{coll}	**τ**	v_{coll}	**τ**	v_{coll}	**τ**	v_{coll}	**τ**	v_{coll}	**τ**	v_{coll}
220	1.03E-02	8.57E+03	1.70E-04	9.95E+03	1.85E-06	1.06E+04	1.49E-03	1.21E+04	6.62E-05	1.37E+04	5.77E-06	1.07E+04
230	3.47E-03	3.54E+04	7.45E-05	4.11E+04	1.17E-06	4.39E+04	5.57E-04	5.02E+04	3.16E-05	5.65E+04	3.88E-06	4.43E+04
240	1.29E-03	8.56E+04	3.51E-05	9.94E+04	7.67E-07	1.06E+05	2.28E-04	1.21E+05	1.62E-05	1.37E+05	2.71E-06	1.07E+05
250	5.16E-04	2.27E+05	1.75E-05	2.63E+05	5.20E-07	2.81E+05	1.01E-04	3.22E+05	8.76E-06	3.62E+05	1.95E-06	2.84E+05
260	2.22E-04	5.99E+05	9.25E-06	6.95E+05	3.63E-07	7.42E+05	4.75E-05	8.49E+05	4.99E-06	9.55E+05	1.45E-06	7.49E+05
270	1.02E-04	1.40E+06	5.13E-06	1.62E+06	2.61E-07	1.73E+06	2.39E-05	1.98E+06	2.98E-06	2.23E+06	1.10E-06	1.75E+06
280	4.97E-05	2.89E+06	2.97E-06	3.36E+06	1.92E-07	3.59E+06	1.26E-05	4.10E+06	1.85E-06	4.61E+06	8.55E-07	3.62E+06
290	2.54E-05	5.52E+06	1.78E-06	6.40E+06	1.44E-07	6.84E+06	7.00E-06	7.82E+06	1.20E-06	8.80E+06	6.78E-07	6.90E+06
300	1.36E-05	9.97E+06	1.11E-06	1.16E+07	1.10E-07	1.24E+07	4.06E-06	1.41E+07	7.97E-07	1.59E+07	5.47E-07	1.25E+07

* Lifetime is reported in s. v_{coll} is reported in collisions/s^{-1}.

5.5 Conclusion

The present work has demonstrated the existence of hydrogen bond stabilized complexes of NH_x with HNO_3, H_2SO_4, formic and acetic acid. The calculated binding energies of all the acid complexes of NH_3 and NH_2 are greater than or equivalent to that of the water dimer, which has a binding energy of -5.0 kcal mol^{-1}.[131] The water dimer is a useful comparison as it is broadly held as the standard for atmospheric hydrogen bonded complexes. The acid−NH complexes have weaker binding energies between -2.9 kcal mol^{-1} and -4.8 kcal mol^{-1}, a result of the double radical nature of the NH diradical.

The results presented here suggest that new condensation nuclei will be primarily initiated by acid complexation with NH_3 and to a lesser degree NH_2 and NH. This can be seen by observing the trend in the change of electron density for a given acid as a function of the multiplicity of NH_x. As the radical nature of NH_x increases, the extent to which electron density is delocalized into a hydrogen bond interaction is decreased. This decrease in electron delocalization is quantitatively expressed by the trend in the (P)NBO overlap integrals and in the 2nd-order perturbative estimates of the stabilization energy.

A mitigating factor for the relevance of NH_2 and NH in the formation of new condensation nuclei will be their respective concentrations at temperatures relevant to the atmosphere. The binding energies expressed for each NH_x−acid complex are based on *ab initio* calculations that assume a temperature of 0 K. The actual formation of each complex will involve interplay between the enthalpies and entropies of formation. The Gibb's free energy of formation for complexes of NH_3 is found to be favorable at all temperatures between 220 and 300 K. The H_2SO_4–NH_2 and HNO_3–NH_2 complexes are also expected to be of importance within the same temperature range and must be considered in nucleation models germane to these acids. The remaining complexes of NH_2 are only expected to be relevant at temperatures below 280 K. The NH radical is only expected to play a role in nucleation in the case of H_2SO_4 and at temperatures below 270 K. However, the full importance of the NH radical in nucleation is expected to be minimal as the atmospheric concentration of this radical species is expected to be very low.

It is of note that Kirkby et al.[48] report that for typical boundary-layer ammonia concentrations, below ~ 1 ppbv, ternary nucleation of NH_3–H_2SO_4–H_2O, is unable to explain the atmospheric observations of increased aerosol formation over that which takes place in the absence of NH_3.[48] They state that these observations imply that additional species, most likely organic compounds, are necessary for boundary-layer nucleation. The results of this study indicate that the formation of condensation nuclei from less reduced NH_x–acid complexes (those of NH_2 and NH) is less likely. This suggests that the inability of NH_3 to explain the increased formation of condensation nuclei, and subsequently new aerosol particles, is a function of the reduced concentration of NH_3 most likely because of its conversion to NH_2 as a result of photolysis or reaction with OH, Cl or NO_3 radicals.

Chapter 6

Summary

Air pollution has been implicated as a cause for various health hazards in humans including, cancer, heart attacks and breathing related diseases. Air pollution also affects the animal and plant world as well. Various chemical and biological models are used by scientists to predict pollution levels and their effects on human, plant and animal health. Unfortunately, these models are not able to predict the observed pollution levels in the atmosphere under all conditions. These models are being constantly updated by atmospheric scientists to better predict pollution levels in the atmosphere. Identifying all the pathways that leads to pollution formation in the atmosphere is critical to improving these models.

Anthropogenic activities in conjunction with radicals are often the primary reason for creating both ozone and particulate matter pollution in the atmosphere. As the climate gets warmer and wetter, water mediated radical chemistry also is affected. Water vapor in the atmosphere has the potential to complex with radicals leading to the formation of radical-water complexes. This dissertation focuses on the role of radical-water complexes in creating ozone and particulate matter pollution in the atmosphere. The first half of this dissertation focuses on ozone pollution created indirectly through the self-reaction of peroxy radicals. Specifically, the effect of water vapor and temperature on the kinetics of the self-reaction of β-hydroxyethyl peroxy radical was studied using both experimental and computational methods. The measured rate constant can be used in scientific models to better predict tropospheric ozone concentrations in the atmosphere. The experimental study shows that the rate of the self-reaction of β-hydroxyethyl peroxy radical increases with increasing water vapor concentration. The increase in the self-reaction was attributed to the formation of a β-hydroxyethyl peroxy radical-water complex. The products of the self-reaction of β-hydroxyethyl peroxy radical could not be identified in the experimental study and thus a computational study was performed to identify the products. Slices of the potential energy surface (PES) for the self-reaction of β-hydroxyethyl peroxy radical were calculated with high level *ab initio* calculations both in the presence and absence of water vapor. The study identified products similar to those observed for other peroxy radicals in the atmosphere. Although in the presence of water vapor a new product pathway was identified that produced hydroperoxy radical as a product as well. The PES study showed that, in the presence of water vapor, an increase in tropospheric ozone is possible. The addition of the water vapor and temperature dependence of the β-hydroxyethyl peroxy self-reaction rate constant to models would improve their ability to predict ozone concentrations and thus help in devising policies to prevent ozone production.

The second half of this dissertation focuses on the role of radical-water complexes in forming aerosol particles in the atmosphere. Similar to ozone production in the atmosphere, atmospheric models under-predict relative to observed concentrations, the number density of aerosols in the atmosphere. The majority of aerosols in the atmosphere are thought to form from the nucleation of sulfuric acid-water complexes. Up to this point, the majority of research on new particle formation in the atmosphere has involved study of sulfuric acid nucleation. However, nucleation by sulfuric acid is not sufficient to explain the observed aerosol concentration in the atmosphere as there is not enough sulfuric acid present to form the observed aerosol concentrations. Various organic compounds and other sulfur compounds have been explored as nucleating agents in an effort to explain the observed aerosol concentrations. This dissertation attempts to identify the role of radical-water complexes to act as nucleating agents to form aerosol particles in the atmosphere. An experimental set-up involving scanning mobility particle sizers as detectors was created to form and measure radical initiated particle formation. The setup uses UV absorption spectroscopy to measure the radical concentration and wavelength modulated IR spectroscopy to measure the water vapor. Hydroperoxy radical (HO_2) was used as the test radical in this study. The hydroperoxy radical-water complex was expected to act as the nucleating site for the formation of aerosol particles, but at room temperature and pressure, no new particle formation was observed. Recent publications on nucleation theory and sulfuric acid aerosol particle formation sheds light on the possible reasons for the observed lack of particle formation in this study. It has been suggested that the binary nucleation of sulfuric acid-water complex does not occur at room temperature, rather a ternary nucleation involving a base like ammonia or amines is responsible for particle formation in the troposphere at room temperatures. At temperatures of the stratosphere, binary nucleation is the major pathway to form aerosol particles. The current experimental set-up does not allow for measurement of the binary nucleation of particle formation at cold temperatures (220-273K) due to the absence of a cooling jacket around the reaction cell. Ternary nucleation also cannot be studied due to the precursor gases used to generate the HO_2 radical in the system. The chlorine gas would react with the base and form ammonium chloride particles in overwhelming amounts, overshadowing the HO_2 radical generated particles. Possible experimental setup changes that would allow for measurement of both binary and ternary nucleation has been discussed in the dissertation.

Ammonia involved in the ternary nucleation process can be photolysed in the atmosphere to form amidogen (NH_2) and imidogen (NH) radicals. The fate of these radicals in the atmosphere is unexplored. The possibility of these radicals to act as nucleating sites by complexing with common acids found in the atmosphere has been explored in this dissertation. The formation of sulfuric acid (H_2SO_4), nitric acid (HNO_3), acetic acid ($CH_3C(O)OH$) and formic acid ($HCO(O))H$) complexes with ammonia, amidogen radical and imidogen radical was studied with high level *ab initio* calculations. Other than the ammonia complexes, H_2SO_4-NH_2 and HNO_3-NH_2 complexes have shown the potential to act as nucleating sites to form aerosols. However, the NH radical is not expected to play a significant role in the formation of atmospheric condensation nuclei.

In conclusion, radical–water complexes play a significant role in the atmosphere. Radical chemistry in the atmosphere is affected by water vapor in the atmosphere. The inclusion of radical – water complex chemistry in atmospheric models will improve the estimation of pollution in the atmosphere. The improved scientific models will help in creating better strategies and policies to reduce pollution in the atmosphere.

References

1. Wang, Y.; Wang, M.; Zhang, R.; Ghan, S. J.; Lin, Y.; Hu, J.; Pan, B.; Levy, M.; Jiang, J. H.; Molina, M. J., Assessing the effects of anthropogenic aerosols on Pacific storm track using a multiscale global climate model. *Proceedings of the National Academy of Sciences* **2014,** *111* (19), 6894-6899. DOI: 10.1073/pnas.1403364111.

2. Cohen, A. J.; Ross Anderson, H.; Ostro, B.; Pandey, K. D.; Krzyzanowski, M.; Künzli, N.; Gutschmidt, K.; Pope, A.; Romieu, I.; Samet, J. M.; Smith, K., The Global Burden of Disease Due to Outdoor Air Pollution. *Journal of Toxicology and Environmental Health, Part A* **2005,** *68* (13-14), 1301-1307. DOI: 10.1080/15287390590936166.

3. Change, I. P. f. C., *Climate Change 2007 - The Physical Science Basis: Working Group I Contribution to the Fourth Assessment Report of the IPCC.* Cambridge University Press: 2007. DOI: citeulike-article-id:1995894.

4. Bromaghin, J. F.; McDonald, T. L.; Stirling, I.; Derocher, A. E.; Richardson, E. S.; Regehr, E. V.; Douglas, D. C.; Durner, G. M.; Atwood, T. C.; Amstrup, S. C., Polar bear population dynamics in the southern Beaufort Sea during a period of sea ice decline. *Ecological Applications* **2015,** *25* (3), 634-651. DOI: 10.1890/14-1129.1.

5. Dockery, D. W.; Pope, C. A.; Xu, X.; Spengler, J. D.; Ware, J. H.; Fay, M. E.; Ferris, B. G.; Speizer, F. E., An Association between Air Pollution and Mortality in Six U.S. Cities. *New England Journal of Medicine* **1993,** *329* (24), 1753-1759. DOI: 10.1056/NEJM199312093292401.

6. Pope, I. C.; Burnett, R. T.; Thun, M. J.; et al., LUng cancer, cardiopulmonary mortality, and long-term exposure to fine particulate air pollution. *JAMA* **2002,** *287* (9), 1132-1141. DOI: 10.1001/jama.287.9.1132.

7. Lozano, R.; Naghavi, M.; Foreman, K.; Lim, S.; Shibuya, K.; Aboyans, V.; Abraham, J.; Adair, T.; Aggarwal, R.; Ahn, S. Y.; AlMazroa, M. A.; Alvarado, M.; Anderson, H. R.; Anderson, L. M.; Andrews, K. G.; Atkinson, C.; Baddour, L. M.; Barker-Collo, S.; Bartels, D. H.; Bell, M. L.; Benjamin, E. J.; Bennett, D.; Bhalla, K.; Bikbov, B.; Abdulhak, A. B.; Birbeck, G.; Blyth, F.; Bolliger, I.;

Boufous, S.; Bucello, C.; Burch, M.; Burney, P.; Carapetis, J.; Chen, H.; Chou, D.; Chugh, S. S.; Coffeng, L. E.; Colan, S. D.; Colquhoun, S.; Colson, K. E.; Condon, J.; Connor, M. D.; Cooper, L. T.; Corriere, M.; Cortinovis, M.; de Vaccaro, K. C.; Couser, W.; Cowie, B. C.; Criqui, M. H.; Cross, M.; Dabhadkar, K. C.; Dahodwala, N.; De Leo, D.; Degenhardt, L.; Delossantos, A.; Denenberg, J.; Des Jarlais, D. C.; Dharmaratne, S. D.; Dorsey, E. R.; Driscoll, T.; Duber, H.; Ebel, B.; Erwin, P. J.; Espindola, P.; Ezzati, M.; Feigin, V.; Flaxman, A. D.; Forouzanfar, M. H.; Fowkes, F. G. R.; Franklin, R.; Fransen, M.; Freeman, M. K.; Gabriel, S. E.; Gakidou, E.; Gaspari, F.; Gillum, R. F.; Gonzalez-Medina, D.; Halasa, Y. A.; Haring, D.; Harrison, J. E.; Havmoeller, R.; Hay, R. J.; Hoen, B.; Hotez, P. J.; Hoy, D.; Jacobsen, K. H.; James, S. L.; Jasrasaria, R.; Jayaraman, S.; Johns, N.; Karthikeyan, G.; Kassebaum, N.; Keren, A.; Khoo, J.-P.; Knowlton, L. M.; Kobusingye, O.; Koranteng, A.; Krishnamurthi, R.; Lipnick, M.; Lipshultz, S. E.; Ohno, S. L.; Mabweijano, J.; MacIntyre, M. F.; Mallinger, L.; March, L.; Marks, G. B.; Marks, R.; Matsumori, A.; Matzopoulos, R.; Mayosi, B. M.; McAnulty, J. H.; McDermott, M. M.; McGrath, J.; Memish, Z. A.; Mensah, G. A.; Merriman, T. R.; Michaud, C.; Miller, M.; Miller, T. R.; Mock, C.; Mocumbi, A. O.; Mokdad, A. A.; Moran, A.; Mulholland, K.; Nair, M. N.; Naldi, L.; Narayan, K. M. V.; Nasseri, K.; Norman, P.; O'Donnell, M.; Omer, S. B.; Ortblad, K.; Osborne, R.; Ozgediz, D.; Pahari, B.; Pandian, J. D.; Rivero, A. P.; Padilla, R. P.; Perez-Ruiz, F.; Perico, N.; Phillips, D.; Pierce, K.; Pope Iii, C. A.; Porrini, E.; Pourmalek, F.; Raju, M.; Ranganathan, D.; Rehm, J. T.; Rein, D. B.; Remuzzi, G.; Rivara, F. P.; Roberts, T.; De León, F. R.; Rosenfeld, L. C.; Rushton, L.; Sacco, R. L.; Salomon, J. A.; Sampson, U.; Sanman, E.; Schwebel, D. C.; Segui-Gomez, M.; Shepard, D. S.; Singh, D.; Singleton, J.; Sliwa, K.; Smith, E.; Steer, A.; Taylor, J. A.; Thomas, B.; Tleyjeh, I. M.; Towbin, J. A.; Truelsen, T.; Undurraga, E. A.; Venketasubramanian, N.; Vijayakumar, L.; Vos, T.; Wagner, G. R.; Wang, M.; Wang, W.; Watt, K.; Weinstock, M. A.; Weintraub, R.; Wilkinson, J. D.; Woolf, A. D.; Wulf, S.; Yeh, P.-H.; Yip, P.; Zabetian, A.; Zheng, Z.-J.; Lopez, A. D.; Murray, C. J. L., Global and regional mortality from 235 causes of death for 20 age groups in 1990 and 2010: a systematic analysis for the Global Burden of Disease Study 2010. *The Lancet* **2012,** *380* (9859), 2095-2128. DOI: http://dx.doi.org/10.1016/S0140-6736(12)61728-0.

8. Finlayson-Pitts, B. J.; Pitts, J. N., *Chemistry of the Upper and Lower Atmosphere: Theory, Experiments and Applications.* 1st ed.; Academic Press: San Diego, 2000.

9. Gu, G.; Adler, R., Large-scale, inter-annual relations among surface temperature, water vapour and precipitation with and without enso and volcano forcings. *Int J Clim* **2012,** *32*, 1782-1791.

10. Curtius, J., Nucleation of atmospheric particles. *EPJ Web of Conferences* **2009,** *1*, 199-209.

11. Heagle, A., Ozone and crop yield *Annual Review of Phytopathology* **1989,** *27*, 397.

12. Avnery, S.; Mauzerall, D. L.; Liu, J.; Horowitz, L. W., Global crop yield reductions due to surface ozone exposure: 2. Year 2030 potential crop production losses and economic damage under two scenarios of O3 pollution. *Atmospheric Environment* **2011,** *45* (13), 2297-2309. DOI: http://dx.doi.org/10.1016/j.atmosenv.2011.01.002.

13. "Climate Change 2013: The Physical Science Basis". IPCC, IPCC, 2013. *Climate Change 2013: The Physical Science Basis. Contribution of Working Group I to the Fifth Assessment Report of the Intergovernmental Panel on Climate Change* **2013,** *Ch.8*, p. 711-714.

14. Mitchell, J. F. B.; Johns, T. C.; Gregory, J. M.; Tett, S. F. B., Climate response to increasing levels of greenhouse gases and sulphate aerosols. *Nature* **1995,** *376* (6540), 501-504.

15. Lave, L. B.; Seskin, E. P., An Analysis of the Association between U.S. Mortality and Air Pollution. *Journal of the American Statistical Association* **1973,** *68* (342), 284-290. DOI: 10.1080/01621459.1973.10482421.

16. Mokdad, A. H.; Marks, J. S.; Stroup, D. F.; Gerberding, J. L., ACtual causes of death in the united states, 2000. *JAMA* **2004,** *291* (10), 1238-1245. DOI: 10.1001/jama.291.10.1238.

17. Lim, S. S.; Vos, T.; Flaxman, A. D.; Danaei, G.; Shibuya, K.; Adair-Rohani, H.; Amann, M.; Anderson, H. R.; Andrews, K. G.; Aryee, M.; Atkinson, C.; Bacchus, L. J.; Bahalim, A. N.; Balakrishnan, K.; Balmes, J.; Barker-Collo, S.; Baxter, A.; Bell, M. L.; Blore, J. D.; Blyth, F.; Bonner, C.; Borges, G.; Bourne, R.; Boussinesq, M.; Brauer, M.; Brooks, P.; Bruce, N. G.; Brunekreef, B.; Bryan-Hancock, C.; Bucello, C.; Buchbinder, R.; Bull, F.; Burnett, R. T.; Byers, T. E.; Calabria, B.; Carapetis, J.; Carnahan, E.; Chafe, Z.; Charlson, F.; Chen, H.; Chen, J. S.; Cheng, A. T.; Child, J. C.; Cohen, A.; Colson, K. E.; Cowie, B. C.; Darby, S.; Darling, S.; Davis, A.; Degenhardt, L.; Dentener, F.; Des Jarlais, D. C.; Devries, K.; Dherani, M.; Ding, E. L.; Dorsey, E. R.; Driscoll, T.; Edmond, K.; Ali, S. E.; Engell, R. E.; Erwin, P. J.; Fahimi, S.; Falder, G.; Farzadfar, F.; Ferrari, A.; Finucane, M. M.; Flaxman, S.; Fowkes, F. G.;

Freedman, G.; Freeman, M. K.; Gakidou, E.; Ghosh, S.; Giovannucci, E.; Gmel, G.; Graham, K.; Grainger, R.; Grant, B.; Gunnell, D.; Gutierrez, H. R.; Hall, W.; Hoek, H. W.; Hogan, A.; Hosgood, H. D., 3rd; Hoy, D.; Hu, H.; Hubbell, B. J.; Hutchings, S. J.; Ibeanusi, S. E.; Jacklyn, G. L.; Jasrasaria, R.; Jonas, J. B.; Kan, H.; Kanis, J. A.; Kassebaum, N.; Kawakami, N.; Khang, Y. H.; Khatibzadeh, S.; Khoo, J. P.; Kok, C.; Laden, F.; Lalloo, R.; Lan, Q.; Lathlean, T.; Leasher, J. L.; Leigh, J.; Li, Y.; Lin, J. K.; Lipshultz, S. E.; London, S.; Lozano, R.; Lu, Y.; Mak, J.; Malekzadeh, R.; Mallinger, L.; Marcenes, W.; March, L.; Marks, R.; Martin, R.; McGale, P.; McGrath, J.; Mehta, S.; Mensah, G. A.; Merriman, T. R.; Micha, R.; Michaud, C.; Mishra, V.; Mohd Hanafiah, K.; Mokdad, A. A.; Morawska, L.; Mozaffarian, D.; Murphy, T.; Naghavi, M.; Neal, B.; Nelson, P. K.; Nolla, J. M.; Norman, R.; Olives, C.; Omer, S. B.; Orchard, J.; Osborne, R.; Ostro, B.; Page, A.; Pandey, K. D.; Parry, C. D.; Passmore, E.; Patra, J.; Pearce, N.; Pelizzari, P. M.; Petzold, M.; Phillips, M. R.; Pope, D.; Pope, C. A., 3rd; Powles, J.; Rao, M.; Razavi, H.; Rehfuess, E. A.; Rehm, J. T.; Ritz, B.; Rivara, F. P.; Roberts, T.; Robinson, C.; Rodriguez-Portales, J. A.; Romieu, I.; Room, R.; Rosenfeld, L. C.; Roy, A.; Rushton, L.; Salomon, J. A.; Sampson, U.; Sanchez-Riera, L.; Sanman, E.; Sapkota, A.; Seedat, S.; Shi, P.; Shield, K.; Shivakoti, R.; Singh, G. M.; Sleet, D. A.; Smith, E.; Smith, K. R.; Stapelberg, N. J.; Steenland, K.; Stockl, H.; Stovner, L. J.; Straif, K.; Straney, L.; Thurston, G. D.; Tran, J. H.; Van Dingenen, R.; van Donkelaar, A.; Veerman, J. L.; Vijayakumar, L.; Weintraub, R.; Weissman, M. M.; White, R. A.; Whiteford, H.; Wiersma, S. T.; Wilkinson, J. D.; Williams, H. C.; Williams, W.; Wilson, N.; Woolf, A. D.; Yip, P.; Zielinski, J. M.; Lopez, A. D.; Murray, C. J.; Ezzati, M.; AlMazroa, M. A.; Memish, Z. A., A comparative risk assessment of burden of disease and injury attributable to 67 risk factors and risk factor clusters in 21 regions, 1990-2010: a systematic analysis for the Global Burden of Disease Study 2010. *Lancet* **2012,** *380* (9859), 2224-60. DOI: 10.1016/s0140-6736(12)61766-8.

18. Cesaroni, G.; Forastiere, F.; Stafoggia, M.; Andersen, Z. J.; Badaloni, C.; Beelen, R.; Caracciolo, B.; de Faire, U.; Erbel, R.; Eriksen, K. T.; Fratiglioni, L.; Galassi, C.; Hampel, R.; Heier, M.; Hennig, F.; Hilding, A.; Hoffmann, B.; Houthuijs, D.; Jöckel, K.-H.; Korek, M.; Lanki, T.; Leander, K.; Magnusson, P. K. E.; Migliore, E.; Ostenson, C.-G.; Overvad, K.; Pedersen, N. L.; J, J. P.; Penell, J.; Pershagen, G.; Pyko, A.; Raaschou-Nielsen, O.; Ranzi, A.; Ricceri, F.; Sacerdote, C.; Salomaa, V.; Swart, W.; Turunen, A. W.; Vineis, P.; Weinmayr, G.; Wolf, K.; de Hoogh, K.; Hoek, G.; Brunekreef, B.; Peters, A., Long term exposure to ambient air pollution and incidence of acute coronary events: prospective cohort study and meta-analysis in 11 European cohorts from the ESCAPE Project. *BMJ : British Medical Journal* **2014,** *348*, f7412. DOI: 10.1136/bmj.f7412.

19. Nawrot, T. S.; Perez, L.; Künzli, N.; Munters, E.; Nemery, B., Public health importance of triggers of myocardial infarction: a comparative risk assessment. *The Lancet 377* (9767), 732-740. DOI: http://dx.doi.org/10.1016/S0140-6736(10)62296-9.

20. Hamilton, E. J., Jr., Water-vapor dependence of kinetics of self-reaction of HO_2 in gas phase. *J. Chem. Phys.* **1975,** *63*, 3682-3683.

21. Cox, R. A.; Burrows, J. P., Kinetics and mechanisim of the disproportionation of ho2 in the gas phase. *J. Phys. Chem.* **1979,** *83*, 2560-2568.

22. DeMore, W. B., Reaction of HO_2 with O_3 and the effect of water-vapor on HO_2 kinetics. *J. Phys. Chem.* **1979,** *83*, 1113-1118.

23. Hamilton, E. J., Jr.; Lii, R., Dependence on H_2O and on NH_3 of kinetics of self-reaction of HO_2 in gas-phase formation of HO_2-H_2O and HO_2-NH_3 complexes. *Int. J. Chem. Kinet.* **1977,** *9*, 875-885.

24. Kircher, C. C.; Sander, S. P., Kinetics and mechanisim of HO_2 and DO_2 disproportionations. *J. Phys. Chem.* **1984,** *88* (10), 2082-91.

25. Lii, R.-R.; Gorse, R. A., Jr. ; Sauer, M. C., Jr.; Gordon, S., Temperature-dependence of the gas-phase self-reaction of HO_2 in the presence of NH_3. *J. Phys. Chem.* **1980,** *84* (8), 813-817.

26. Sander, S. P.; Peterson, M.; Watson, R. T.; Patrick, R., Kinetics studies of the HO_2 + HO_2 and DO_2 + DO_2 reactions at 298 K. *J. Phys. Chem.* **1982,** *86* (8), 1236-1240.

27. Sander, S. P.; Abbat, J.; Burkholder, J. B.; Friedl, R. R.; Kolb, C. E.; Golden, D. M.; Huie, R. E.; Kurylo, M. J.; Moortgat, G. K.; Orkin, V. L.; Wine, P. H., Chemical Kinetics and Photochemical Data for use in Atmospheric Studies. *Evaluation No. 17, JPL publication 10-6* **2011,** *Jet Propulsion Laboratory, Pasadena.*

28. Suma, K.; Sumiyoshi, Y.; Endo, Y., The rotational spectrum of the water-hydroperoxy radical (H2O-HO2) complex. *Science* **2006,** *311* (5765), 1278-1281.

29. Kanno, N.; Tonokura, K.; Tezaki, A.; Koshi, M., Water Dependence of the HO2 Self Reaction: Kinetics of the HO_2-H_2O Complex. *J. Phys. Chem. A* **2005,** *109* (14), 3153-3158.

30. Tang, Y. X.; Tyndall, G. S.; Orlando, J. J., Spectroscopic and kinetic properties of HO_2 radicals and the enhancement of the HO_2 self reaction by CH_3OH and H_2O. *J Phys Chem A* **2011,** *135* (2), 8.

31. Stone, D.; Rowley, D. M., Kinetics of the gas phase HO2 self-reaction: Effects of temperature, pressure, water and methanol vapours. . *Phys Chem Chem Phys* **2005,** *7* (10), 2156.

32. Hansen, J. C.; Francisco, J. S., Radical-molecule complexes: Changing our perspective on the molecular mechanisms of radical-molecule reactions and their impact on atmospheric chemistry. *Chem Phys Chem* **2002,** *3* (10), 833–840.

33. Clark, J.; Call, S.; Austin, D.; Hansen, J., Computational study of isoprene hydroxyalkyl peroxy radical-water complexes ($C_5H_8(OH)O_2$-H_2O). . *J Phys Chem A,* **2010,** *114* 6534–6541.

34. Vaida, V., Perspective: Water cluster mediated atmospheric chemistry. *J Chem Phys* **2011,** *135* (2), 8.

35. Sennikov, P. G.; Ignatov, S. K.; Schrems, O., Complexes and clusters of water relevant to atmospheric chemistry: H2O complexes with oxidants. *Chem Phys Chem* **2005,** *6* (3), 392-412.

36. Staikova, M.; Donaldson, D. J., Water complexes as catalysts in atmospheric reactions. *Physics and Chemistry of the Earth Part C-Solar-Terrestial and Planetary Science* **2001,** *26* (7), 473-478.

37. English, A. M.; Hansen, J. C.; Szente, J. J.; Mariq, A. M., The effects of water vapor on the CH_3O_2 self-reaction and reaction with HO_2. *J Phys Chem A* **2008,** *112* (39), 9220-9228.

38. Grotheer, H. H.; Riekert, G.; Meier, U.; Just, T., Kinetics of the reactions of CH_2OH radicals with O_2 and HO_2. *Phys Chem Chem Phys* **1985,** *89*, 187-191.

39. Stockwell, W. R., On the HO_2+HO_2 Reaction - Its Misapplication in Atmospheric Chemistry Models. *J Geophys Res-Atm* **1995,** *100* (D6), 11695-11698.

40. Butkovskaya, N.; Rayez, M. T.; Rayez, J. C.; Kukui, A.; Bras, G. L., Water vapor effect on the hno_3 yield in the HO_2 + NO reaction: Experimental and theoretical evidence. *J Phys Chem A* **2009,** *113* (42), 11327-11342.

41. Aloisio, S.; Francisco, J. S., Existence of a hydroperoxy and water (HO_2 center dot H_2O) radical complex. *J Phys Chem A* **1998,** *102* (11), 1899-1902.

42. Clark, J.; English, A. M.; Fransisco, J.; Hansen, J. C., Computational Study on the Existence of Organic Peroxy Radical-Water Complexes (RO_2-H_2O). *J. Phys. Chem. A.* **2008,** *112* (7), 1587-1595.

43. Khan, M. A. H.; Cooke, M. C.; Utembe, S. R.; Archibald, A. T.; Derwent, R. G.; Jenkin, M. E.; Morris, W. C.; South, N.; Hansen, J. C.; Francisco, J. S.; Percival, C. J.; Shallcross, D. E., Global analysis of peroxy radicals and peroxy radical-water complexation using the STOCHEM-CRI global chemistry and transport model. *Atmospheric Environment* **2015,** *106* (0), 278-287. DOI: http://dx.doi.org/10.1016/j.atmosenv.2015.02.020.

44. Bohr, F.; Henon, E.; García, I.; Castro, M., Theoretical study of the peroxy radicals RO_2 self-reaction: Structures and stabilization energies of the intermediate RO_4R for various R. *International Journal of Quantum Chemistry* **1999,** *75* (4-5), 671-682. DOI: 10.1002/(SICI)1097-461X(1999)75:4/5<671::AID-QUA34>3.0.CO;2-N.

45. Barnes, I.; Becker, K. H.; Ruppert, L., FTIR product study of the self-reaction of β-hydroxyethl peroxy radicals. *Chemical Physics Letters* **1993,** *203* (2–3), 295-301. DOI: http://dx.doi.org/10.1016/0009-2614(93)85404-C.

46. Henon, E.; Bohr, F.; Chakir, A.; Brion, J., Theoretical study of the methyl peroxy self-reaction: the intermediate structure. *Chemical Physics Letters* **1997,** *264* (6), 557-564. DOI: http://dx.doi.org/10.1016/S0009-2614(96)01378-4.

47. Wei, W.-M.; Zheng, R.-H.; Tian, Y. A. N.; Gu, Z.-H.; Xie, Y.-Y., Theoretical study of self reaction of CH_2ClO_2 radical. *Journal of Theoretical & Computational Chemistry* **2009,** *8* (1), 119-142.

48. Kirkby, J.; Curtius, J.; Almeida, J.; Dunne, E.; Duplissy, J.; Ehrhart, S.; Franchin, A.; Gagne, S.; Ickes, L.; Kurten, A.; Kupc, A.; Metzger, A.; Riccobono, F.; Rondo, L.; Schobesberger, S.; Tsagkogeorgas, G.; Wimmer, D.; Amorim, A.; Bianchi, F.; Breitenlechner, M.; David, A.; Dommen, J.; Downard, A.; Ehn, M.; Flagan, R. C.; Haider, S.; Hansel, A.; Hauser, D.; Jud, W.; Junninen, H.; Kreissl, F.; Kvashin, A.; Laaksonen, A.; Lehtipalo, K.; Lima, J.; Lovejoy, E. R.; Makhmutov, V.; Mathot, S.; Mikkila, J.; Minginette, P.; Mogo, S.; Nieminen, T.; Onnela, A.; Pereira, P.; Petaja, T.; Schnitzhofer, R.; Seinfeld, J. H.; Sipila, M.; Stozhkov, Y.; Stratmann, F.; Tome, A.; Vanhanen, J.; Viisanen, Y.; Vrtala, A.; Wagner, P. E.; Walther, H.; Weingartner, E.; Wex, H.; Winkler, P. M.; Carslaw, K. S.; Worsnop, D. R.; Baltensperger, U.; Kulmala, M., Role of sulphuric acid, ammonia and galactic cosmic rays in atmospheric aerosol nucleation. *Nature* **2011,** *476* (7361), 429-433. DOI: http://www.nature.com/nature/journal/v476/n7361/abs/nature10343.html#supplementary-information.

49. Du, J.; Cooper, F.; Fueglistaler, S., Statistical analysis of global variations of atmospheric relative humidity as obserevd by AIRS. *J Geophys Res-Atm* **2012,** *117*, D12315.

50. Sawada, S.; Totsuka, T., Natural and anthropogenic sources and fate of atmospheric ethylene. *Atmos Environ* **1986,** *20*, 821-832.

51. Vohringer-Martinez, E.; Hansmann, B.; Hernandez, H.; Francisco, J. S.; Troe, J.; Abel, B., Water catalysis of a radical-molecule gas-phase reaction. . *Science* **2007,** *315* (5811), 497-501.

52. Gerber, R. B.; McCoy, A. B.; Garciavela, A., Photochemical reaction in weakly-bound clusters. *Ann. Rev. Phys. Chem.* **1994,** *45*, 275-314.

53. Bauer, D.; Crowley, J. N.; Moortgat, G. K., The UV spectrum of ethyl peroxy radical and its self-reaction kinetics between 218 and 333 K,. *J. Photochem. and Photobiol. A: Chemistry* **1992,** *A65*, 3530-3538.

54. Jenkin, M. E.; Cox, R. A., Kinetics of reactions of methylperoxy and 2-hydroethylperoxy radicals produced by the photolysis of iodomethane and 2-iodoethanol. *J. Phys. Chem.* **1991,** *95*, 3229.

55. Jenkin, M. E.; Hayman, G. D., Kinetics of reactions of primary, secondary and tertiary beta-hydroxyperoxyl radicals - application to isoprene degradation. *J Chem Soc-Faraday Transactions* **1995,** *91* (13), 1911.

56. Jenkin, M. E.; Hurley, M. A.; Wallington, T. J., Investigation of the radical product channel of the $CH_3OCH_2O_2$ + HO_2 reaction in the gas phase. *J Phys Chem A* **2010,** *114* (1), 408.

57. Anastasi, C.; Muir, D. J.; Simpson, V. J.; Pagsberg, P., Spectrum and mutual kinetics of $HOCH_2CH_2O_2$ radicals. *J Phys Chem A* **1991,** *95* (15), 5791.

58. Lightfoot, P. D.; Cox, R. A.; Crowley, J. N.; Destriau, M.; Hayman, G. D.; Jenkin, M. E.; Moortgat, G. K.; Zabel, F., Organic Peroxy radicals: Kinetics, spectroscopy, and tropospheric chemistry. *Atmos. Environ.* **1992,** *26A*, 1805-1961.

59. Murrells, T. P.; Jenkin, M. E.; Shalliker, S. J.; Hayman, G. D., Laser flash-photolysis study of the uv spectrum and kinetics of reactions of $HOCH_2CH_2O_2$ radicals. . *J Chem Soc. -Faraday Transactions* **1991,** *87* (15), 2351-2360.

60. Boyd, A. A.; Lesclaux., R., The temperature dependence of the rate coefficients for beta-hydroxyperoxy radical self-reactions. *Int. J Chem Kin* **1997,** *29* (5), 323-331.

61. Atkinson, R.; Baulch, D. L.; Cox, R. A.; Crowley, J. N.; Hampson, R. F.; Hynes, R. G.; Jenkin, M. E.; Rossi, M. J.; Troe., J., Evaluated kinetic and photochemical data for atmospheric chemistry: Volume iii - gas phase reactions of inorganic halogens. *Atmos Chem and Phys* **2007,** *7*, 981-1191.

62. Frisch, M. J.; Trucks, G. W.; Schlegel, H. B.; Scuseria, G. E.; Robb, M. A.; Cheeseman, J. R.; Montgomery, J. A. J.; Vreven, T.; Kudin, K. N.; Burant, J. C. e. a., *Gaussian 03* **2004**.

63. Chang Kon; Kim, J. W., Chan Kyung; Kim, Effects of the basis set superposition error on optimized geometries of trimer complexes (Part I). *Chemical Physics Letters* **2012,** *545*, 112-117.

64. Hintsa, E. J.; Zhao, X. S.; Lee., Y. T., Photodissociation of 2-bromoethanol and 2-chloroethanol at 193 nm. *J Chem Phys* **1990,** *92* (4), 2280-2286.

65. Keller-Rudek, H.; Moortgat, G. K., Max-Planck Intitut fur Chemie, Atmospheric Chemistry Division. *MPI-Mainz-UV-Vis Spectral Atlas of Gaseous Molecules* **2013**.

66. K Bogumil, J. O., J. Hormann, S. Voigt, P. Speitz, O.C. Fleischmann, A. Vogel, M. Hartmann, H Kromminga, and H. Bovensmann. et. al Measurements of molecular absorption spectra with the sciamachy pre-flight model: Instrument characterization and reference data for atmospheric remote-sensing in the 230-2380 nm region. *J Photochem Photobio A-Chem* **2003,** *157*, 2.

67. Crowley, J. N.; Simon, F. G.; Burrows, J. P.; Moortgat, G. K.; Jenkin, M. E.; Cox, R. A., The HO_2 radical absorption-spectrum measured by molecular modulation, uv diode-array spectroscopy. *J. Photochem. and Photobiol. A: Chem.* **1991,** *60*, 1-10.

68. Rothman, L. S.; Rinsland, C. P.; Goldman, A.; Massie, S. T.; Edwards, D. P.; Flaud, J. M.; Perrin, A.; Camy-Peyret, C.; Dana, V.; Mandin, J. Y.; Schroeder, J.; McCann, A.; Gamache, R. R.; Wattson, R. B.; Yoshino, K.; Chance, K. V.; Jucks, K. W.; Brown, L. R.; Nemtchinov, V.; Varanasi, P., The HITRAN molecular spectroscopic database and HAWKS (HITRAN Atmospheric Workstation): 1996 edition. *J. Quant. Spectrosc. Radiat. Transfer* **1998,** *60* (5), 665-710.

69. Caralp, F.; Forst, W.; Rayez., M. T., Chemical activation in oh radical-oxidation of 1-n-alkenes. *Phys Chem Chem Phys* **2003,** *5* (3), 476-486.

70. Orlando, J. J.; Tyndall, G. S.; Bilde, M.; Ferronato, C.; Wallington, T. J.; Vereecken, L.; Peeters., J., Laboratory and theoretical study of the oxy radicals in the oh- and cl-initiated oxidation of ethene. *J Phys Chem A* **1998,** *102* (42), 8116-8123.

71. S. Aloisio, Y. L., and J. Francisco, Complete active space self-consistent field and multireference configuration interaction studies of the differences between the low lying excited states of HO_2 and HO_2-H_2O. *Journal of Chemical Physics* **1999,** *110* (18), 9017.

72. Kanno, N.; Tonokura, K.; Koshi, M., Equilibrium constant of the HO2-H2O complex formation and kinetics of HO_2+HO_2-H_2O: Implications for tropospheric chemistry. *J Geophys Res-Atm* **2006,** *111* (D20).

73. Garzon, A.; Cuevas, C. A.; Ceacero, A. A.; Notario, N.; Albaladejo, J., Atmospheric reactions Cl + CH_3-$(CH_2)_n$-OH (n=0-4): A kinetic and theoretical study. *J Chem Phys* **2006,** *125*, 104305.

74. Taatjes, C. A.; Christensen, L. K.; Hurley, M. D.; Wallington, T. J., Absolute and Site-Specific Abstraction Rate Coefficients for Reactions of Cl with CH_3CH_2OH, CH_3CD_2OH, and CD_3CH_2OH between 295 and 600 K. *J. Phys. Chem. A* **1999,** *103*, 9805.

75. Bauer, D.; Crowley, J. N.; Moortgat, G. K., The UV absorption spectrum of the ethyl peroxy radical and its self-reaction kinetics between 218 333 K. *J. Photochem Photobiol. A: Chem.* **1992,** *A65*, 329-344.

76. Burrell, E.; Clark, J. C.; Snow, M.; Dumais, H.; Lee, S.-c.; Nielson, B. J.; Osborne, D.; Salamanca-cardona, L.; Zemp, L.; Dabell, R. S.; Hansen, J. C., Computational study of hexanal peroxy radical–water complexes. *International Journal of Quantum Chemistry* **2012,** *112* (8), 1936-1944. DOI: 10.1002/qua.23220.

77. Curtiss, L. A.; Raghavachari, K.; Redfern, P. C.; Rassolov, V.; Pople, J. A., Gaussian-3 (g3) theory for molecules containing first and second-row atoms. *J Chem Phys* **1998,** *109*, 7764-7777.

78. Zhang, R.; Khalizov, A.; Wang, L.; Hu, M.; Xu, W., Nucleation and Growth of Nanoparticles in the Atmosphere. *Chemical Reviews* **2012,** *112* (3), 1957-2011. DOI: 10.1021/cr2001756.

79. Kulmala, M.; Vehkamäki, H.; Petäjä, T.; Dal Maso, M.; Lauri, A.; Kerminen, V. M.; Birmili, W.; McMurry, P. H., Formation and growth rates of ultrafine atmospheric particles: a review of observations. *Journal of Aerosol Science* **2004,** *35* (2), 143-176. DOI: http://dx.doi.org/10.1016/j.jaerosci.2003.10.003.

80. Chen, H.; Ezell, M. J.; Arquero, K. D.; Varner, M. E.; Dawson, M. L.; Gerber, R. B.; Finlayson-Pitts, B. J., New particle formation and growth from methanesulfonic acid, trimethylamine and water. *Physical Chemistry Chemical Physics* **2015,** *17* (20), 13699-13709. DOI: 10.1039/C5CP00838G.

81. Kerminen, V.-M.; Lihavainen, H.; Komppula, M.; Viisanen, Y.; Kulmala, M., Direct observational evidence linking atmospheric aerosol formation and

cloud droplet activation. *Geophysical Research Letters* **2005,** *32* (14), n/a-n/a. DOI: 10.1029/2005GL023130.

82. Ehn, M.; Thornton, J. A.; Kleist, E.; Sipila, M.; Junninen, H.; Pullinen, I.; Springer, M.; Rubach, F.; Tillmann, R.; Lee, B.; Lopez-Hilfiker, F.; Andres, S.; Acir, I.-H.; Rissanen, M.; Jokinen, T.; Schobesberger, S.; Kangasluoma, J.; Kontkanen, J.; Nieminen, T.; Kurten, T.; Nielsen, L. B.; Jorgensen, S.; Kjaergaard, H. G.; Canagaratna, M.; Maso, M. D.; Berndt, T.; Petaja, T.; Wahner, A.; Kerminen, V.-M.; Kulmala, M.; Worsnop, D. R.; Wildt, J.; Mentel, T. F., A large source of low-volatility secondary organic aerosol. *Nature* **2014,** *506* (7489), 476-479. DOI: 10.1038/nature13032.

83. Kulmala, M.; Kontkanen, J.; Junninen, H.; Lehtipalo, K.; Manninen, H. E.; Nieminen, T.; Petäjä, T.; Sipilä, M.; Schobesberger, S.; Rantala, P.; Franchin, A.; Jokinen, T.; Järvinen, E.; Äijälä, M.; Kangasluoma, J.; Hakala, J.; Aalto, P. P.; Paasonen, P.; Mikkilä, J.; Vanhanen, J.; Aalto, J.; Hakola, H.; Makkonen, U.; Ruuskanen, T.; Mauldin, R. L.; Duplissy, J.; Vehkamäki, H.; Bäck, J.; Kortelainen, A.; Riipinen, I.; Kurtén, T.; Johnston, M. V.; Smith, J. N.; Ehn, M.; Mentel, T. F.; Lehtinen, K. E. J.; Laaksonen, A.; Kerminen, V.-M.; Worsnop, D. R., Direct Observations of Atmospheric Aerosol Nucleation. *Science* **2013,** *339* (6122), 943-946. DOI: 10.1126/science.1227385.

84. Patoulias, D.; Fountoukis, C.; Riipinen, I.; Pandis, S. N., The role of organic condensation on ultrafine particle growth during nucleation events. *Atmos. Chem. Phys.* **2015,** *15* (11), 6337-6350. DOI: 10.5194/acp-15-6337-2015.

85. Riva, M.; Budisulistiorini, S. H.; Zhang, Z.; Gold, A.; Surratt, J. D., Chemical characterization of secondary organic aerosol constituents from isoprene ozonolysis in the presence of acidic aerosol. *Atmospheric Environment* (0). DOI: http://dx.doi.org/10.1016/j.atmosenv.2015.06.027.

86. Butkovskaya, N. I.; Kukui, A.; Pouvesle, N.; Le Bras, G., Formation of nitric acid in the gas-phase HO_2+NO reaction: Effects of temperature and water vapor. *Journal Of Physical Chemistry A* **2005,** *109* (29), 6509-6520.

87. Aloisio, S.; Francisco, J. S.; Friedl, R. R., Experimental evidence for the existence of the HO_2-H_2O complex. *J. Phys. Chem. A* **2000,** *104*, 6597-6601.

88. Karlsson, R. S.; Szente, J. J.; Ball, J. C.; Maricq, M. M., Homogeneous Aerosol Formation by the Chlorine Atom Initiated Oxidation of Toluene. *The Journal of Physical Chemistry A* **2001,** *105* (1), 82-96. DOI: 10.1021/jp001831u.

89. Husar, D. E.; Temelso, B.; Ashworth, A. L.; Shields, G. C., Hydration of the Bisulfate Ion: Atmospheric Implications. *The Journal of Physical Chemistry A* **2012,** *116* (21), 5151-5163. DOI: 10.1021/jp300717j.

90. Bustos, D. J.; Temelso, B.; Shields, G. C., Hydration of the Sulfuric Acid–Methylamine Complex and Implications for Aerosol Formation. *The Journal of Physical Chemistry A* **2014,** *118* (35), 7430-7441. DOI: 10.1021/jp500015t.

91. Temelso, B.; Phan, T. N.; Shields, G. C., Computational Study of the Hydration of Sulfuric Acid Dimers: Implications for Acid Dissociation and Aerosol Formation. *The Journal of Physical Chemistry A* **2012,** *116* (39), 9745-9758. DOI: 10.1021/jp3054394.

92. Temelso, B.; Morrell, T. E.; Shields, R. M.; Allodi, M. A.; Wood, E. K.; Kirschner, K. N.; Castonguay, T. C.; Archer, K. A.; Shields, G. C., Quantum Mechanical Study of Sulfuric Acid Hydration: Atmospheric Implications. *The Journal of Physical Chemistry A* **2012,** *116* (9), 2209-2224. DOI: 10.1021/jp2119026.

93. Dockery, D. W.; Pope III, C. A.; Xu, X.; Spengler, J. D.; Ware, J. H.; Fay, M. E.; Ferris, J., B G; Speizer, F. E., An association bewteen air pollution and mortality in six U.S. cities. *New England J. Med.* **1993,** *329*, 1753.

94. Ball, R. J.; Robinson, G. D., The origin of haze in the central United States and its effects on soalr irradiation *J. Appl. Meterol.* **1982,** *21*, 171.

95. Eldering, A.; Larson, S. M.; Hall, J. R.; Hussey, K. J.; Cass, G. R., Development of an improved image processing based visibility model. *Environ. Sci. Technol.* **1993,** *27*, 626.

96. Liepert, B.; Fabian, P.; Grassi, H., *Beitr. Phys. Atmos.* **1994,** *67*, 15.

97. Zhang, R., Getting to the Critical Nucleus of Aerosol Formatkion. *Science* **2010,** *328*, 1366.

98. Solomon, S.; Qin, D.; Manning, M.; Chen, Z.; Maricq, M. M.; Averyt, K. B.; Tignor, M.; Miller, H. L., *Contribution of Working Group I to the Fourth Assessment Report of the Intergovernmental Panel on Climate Change, 2007.* Cambridge University Press: Cambridge, 2007.

99. McGraw, R.; Zhang, R., Multivariate analysis of homogeneous nucleation rate measurements. Nucleation in the p-toluic acid/sulfuric acid/water system *J. Chem. Phys.* **2008,** *128*, 064508.

100. Fan, J.; Zhang, R.; Collins, D.; Li, G., Contribution of secondary condensable organics to new particel formation: A case study in Houstan, Texas. *Geophys. Res. Lett.* **2006,** *33*, L15802.

101. Castleman, A. W.; Dans, R. E.; Mukelwitz, H. R.; Tang, I. N.; Wood, W. P., *Int. J. Chem. Kinet. Symp.* **1975,** *1*, 629.

102. Seinfeld, J. H., *Atmospheric Chemistry and Physics of Air Pollution.* Wiley & Sons: New York, 1986.

103. Nguyen, M.-T.; Jamka, A. J.; Cazar, R. A.; Tao, F.-M., Structure and stability of the nitric acid–ammonia complex in the gas phase and in water. *J. Chem. Phys.* **1997,** *106* (21), 8710-8717.

104. Tao, F.M., Gas phase proton transfer reaction of nitric acid-ammonia and the role of water. *J. Chem. Phys.* **1998,** *108*, 193.

105. Latajka, Z.; Szczesniak, M. M.; Ratajczak, H.; Orville-Thomas, W. J., Properties of strong hydrogen bond systems. II. *Ab initio* SCF-MO study of the hydrogen bond between nitric acid and ammonia. *J. Comput. Chem.* **1980,** *1*, 417.

106. Rozenberg, M.; Loewenschuss, A.; Nielson, C. J., Complexes of molecular and ionic character in the same matrix layer: Infrared studies of the sulfuric acid/ammonia system *J. Phys. Chem. A* **2011,** *115* (23), 5759-5766.

107. Ott, M. E.; Leopold, K. R., A Microwave Study of the Ammonia-Nitric Acid Complex. *J. Phys. Chem. A* **1999,** *103*, 1322-1328.

108. Larson, L. J.; Largend, A.; Tao, F.-M., Structure of the Sulfuric Acid-Ammonia System and the Effect of Water Molecules in the Gas Phase. *J. Phys. Chem. A* **1999,** *103* (34), 6786-6792.

109. Ennis, C. P.; Lane, J. R.; Kjaergaard, H. G.; McKinley, A. J., Identification of the Water Amidogen Radical Complex. *J. Am. Chem. Soc.* **2009,** *131* (4), 1358-1369.

110. Seinfeld, J. H.; Pandis, S., Atmospheric Chemistry and Physics In *Air Pollution to Climate Change*, Wiley & Sons: New York, 1998.

111. Frisch, M. J.; Trucks, G. W.; Schlegel, H. B.; Scuseria, G. E.; Robb, M. A.; Cheeseman, J. R.; Montgomery, J., J. A.; Vreven, T.; Kudin, K. N.; Burant, J. C.; Millam, J. M.; Iyengar, S. S.; Tomasi, J.; Barone, V.; Mennucci, B.; Cossi, M.; Scalmani, G.; Rega, N.; Petersson, G. A.; Nakatsuji, H.; Hada, M.; Ehara, M.; Toyota, K.; Fukuda, R.; Hasegawa, J.; Ishida, M.; Nakajima, T.; Honda, Y.; Kitao, O.; Nakai, H.; Klene, M.; Li, X.; Knox, J. E.; Hratchian, H. P.; Cross, J. B.; Bakken, V.; Adamo, C.; Jaramillo, J.; Gomperts, R.; Stratmann, R. E.; Yazyev, O.; Austin, A. J.; Cammi, R.; Pomelli, C.; Ochterski, J. W.; Ayala, P. Y.; Morokuma, K.; Voth, G. A.; Salvador, P.; Dannenberg, J. J.; Zakrzewski, V. G.; Dapprich, S.; Daniels, A. D.; Strain, M. C.; Farkas, O.; Malick, D. K.; Rabuck, A. D.; Raghavachari, K.; Foresman, J. B.; Ortiz, J. V.; Cui, Q.; Baboul, A. G.; Clifford, S.; Cioslowski, J.; Stefanov, B. B.; Liu, G.; Liashenko, A.; Piskorz, P.; Komaromi, I.; Martin, R. L.; Fox, D. J.; Keith, T.; Al-Laham, M. A.; Peng, C. Y.; Nanayakkara, A.; Challacombe, M.; Gill, P. M. W.; Johnson, B.; Chen, W.; Wong, M. W.; Gonzalez, C.; Pople, J. A. *Gaussian 2003*, Gaussian 2003, revision D.01; Gaussian, Inc: Wallingford, CT, 2004.

112. Latajka, Z.; Scheiner, S. J., Primary and secondary basis set superposition error at the SCF and MP2 levels. H_3N--$Li^+$and H_2O--Li^+ *J. Chem. Phys.* **1987,** *87*, 1194.

113. Glending, E.; Lanids, C. R.; Weinhold, F. *NBO.5G*, NBO 5.G; Theoretical Chemistry Institute and Department of Chemistry: Madison, WI, 2010.

114. Granovsky, A. A. *GAMESS*, Firefly version 7.1.G; Available at: http://classic.chem.msu.su/gran/firefly/index.html; 2010.

115. Schmidt, M. W.; Baldridge, K. K.; Boatz, J. A.; Elbert, S. T.; Gordon, M. S.; Jensen, J. H.; Koseki, S.; Matsunaga, N.; Nguyen, K. A.; Windus, T. L.; Dupuis, M.; Montgomery, J. A., *J. Comput. Chem.* **1993,** *14*, 1347-1363.

116. Curtis, L. A.; Pochatko, D. J.; Reed, A. E.; Weinhold, F., Investigation of the differences in stability of the OC···HF and CO···HF complexes. *J. Chem. Phys.* **1985,** *82*, 2679-2687.

117. Reed, A. E.; Weinhold, F., Natural Bond orbital analysis of near Hartree Fock water dimer *J. Chem. Phys.* **1983,** *78*, 4066-4073.

118. Reed, A. E.; Weinhold, F., Natural localised molecualr orbitals. *J. Chem. Phys.* **1985,** *83*, 1736-1740.

119. Reed, A. E.; Weinstock, R. B.; Weinhold, F., Natural population analysis *J. Chem. Phys.* **1985,** *83* (735-746), 735.

120. Reed, A. E.; Weinhold, F.; Curtis, L. A.; Pochatko, D. J., Natural bond orbital analysis of molecular interactions: Theoretical studies of binary complexes of HF, H_2O, NH_3, N_2, O_2, F_2, CO, and CO_2 with HF, H_2O, and NH_3. *J. Chem. Phys.* **1986,** *84*, 5687-5704.

121. Foster, J. P.; Weinhold, F., Natural Hybrid Orbitals *J. Am. Chem. Soc.* **1980,** *102*, 7211-7218.

122. Kim, K.; Jordan, K. D., Comparison of Density Functional and MP2 Calculations on the Water Monomer and Dimer. *J. Phys. Chem.* **1994,** *98* (40), 10089-10094. DOI: 10.1021/j100091a024.

123. Kim, K. S.; Mhin, B. J.; Choi, U. S.; Lee, K., Ab initio studies of the water dimer using large basis sets: The structure and thermodynamic energies. *J. Chem. Phys.* **1992,** *97* (9), 6649-6662. DOI: 10.1063/1.463669.

124. Gu, Y.; Kar, T.; Scheiner, S. J., Fundamental properties of the CH--O interactions: Is it true hydrogen bond? *J. Am. Chem. Soc.* **1999,** *121*, 9411.

125. Clark, J. M.; Hansen, J. C.; English, A. M.; Francisco, J. S., Computational study of the existance of organic peroxy radical-water complexes (RO_2-H_2O). *J. Phys. Chem. A* **2008,** *112*, 1587-1595.

126. CENRS, *Atmospheric Ammonia: Sources and Fate A Review of Ongoing Federal Research and Future Needs*. NOAA Aeronomy Laboratory: Boulder,

2000.

127. Sather, M. E.; Mathew, J.; Nguyen, N.; Lay, J.; Golod, G.; Vet, R.; Cotie, J.; Hertel, T.; Aaboe, E.; Callison, R.; Adam, J.; Keese, D.; Freise, J.; Hathcoat, A.; Sakizzie, B.; King, M.; Lee, C.; Oliva, S.; San Miguel, G.; Crow, L.; Geasland, F., Baseline ambient gaseous ammonia concentrations in the Four Corners area and eastern Oklahoma, USA. *Journal of Environmental Monitoring* **2008,** *10* (11), 1319-1325.

128. Eisele, F. L.; Tanner, D. J.,Measurement of the gas phase concentration of H_2SO_4 and methane sulfonic acid and estimates of H_2SO_4 production and loss in the atmosphere. *J. Geophys. Res.* **1993,** *98* (D5), 9001-9010.

129. Petaja, T.; Mauldin, R. L. I.; Kosciuch, E.; McGrath, J.; Nieminen, T.; Paasonen, P.; Boy, M.; Adamov, A.; Kotiaho, T.; Kulmala, M., Sulfuric acid and OH concentrations in a boreal forest site. *Atmos. Chem. Phys.* **2009,** *9*, 7435-7448.

130. Danalatos, D.; Glavas, S., Gas phase nitric acid, ammonia and related particulate matter at a Mediterranean costal site, Patras, Greece. *Atmos. Environ.* **1999,** *33*, 3417-3425.

131. Feyereisen, M. W.; Feller, D.; Dixon, D. A., Hydrogen Bond Energy of the Water Dimer. *J. Phys. Chem.* **1996,** *100* (8), 2993-2997. DOI: 10.1021/jp952860l.

Appendix

A-1 Chapter 2 Supporting Information

- *Cartesian coordinates for* β*-HEP and* β*-HEP-water complexes*

β-HEP global minimum geometry

C	-0.06143200	0.91095700	0.78251300
H	0.70537100	1.65989500	1.04911700
H	-0.86691800	0.97296800	1.52817800
C	0.55132200	-0.47919800	0.86575500
H	-0.09928800	-1.23791500	0.41244200
H	0.80278200	-0.74864500	1.89943800
O	1.84550900	-0.54200200	0.18305800
O	1.73483300	-0.30263400	-1.10954000
O	-0.65152700	1.19369700	-0.47426700
H	-0.00588500	0.96509700	-1.15925600

β – HEP local minimum geometry

C	1.301556	0.056602	-2.850408
H	1.778681	0.988648	-2.502920
H	1.285371	0.075554	-3.948210
C	-0.128752	-0.005440	-2.351299
H	-0.605416	-0.967864	-2.571418
H	-0.734926	0.825602	-2.737788
O	-0.074926	0.132617	-0.893954
O	-1.236812	-0.120060	-0.329781
O	2.065346	-1.084651	-2.481584
H	2.154245	-1.101720	-1.520228

β – HEP – water complex global minimum geometry

C	-2.65842400	1.14531100	-0.17809300
H	-2.08483300	1.90020500	0.39036000
H	-3.72901100	1.38968700	-0.08255900
C	-2.44137100	-0.22557100	0.44579100
H	-2.87794000	-1.03309300	-0.15558000
H	-2.78227500	-0.25696900	1.49213600
O	-0.99129900	-0.48192000	0.50419700
O	-0.61784100	-1.37340900	-0.36524300
O	-2.34317600	1.17089400	-1.55988100
H	-1.37005600	1.15884300	-1.65118400
O	0.50582200	0.99954400	-1.65001100
H	0.60005500	0.09319000	-1.31499500
H	0.99660900	1.00896600	-2.48178800

β-HEP-water complex local minimum 1

C	-2.79295000	1.25663300	0.05158200
H	-2.35729700	1.67926500	0.97608900
H	-3.88606500	1.38022100	0.11035500
C	-2.50867400	-0.23381100	-0.00814200
H	-2.77184300	-0.66238900	-0.98440900
H	-2.99370800	-0.78264200	0.81302900
O	-1.05574600	-0.41092600	0.16323200
O	-0.71235200	-1.66513600	0.04268500
O	-2.35633200	1.95282700	-1.10651200
H	-1.39043900	2.07167000	-1.03911300
O	0.45843100	1.91270200	-0.72274500
H	0.49159600	1.05360300	-0.27567600
H	1.10079900	2.46647300	-0.26169600

β-HEP_water complex minimum 2

C	-2.93133700	1.33122600	0.32990900
H	-2.07468600	1.95455500	0.64764100
H	-3.80837200	1.63769200	0.92307200
C	-2.63962600	-0.12504000	0.66042500
H	-3.38465600	-0.80859000	0.23379000
H	-2.50772600	-0.27883200	1.74258700
O	-1.34364900	-0.48585800	0.05818500
O	-1.48146300	-1.29166400	-0.95282100
O	-3.26103500	1.53235600	-1.03293400
H	-2.45196300	1.43642400	-1.57223300
O	-0.96675900	1.02237000	-2.65183900
H	-0.13368700	1.49611200	-2.76795500
H	-0.71444100	0.14482100	-2.32348600

- *Cartesian coordinates of Cl + ClCH2CH2OH reaction*

Chloroethanol

C	0.44609700	0.86646700	0.02950100
H	0.88766100	-0.13346500	-0.03724000
H	-0.64657800	0.79684000	0.03722200
C	0.93941500	1.58997500	1.26299300
H	0.63531000	2.64801700	1.22607700
H	0.45347200	1.11726400	2.13741200
O	2.35442000	1.45508800	1.34092800
H	2.69343800	2.05018500	2.01857000
Cl	0.89393000	1.73152600	-1.50819100

Transition state 1 geometry

C	0.45675400	0.86226900	0.02582500
H	0.70563600	-0.19459900	-0.07241900
H	-0.61940400	0.97234100	0.12057400
C	1.12759100	1.43594500	1.23594600
H	0.69627800	2.70580400	1.34168700
H	0.71466700	1.06214400	2.17653000
O	2.48617100	1.43895200	1.16290300
H	2.87025900	1.68882700	2.01049900
Cl	0.95370900	1.65047900	-1.50486400
Cl	0.15655000	4.10404900	1.63215900

Transition state 2 geometry

C	0.80661500	0.87215400	0.03843700
H	1.26093500	-0.10682900	-0.09279400
H	-0.54453400	0.46755600	0.32540000
C	1.19476300	1.64798700	1.26537800
H	0.63412400	2.58838600	1.30444700
H	0.92733300	1.04203500	2.14000200
O	2.60172200	1.87507800	1.20307800
H	2.88563900	2.28796100	2.02539300
Cl	0.73521100	1.74839000	-1.45861000
Cl	-1.86078800	0.02888200	0.77769000

Transition state 3 geometry

C	0.41403100	0.74566800	0.18451800
H	0.93389100	-0.15166500	0.51628100
H	-0.65066900	0.65693800	0.39843200
C	0.97452000	1.97474000	0.89368500

H	0.54195500	2.88524900	0.44018600
H	0.68521300	1.96512100	1.95339000
O	2.34260500	2.13495300	0.74334500
H	3.01723800	1.82728400	1.78427500
Cl	0.59577100	0.84081500	-1.60646200
Cl	3.56228400	0.93988600	2.78487000

A-2 Chapter 3 Supporting Information

The Cartesian coordinates for all the reactant geometries including β-HEP and β-HEP-water complex are provided above. Global minimum geometries were used for both the complexes.

- *Cartesian coordinates of the Intermediate geometries*

Intermediate I

C	1.41074700	1.30063800	-2.97172300
H	1.31218600	2.39072600	-2.83979600
H	1.64425800	1.10256300	-4.02599100
C	0.09147100	0.61672800	-2.63912000
H	0.17960200	-0.47248900	-2.74289400
H	-0.71041100	0.99654200	-3.29027000
O	-0.18217700	0.96938500	-1.27189600
O	-1.44916100	0.36680400	-0.87833500
O	2.50303100	0.78800100	-2.21550700
H	2.35795800	1.01104500	-1.28747000
C	0.49777800	-3.61738300	-1.09841100
H	-0.20226600	-4.33988900	-0.64742800
H	1.51950600	-3.98890100	-0.94603400
C	0.37160000	-2.26959500	-0.40130600
H	1.04457700	-1.53046400	-0.85461600
H	0.58902700	-2.37284100	0.67262100
O	-0.99976500	-1.87688700	-0.58572600
O	-1.21257800	-0.59571900	0.07379100
O	0.30864500	-3.52900100	-2.50699600
H	-0.60620000	-3.26867400	-2.67245100

Intermediate II

C	1.09859800	-0.00659300	-3.79376200
H	2.01641500	0.44610600	-3.38071200
H	0.84387700	0.52780600	-4.71851600
C	-0.04844100	0.16640900	-2.80952200
H	-0.94563200	-0.36212800	-3.15818400
H	-0.26858100	1.23275200	-2.64931100
O	0.40102700	-0.43035900	-1.57780400
O	-0.72748800	-0.56779300	-0.69128500
O	1.31353300	-1.36271300	-4.16069600
H	1.50267000	-1.86850600	-3.35997800
C	1.79135400	1.05219300	2.47128700
H	1.13214000	1.47097200	3.25042800
H	2.71940300	1.63901200	2.45799500
C	1.12420700	1.18202700	1.11037800
H	1.71454100	0.67758700	0.33630700
H	0.96798800	2.24062200	0.85311600
O	-0.15486500	0.52944000	1.25261300
O	-0.89183100	0.62635600	0.02687800
O	2.16912700	-0.28418100	2.77827700
H	1.37565900	-0.83465900	2.77154100

Intermediate III

C	1.43878800	0.82205300	-2.60281700
H	1.95539700	0.96775200	-1.63902500
H	1.33321400	1.80330700	-3.08395900
C	0.04883700	0.25579800	-2.35907300
H	-0.44961100	0.01399100	-3.30753900
H	-0.56048200	0.95664300	-1.76959600
O	0.25103100	-0.95842200	-1.60886600
O	-0.97871300	-1.68236300	-1.55233300

O	2.21483100	0.02342500	-3.48785000
H	2.30205600	-0.85783700	-3.10279700
C	-1.61821400	-3.34733600	2.36560700
H	-0.53088900	-3.30561300	2.54720300
H	-1.95157000	-4.38017000	2.53161700
C	-1.91135600	-2.97558200	0.92060300
H	-2.99339300	-2.91748200	0.74094200
H	-1.44261400	-3.69209400	0.23008100
O	-1.33031200	-1.67012600	0.73074000
O	-1.77659600	-1.13711800	-0.51677500
O	-2.32782000	-2.54244500	3.29938300
H	-2.07458400	-1.62119300	3.15913700

Intermediate IV

C	-2.69717600	0.79952900	0.01883800
H	-2.30800900	1.42771700	0.83807600
H	-3.79458900	0.85955400	0.05289300
C	-2.33178300	-0.66312000	0.26773000
H	-2.54768700	-1.26793400	-0.62162400
H	-2.86497900	-1.05351300	1.14635300
O	-0.90678300	-0.71376500	0.52876300
O	-0.47751300	-2.12352900	0.50672500
O	-2.29685400	1.27571400	-1.24924200
H	-1.33549800	1.43640600	-1.24373200
O	0.54711100	1.32515800	-0.94655200
H	0.45941500	0.45049500	-0.53675900
H	1.14994200	1.20947900	-1.69015900
C	0.31820000	-0.47946500	3.94262300
H	1.28636300	-0.10072400	3.57117800
H	0.24899100	-0.23221900	5.01235900
C	0.28834400	-1.99443900	3.80516500

H	-0.68660200	-2.40997000	4.09477100
H	1.06446000	-2.44808800	4.44096800
O	0.62591300	-2.46425900	2.48463300
O	-0.62740300	-2.67683500	1.74107500
O	-0.76867900	0.17271400	3.30621600
H	-0.70996200	-0.00887700	2.35581300

Intermediate V

C	-1.07607300	2.20349100	-1.12684900
H	-0.12715000	2.39748500	-1.64881200
H	-1.28808700	3.02000100	-0.42453000
C	-1.01724700	0.89183300	-0.41432700
H	-1.85512300	0.50460100	0.16995100
H	-0.91432000	-1.16967900	1.32573900
O	-0.04935300	0.13214200	-0.66377800
O	-0.17513500	-1.21082900	-0.26138300
O	-2.18706400	2.10585100	-2.00975500
H	-2.14138200	1.24883600	-2.47418700
O	-1.90575600	-0.80821600	-2.52171500
H	-1.35988400	-1.30390800	-1.87826100
H	-2.53403700	-1.44316900	-2.88228000
C	0.97206900	1.28747600	3.92270400
H	1.29661100	1.93263800	3.08699400
H	1.84769200	1.08731700	4.55425200
C	0.44602700	-0.03135100	3.38084500
H	0.04492000	-0.65471600	4.19197100
H	1.23548800	-0.57982800	2.84131700
O	-0.62013700	0.30766600	2.48550200
O	-1.35540600	-0.90155000	2.17583100
O	0.02329800	1.95994600	4.74408300
H	-0.81638900	1.98055200	4.26676900

- *Cartesian coordinates of the product geometries*

1. RO

C	0.497778	-3.617383	-1.098411
H	-0.202266	-4.339889	-0.647428
H	1.519506	-3.988901	-0.946034
C	0.371600	-2.269595	-0.401306
H	1.044577	-1.530464	-0.854616
H	0.589027	-2.372841	0.672621
O	-0.999765	-1.876887	-0.585726
O	0.308645	-3.529001	-2.506996
H	-0.606200	-3.268674	-2.672451

2. RO$_2$R

C	1.373876	1.839829	-2.359016
H	1.116647	2.740503	-1.777611
H	1.708573	2.158530	-3.354831
C	0.140798	0.962587	-2.528759
H	0.385555	0.049095	-3.086033
H	-0.656244	1.519705	-3.044135
O	-0.277634	0.637070	-1.191783
O	2.468433	1.143877	-1.771359
H	2.226838	0.912108	-0.865841
C	0.593235	-3.285067	-1.178524
H	-0.106809	-4.007574	-0.727542
H	1.614963	-3.656586	-1.026147
C	0.467058	-1.937280	-0.481420
H	1.140034	-1.198149	-0.934729
H	0.684484	-2.040526	0.592508

O	-0.904308	-1.544572	-0.665839
O	0.404102	-3.196686	-2.587110
H	-0.510743	-2.936359	-2.752565

3. RCHO

C	2.203491	-1.126849	-1.076073
H	2.397485	-1.648812	-0.127150
H	3.020001	-0.424530	-1.288087
C	0.891833	-0.414327	-1.017247
H	0.504601	0.169951	-1.855123
O	0.132142	-0.663778	-0.049353
O	2.105851	-2.009755	-2.187064
H	1.248836	-2.474187	-2.141382

4. ROH

C	1.287476	3.922704	0.972069
H	1.932638	3.086994	1.296611
H	1.087317	4.554252	1.847692
C	-0.031351	3.380845	0.446027
H	-0.654716	4.191971	0.044920
H	-0.579828	2.841317	1.235488
O	0.307666	2.485502	-0.620137
O	1.959946	4.744083	0.023298
H	1.980552	4.266769	-0.816389
H	0.621845	1.655756	-0.253512

5. O2

O	-2.123529	0.506725	-0.477513
O	-2.676835	1.741075	-0.627403

6. RCHO – Water complex

C	2.203491	-1.126849	-1.076073
H	2.397485	-1.648812	-0.127150
H	3.020001	-0.424530	-1.288087
C	0.891833	-0.414327	-1.017247
H	0.504601	0.169951	-1.855123
O	0.132142	-0.663778	-0.049353
O	2.105851	-2.009755	-2.187064
H	1.248836	-2.474187	-2.141382
O	-0.808216	-2.521715	-1.905756
H	-1.303908	-1.878261	-1.359884
H	-1.443169	-2.882280	-2.534037

7. RO – water complex

C	0.799529	0.018838	-2.697176
H	1.427717	0.838076	-2.308009
H	0.859554	0.052893	-3.794589
C	-0.663120	0.267730	-2.331783
H	-1.267934	-0.621624	-2.547687
H	-1.053513	1.146353	-2.864979
O	-0.713765	0.528763	-0.906783
O	1.275714	-1.249242	-2.296854
H	1.436406	-1.243732	-1.335498
O	1.325158	-0.946552	0.547111
H	0.450495	-0.536759	0.459415
H	1.209479	-1.690159	1.149942

8. HO2

O	1.56872400	-0.05429300	-3.19861800

O	2.02359700	-0.70244500	-2.13252500
H	2.27806400	0.57552000	-3.44217300

A–3 Chapter 5 Supporting Information

Table S.I.

NH_x geometries
MP2(full)/6311++G(3df,3dp).

NH_3				
	N	-2.4015	-1.2103	-0.1686
	H	-2.8309	-0.3889	-0.5709
	H	-2.9646	-1.4774	0.6267
	H	-2.4855	-1.9508	-0.8510
NH_2				
	N	1.9584	2.7608	0.1381
	H	1.3377	3.4071	-0.3507
	H	2.7734	3.3357	0.3549
NH				
	N	-1.7910	1.2362	2.3826
	H	-2.7594	1.3074	2.7235

Table S.II. Acid geometries MP2(full)/6-311++G(3df,3dp).

H_2SO_4				
	S	-0.1158	0.4446	-0.0874
	O	-0.4142	-0.9882	0.5081
	H	0.3801	-1.3029	0.9581
	O	0.8656	1.0768	0.7150
	O	0.6144	0.0932	-1.4440
	H	-0.0571	-0.0999	-2.1106
	O	-1.3846	1.0007	-0.3831
HNO_3				
	N	0.2770	-0.0788	-0.2241
	O	0.6465	0.6738	0.8904
	H	-0.2038	0.8173	1.3324
	O	1.1956	-0.3771	-0.9312
	O	-0.9024	-0.3231	-0.3218
HC(O)OH				
	C	0.2939	-1.7676	2.1457
	H	-0.0933	-2.7870	2.2023
	O	0.0614	-1.2619	0.9273
	H	0.4203	-0.3640	0.9276
	O	0.8446	-1.1884	3.0406
$CH_3C(O)OH$				
	C	0.8359	0.0000	0.0536
	C	0.7660	0.0000	-1.4382
	H	0.2201	-0.8767	-1.7762
	H	0.2201	0.8767	-1.7762
	H	1.7672	0.0000	-1.8493
	O	-0.3985	0.0000	0.6020

H	-0.2628	0.0000	1.5583
O	1.8406	0.0000	0.7189

Table S.III. NH_x-H_2SO_4 geometries MP2(full)/6-311++G(3df,3dp).

NH_3-H_2SO_4				
	S	-0.3714	0.0573	-0.1700
	O	-0.2340	-1.3400	-0.8034
	H	0.6989	-1.7278	-0.5631
	O	0.4973	0.1606	0.9562
	O	0.2914	1.0089	-1.2616
	H	-0.3749	1.1928	-1.9345
	O	-1.7539	0.3763	-0.0943
	N	2.0904	-2.1917	-0.0381
	H	2.1159	-3.1237	0.3542
	H	2.2316	-1.5281	0.7163
	H	2.8654	-2.1041	-0.6821
NH_2-H_2SO_4				
	S	-0.2320	-0.1661	0.9821
	O	1.1096	-0.3595	0.2278
	H	1.6958	0.4352	0.4084
	O	-0.0242	0.6654	2.1180
	O	-1.0701	0.7365	-0.0214
	H	-1.4512	0.1586	-0.6937
	O	-0.8568	-1.4381	1.0625
	N	2.5140	1.7919	0.9414
	H	3.3378	2.3470	0.7252
	H	2.0767	2.2023	1.7649
NH-H_2SO_4				
	S	-0.1412	0.4547	-0.0858
	O	-0.3834	-0.9615	0.5313
	H	0.4379	-1.2559	0.9773
	O	0.8052	1.1583	0.7034

O	0.6246	0.1117	-1.4317
H	-0.0315	-0.1418	-2.0927
O	-1.4221	0.9668	-0.4161
N	2.0108	-1.6841	1.8225
H	2.9195	-1.7109	2.2955

Table S.IV. NH_x-HNO_3 geometries
MP2(full)/6-311++G(3df3,dp).

NH_3-HNO_3

N	0.1805	0.8755	-0.0099
O	0.1030	-0.4208	0.3849
H	-0.8467	-0.7118	0.1722
O	1.2507	1.3999	0.1661
O	-0.8245	1.3662	-0.4938
N	-2.3927	-1.2032	-0.1683
H	-2.7829	-0.3585	-0.5682
H	-2.9623	-1.4590	0.6277
H	-2.4828	-1.9397	-0.8559

NH_2-HNO_3

N	-0.0156	0.0295	0.0004
O	1.2224	0.1412	0.5662
H	1.4857	1.0888	0.4097
O	-0.5125	-1.0632	0.0873
O	-0.4705	1.0302	-0.5198
N	1.9582	2.7447	0.1421
H	1.2741	3.3095	-0.3581
H	2.7470	3.3562	0.3404

NH-HNO_3

N	0.2918	-0.0793	-0.2279
O	0.6075	0.6666	0.8871
H	-0.2567	0.8084	1.3246
O	1.2353	-0.3644	-0.9137
O	-0.8798	-0.3507	-0.3761
N	-1.8149	1.2130	2.3503
H	-2.7206	1.3622	2.8075

Table S.V. NH_x-HC(O)OH geometries MP2(full)/6-311++G(3df,3dp).

NH_3-HC(O)OH				
	C	-1.5449	1.8578	0.4549
	H	-2.0929	2.6793	-0.0159
	O	-1.4791	0.8134	-0.3514
	H	-0.9713	0.0907	0.1202
	O	-1.0744	1.9290	1.5677
	N	-0.0735	-0.9381	1.1808
	H	-0.5194	-1.7617	1.5623
	H	0.8746	-1.1910	0.9360
	H	-0.0305	-0.2382	1.9142
NH_2-HC(O)OH				
	C	-1.6582	2.0378	0.1982
	H	-2.3334	2.8427	0.5009
	O	-1.9604	0.9149	0.8335
	H	-1.3309	0.2173	0.5333
	O	-0.7685	2.1803	-0.6062
	N	-0.0172	-0.7401	-0.2608
	H	0.4157	-0.0412	-0.8650
	H	0.4940	-1.6084	-0.4020
NH-HC(O)OH				
	C	-1.6186	2.1011	0.2985
	H	-2.6729	2.2935	0.5139
	O	-1.4269	0.8005	0.0844
	H	-0.4804	0.6651	-0.1037
	O	-0.7677	2.9510	0.2636
	N	1.4269	0.3923	-0.4828

H	2.4307	0.5286	-0.6450

Table S.VI. NH$_x$-CH$_3$C(O)OH geometries MP2(full)/6-311++G(3df,3dp).

NH$_3$-CH$_3$C(O)OH				
	C	-0.2910	-0.7729	0.9480
	C	0.8669	-1.4982	0.3355
	H	0.6080	-1.8062	-0.6742
	H	1.7177	-0.8259	0.2628
	H	1.1217	-2.3616	0.9370
	O	-0.6405	0.2984	0.2399
	H	-1.4116	0.7313	0.7004
	O	-0.8497	-1.1172	1.9708
	N	-2.7275	1.2292	1.7386
	H	-3.6820	1.1642	1.4115
	H	-2.6489	2.0774	2.2832
	H	-2.5522	0.4421	2.3553
NH$_2$-CH$_3$C(O)OH				
	C	-1.6582	2.0378	0.1982
	H	-2.3334	2.8427	0.5009
	O	-1.9604	0.9149	0.8335
	H	-1.3309	0.2173	0.5333
	O	-0.7685	2.1803	-0.6062
	N	-0.0172	-0.7401	-0.2608
	H	0.4157	-0.0412	-0.8650
	H	0.4940	-1.6084	-0.4020
NH-CH$_3$C(O)OH				
	C	0.1155	0.0676	0.4336
	C	-0.0795	-1.3348	0.9136
	H	-1.0807	-1.6699	0.6562

H	0.6247	-1.9913	0.4095
H	0.0672	-1.3789	1.9851
O	-0.0588	0.1625	-0.8934
H	0.0829	1.0954	-1.1300
O	0.3952	1.0138	1.1331
N	0.4691	3.0347	-0.9927
H	0.6946	3.5889	-0.1592

Table S.VII. NH$_x$ harmonic vibrational frequencies B3LYP/6-311++G(3df,3dp).

NH$_3$	1021.4183	1657.4130	3685.0098
	1657.3894	3537.6381	3685.0202
NH$_2$	1532.1200	3482.4745	3582.3419
NH	3449.3131		

Table S.VIII. Acid harmonic vibrational frequencies B3LYP/6-311++G(3df,3dp).

H$_2$SO$_4$	261.6109	549.1717	1160.0433
	346.0036	563.6282	1255.1196
	382.9842	848.2147	1506.5936
	448.0311	897.4023	3829.2315
	500.9146	1140.3793	3833.7495
HNO$_3$	502.4291	793.2788	1349.2622
	597.0491	916.7006	1867.1553
	681.4867	1339.8223	3774.5154
HC(O)OH	631.1184	1140.9097	1815.9071
	683.8242	1306.6028	3130.0042
	1065.5835	1415.4169	3799.2423
CH$_3$C(O)OH	96.3462	1011.4869	1497.7403
	427.9977	1077.5123	1829.8326
	558.4941	1210.2043	3088.5310
	589.6853	1347.6280	3176.8170
	671.8852	1428.8327	3220.7113
	883.8434	1487.3897	3810.7919

Table S.IX. NH$_x$-H_2SO_4 harmonic vibrational frequencies B3LYP/6-311++G(3df,3dp).

NH_3-H_2SO_4	43.2467	538.1845	1434.3097
	94.6634	565.1098	1530.3841
	125.7830	576.9102	1659.8988
	251.7525	841.4471	1667.3101
	282.8089	965.9156	2434.9158
	351.4243	1150.5882	3512.8109
	389.2510	1153.0534	3645.8234
	426.8460	1190.1843	3669.5868
	461.1696	1238.5678	3843.0822
NH_2-H_2SO_4	46.3291	445.2010	1244.1746
	104.6627	532.8147	1387.6181
	143.6917	559.1316	1490.4746
	242.5801	568.7727	1523.5353
	278.0015	847.0829	3054.4559
	331.5030	942.6370	3513.7337
	381.1704	965.7063	3625.5087
	408.3222	1152.0111	3839.9183
NH-H_2SO_4	41.3513	435.6531	1151.5426
	56.4122	517.6521	1250.5260
	199.1004	552.4043	1271.3219
	252.3442	565.7474	1496.2317
	269.6405	746.2055	3501.2330
	291.8244	851.0580	3536.1397
	390.6885	920.9071	3837.6571

Table S.X. NH_x-HNO_3 harmonic vibrational frequencies B3LYP/6-311++G(3df,3dp).

NH_3-HNO_3	61.9228	710.3165	1656.6963
	76.4684	809.6925	1664.8767
	121.6442	987.4229	1823.3093
	254.1932	1130.3237	2849.2466
	326.3007	1135.3288	3520.4052
	408.2121	1355.1547	3658.2949
	668.7804	1549.9806	3666.9067
NH_2-HNO_3	74.2072	652.4862	1496.0318
	96.4069	709.9475	1534.6338
	105.0102	801.5584	1840.6772
	232.4131	963.0098	3231.9585
	321.6007	993.1063	3511.7279
	370.2516	1396.8878	3618.1762
NH-HNO_3	67.4462	624.3078	1351.2178
	68.3923	697.3504	1412.7304
	180.3295	777.1623	1847.6045

Table S.XI. NH_x-HC(O)OH harmonic vibrational frequencies B3LYP/6-311++G(3df,3dp).

NH_3-HC(O)OH	116.0191	1056.9542	1671.3601
	122.9253	1110.0636	1780.3596
	183.8657	1144.6213	3075.1558
	253.5836	1245.6037	3115.2275
	326.3746	1405.8369	3508.5528
	424.1677	1492.5674	3646.0441
	710.0387	1653.3068	3672.4935
NH_2-HC(O)OH	113.8481	691.3032	1513.0771
	163.6994	970.4724	1790.2122
	184.5733	1084.7218	3111.1496
	227.3399	1224.2457	3391.4323
	324.4897	1393.9557	3495.3500
	375.8878	1453.7248	3610.4424
NH-HC(O)OH	43.5496	660.9717	1427.6059
	141.1826	858.5766	1804.2874
	178.6484	1074.0582	3114.0663
	235.7864	1186.5572	3487.4712
	254.1526	1351.2355	3643.4190

Table S.XII. NH_x-$CH_3C(O)OH$ harmonic vibrational frequencies B3LYP/6-311++G(3df,3dp).

NH_3-$CH_3C(O)OH$	73.8260	908.9435	1651.4292
	91.9344	1029.2218	1673.7419
	125.6494	1076.7040	1789.9437
	130.4395	1094.3374	3085.4993
	222.0878	1099.7933	3159.3126
	297.1636	1317.7423	3173.9378
	406.2991	1408.2556	3215.4016
	466.4069	1478.2991	3505.2258
	607.6630	1492.8935	3644.0275
	636.9993	1497.5559	3674.2986
NH_2-$CH_3C(O)OH$	71.8127	625.2294	1497.4322
	92.9036	903.5563	1508.8808
	117.6479	947.1825	1800.1953
	183.7792	1026.7887	3086.5804
	200.4983	1077.5008	3175.0171
	314.4737	1295.6043	3216.8584
	362.5000	1394.0553	3445.1189
	449.9001	1455.0723	3491.7913
	602.9811	1486.8677	3609.0819
NH-$CH_3C(O)OH$	61.6961	606.2390	1486.7034
	75.5185	802.5234	1497.4013
	93.0773	894.3316	1810.5559
	153.3705	1020.9310	3087.7434
	235.4442	1077.4213	3176.2531
	243.5668	1253.8695	3219.1071
	438.2595	1367.8467	3488.1228
	593.1492	1434.8648	3661.8710

A-4 Chapter 4 Supporting Information

How to use the Scanning Mobility Particle Sizer (SMPS) instrument and its Software.

When fully assembled instrument is turned on, it goes through a self-test and then displays standby mode on the LCD screen of the instrument. At this point one can control the Instrument through a computer software provided with the Instrument.

When the Software is started it displays following screen

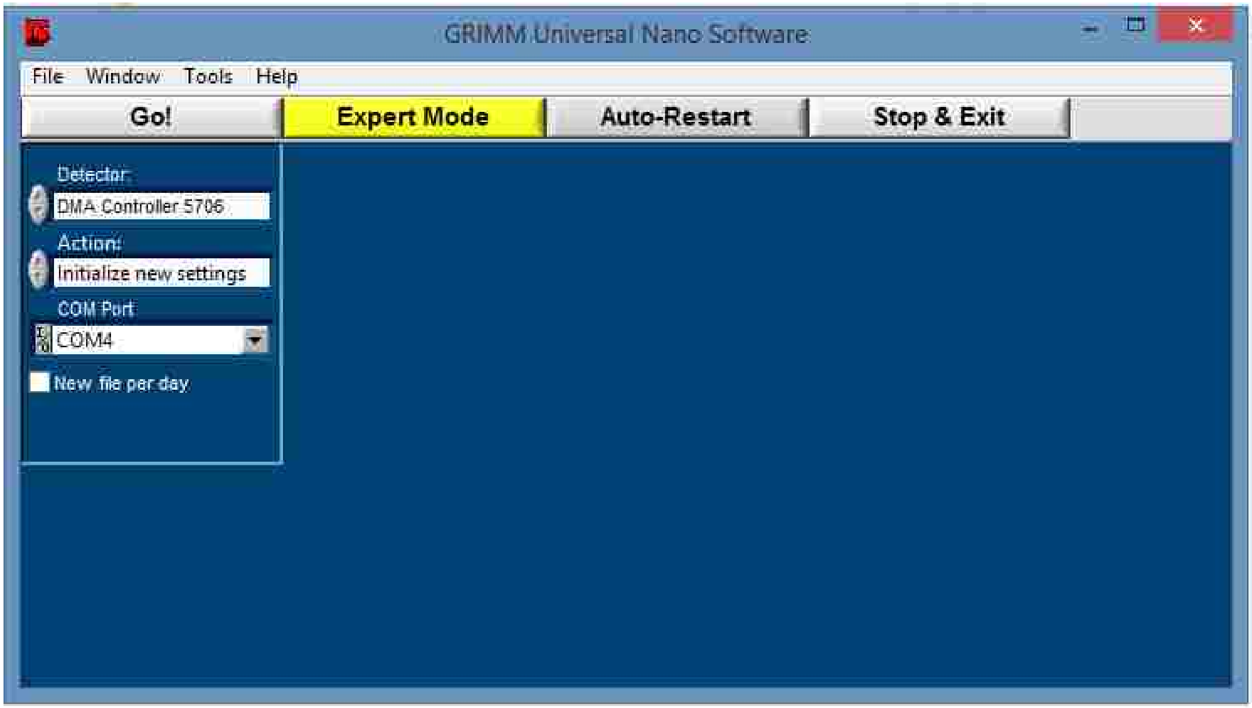

Detector: DMA Controller 5706

Action: Initialize new settings

COM Port: COM4

☐ New file per day

The software is a form of a Lab-view program. The buttons and bullions works exactly as the lab-view software. For example clicking on the un and down arrow next to detector, would cycle through the available options of the detector, or, if you click on DMA controller 5706 it will display all the options at once to choose from.

Pressing stop and exit would shut the program down.

Pressing auto restart would run the software on previously saved setting.

Pressing GO would execute the action chosen in the action tab.

Detector: DMA Controller 5706

Action: Initialize new settings

COM Port: COM4

Do not chose any other detector unless you have it connected. The software is common for all the instruments Grimm technology makes. We have bought controller 5706, thus we must chose the same.

Makes sure you have correct COM port selected in the COM port dialog box. Software is smart enough to detect correct COM port on its own.

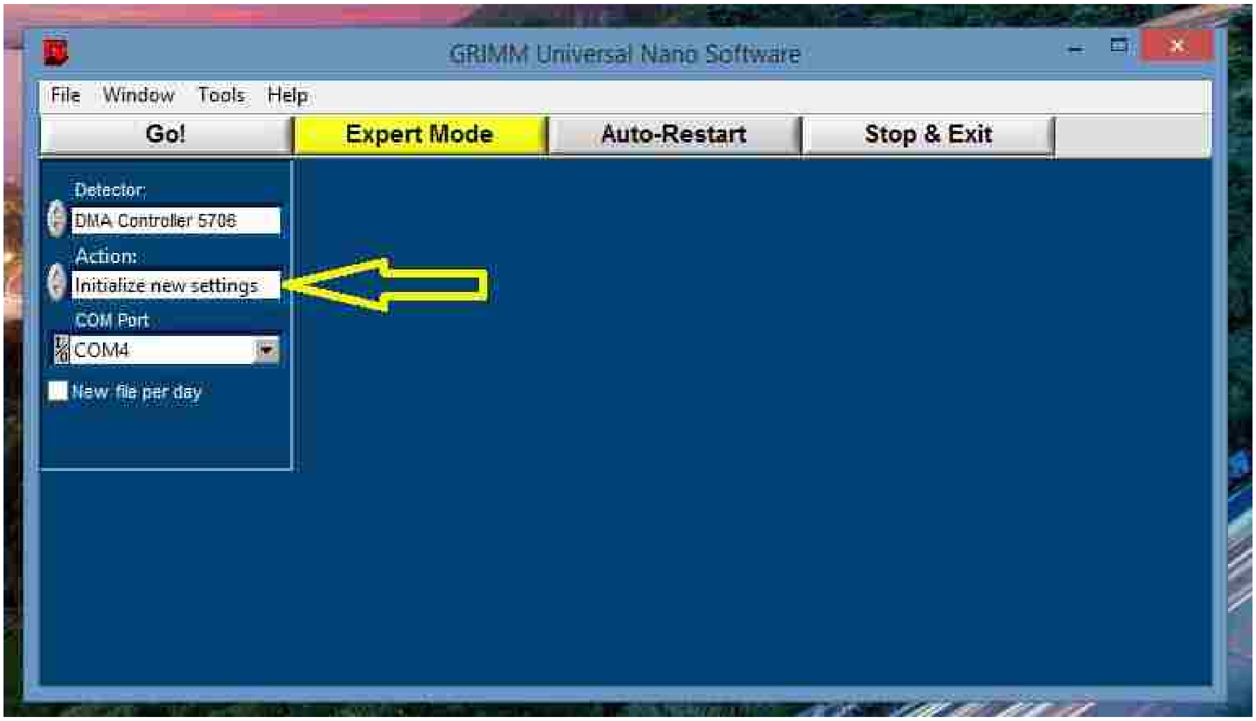

Detector: DMA Controller 5706

Action: Initialize new settings

COM Port: COM4

☐ New file per day

This tab allows you to do the following:

1. Initialize new setting
2. Open protocol file (view previously saved data)
3. Open .raw file (open previously saved data and be able to run from where you left it last)
4. Use last setting (allows you to jump to control setting directly without choosing the parameters, like new setting does)

When you chose to initialize new setting, software will ask you to create a file name and destination to save the file. Upon doing so, following screen will appear

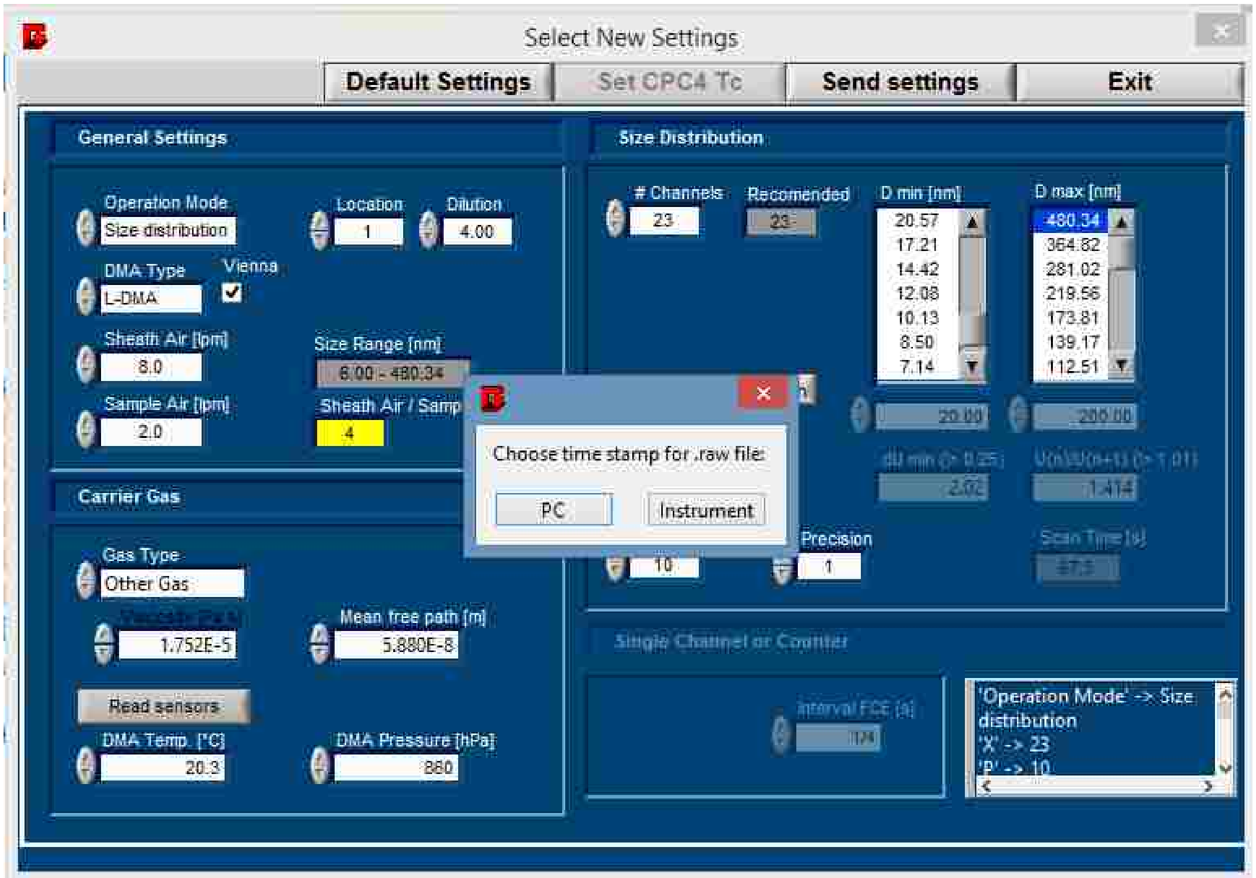

Operation Mode: Size distribution
Location: 1
Dilution: 4.00
DMA Type: L-DMA
Vienna: ☑
Sheath Air [lpm]: 8.0
Sample Air [lpm]: 2.0
Size Range [nm]: 8.00 - 480.34
Sheath Air / Samp: 4
Gas Type: Other Gas
1.752E-5
Mean free path [m]: 5.880E-8
DMA Temp. [°C]: 20.3
DMA Pressure [hPa]: 880
Channels: 23
Recomended: 23
D min [nm]: 20.57, 17.21, 14.42, 12.08, 10.13, 8.50, 7.14
D max [nm]: 480.34, 364.82, 281.02, 219.56, 173.81, 139.17, 112.51
20.00
200.00
2.02
1.414
10
Precision: 1

'Operation Mode' -> Size distribution
'X' -> 23
'P' -> 10

Choose time stamp for .raw file:

Chose the time that you trust. I always chose PC time.

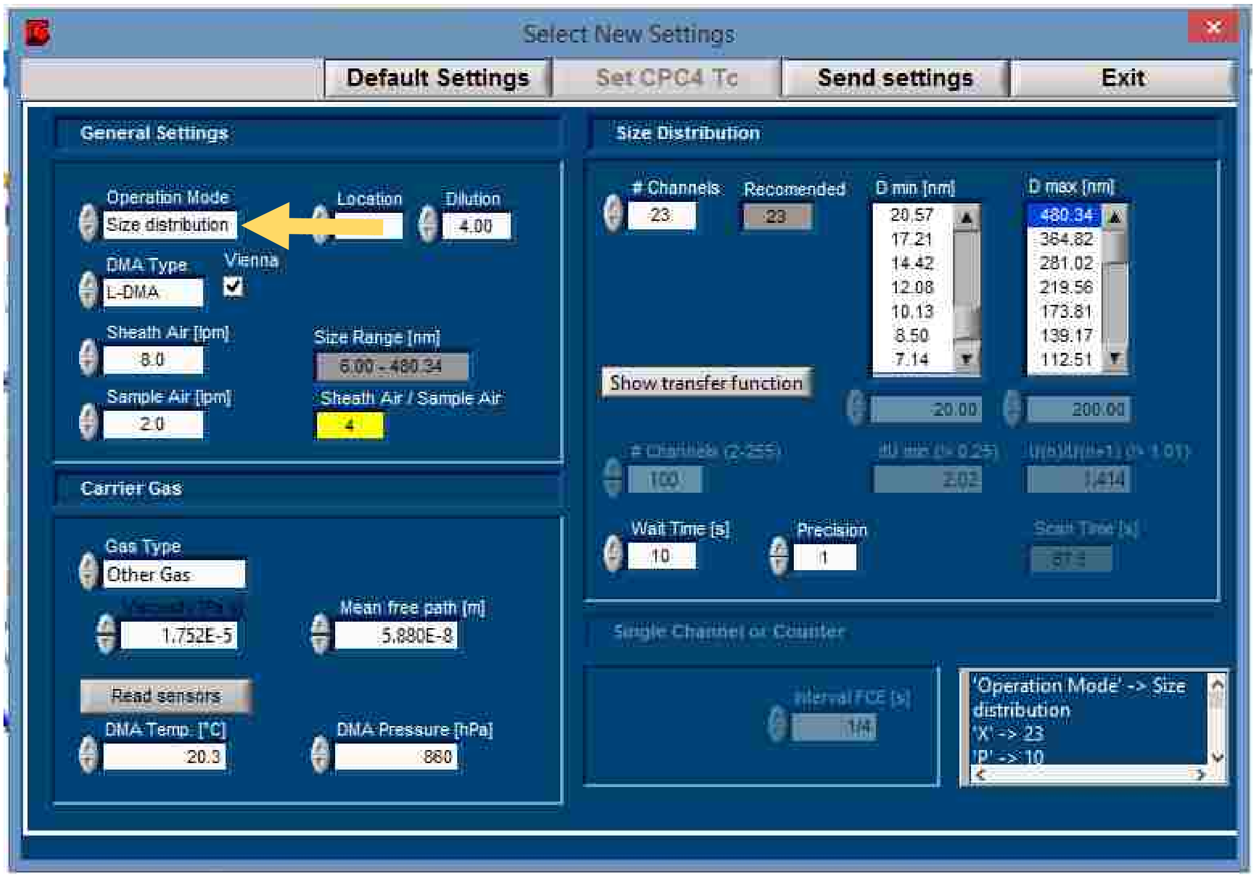

Operation Mode: Size distribution
Location:
Dilution: 4.00
DMA Type: L-DMA
Vienna: ☑
Sheath Air [lpm]: 8.0
Sample Air [lpm]: 2.0
Size Range [nm]: 6.00 - 480.34
Sheath Air / Sample Air: 4
Gas Type: Other Gas
1.752E-5
Mean free path [m]: 5.880E-8
DMA Temp. [°C]: 20.3
DMA Pressure [hPa]: 860
Channels: 23
Recomended: 23

D min [nm]	D max [nm]
20.57	480.34
17.21	364.82
14.42	281.02
12.08	219.56
10.13	173.81
8.50	139.17
7.14	112.51
20.00	200.00

Channels (2-255): 100
dU min (> 0.25): 2.02
U(n)/U(n+1) (> 1.01): 1.414
Wait Time [s]: 10
Precision: 1
Interval FCE [s]: 1/4

'Operation Mode' -> Size distribution
'X' -> 23
'P' -> 10

Operation Mode has two options, size distribution or single channel. For this experiment size distribution is chosen for we want size distribution and particle concentration. Single channel only measures the particle concentration. This may be used to calibrate the instrument by introducing known concentrations of uniform size particles coming from a different DMA source.

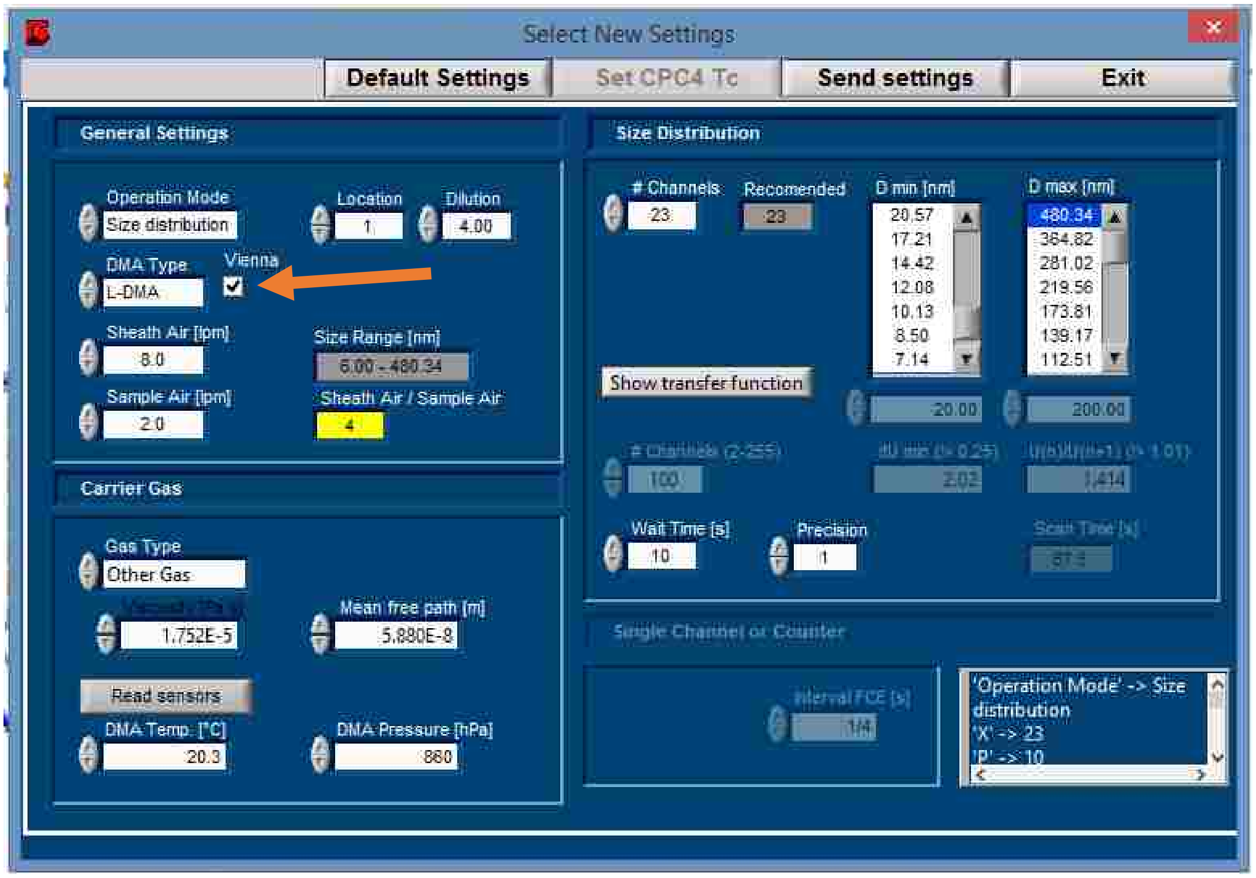

Operation Mode: Size distribution
Location: 1
Dilution: 4.00
DMA Type: L-DMA
Vienna: ☑
Sheath Air [lpm]: 8.0
Size Range [nm]: 6.00 - 480.34
Sample Air [lpm]: 2.0
Sheath Air / Sample Air: 4
Gas Type: Other Gas
1.752E-5
Mean free path [m]: 5.880E-8
DMA Temp. [°C]: 20.3
DMA Pressure [hPa]: 860
Channels: 23
Recomended: 23

D min [nm]	D max [nm]
20.57	480.34
17.21	384.82
14.42	281.02
12.08	219.56
10.13	173.81
8.50	139.17
7.14	112.51
20.00	200.00

Channels (2-255): 100
dU min (> 0.25): 2.02
U(n)/U(n+1) (> 1.01): 1.414
Wait Time [s]: 10
Precision: 1
Interval FCE [s]: 1/4

'Operation Mode' -> Size distribution
'X' -> 23
'P' -> 10

DMA type has following three options, L – DMA, M – DMA, S – DMA. We have purchased all three DMA with our SMPS. Please choose the appropriate DMA connected to the controller. All our DMA are the new ones or the Vienna type DMA. So please check the Veinna box.

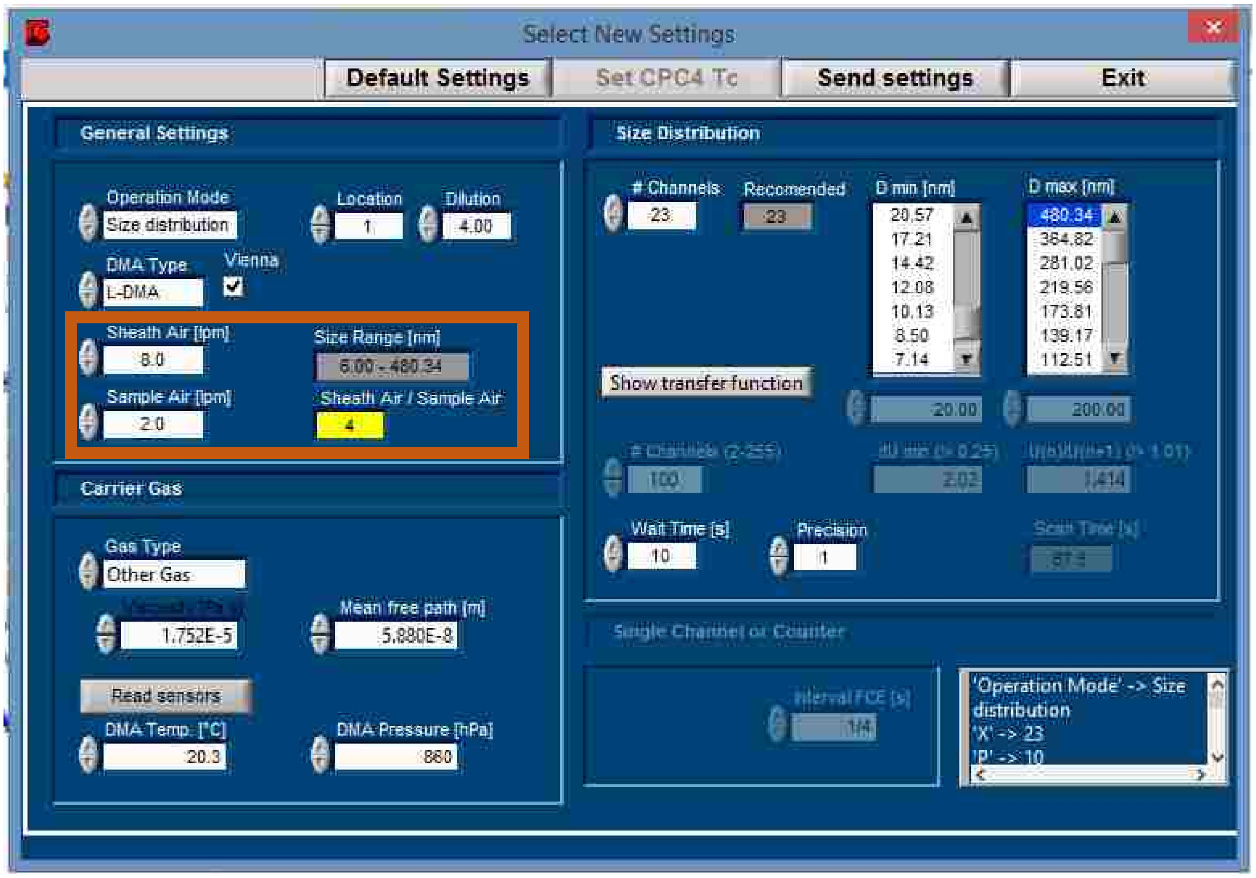

Operation Mode: Size distribution
Location: 1
Dilution: 4.00
DMA Type: L-DMA
Vienna ☑
Sheath Air [lpm]: 8.0
Size Range [nm]: 6.00 - 480.34
Sample Air [lpm]: 2.0
Sheath Air / Sample Air: 4
Gas Type: Other Gas
1.752E-5
Mean free path [m]: 5.880E-8
DMA Temp. [°C]: 20.3
DMA Pressure [hPa]: 860
Channels: 23
Recomended: 23
D min [nm]: 20.57, 17.21, 14.42, 12.08, 10.13, 8.50, 7.14
D max [nm]: 480.34, 364.82, 281.02, 219.56, 173.81, 139.17, 112.51
20.00
200.00
Channels (2-255): 100
dU min (> 0.25): 2.02
U(n)/U(n+1) (> 1.01): 1.414
Wait Time [s]: 10
Precision: 1
Interval FCE [s]: 1/4
'Operation Mode' -> Size distribution
'X' -> 23
'P' -> 10

The ratio of Sheath air flow (flowing through DMA to separate the particles) against the sample air flow (flow rate at which sample is collected) decides the particle size range you can measure with a particular DMA. Smaller this ratio bigger the size range one can measure. But, with smaller ratios the smallest particle size that instrument can measure is much bigger.

For example, at Sheath air flow of 3 LPM and Sample Air flow of 2 LPM the ratio will be 1.5 and the range one can measure is 9.85 – 1117.12 nm. Whereas for Sheath air flow of 20 LPM and Sample air flow of 2 LPM the ratio will be 10 and the range one can measure is 3.78 – 289.35nm.

Ideally one must use a ratio of 8 and above for most accurate and reliable results, for this experiment sheath air flow of 8 LPM and sample air flow of 4 LPM (for LDMA) was used to be able to measure the best possible size range.

Our DMA only allows a maximum sheath air flow of 20.0LPM and a maximum sample air flow of 3 LPM. Thus please do not chose other available option with those settings such as 75 LPM for sheath air flow.

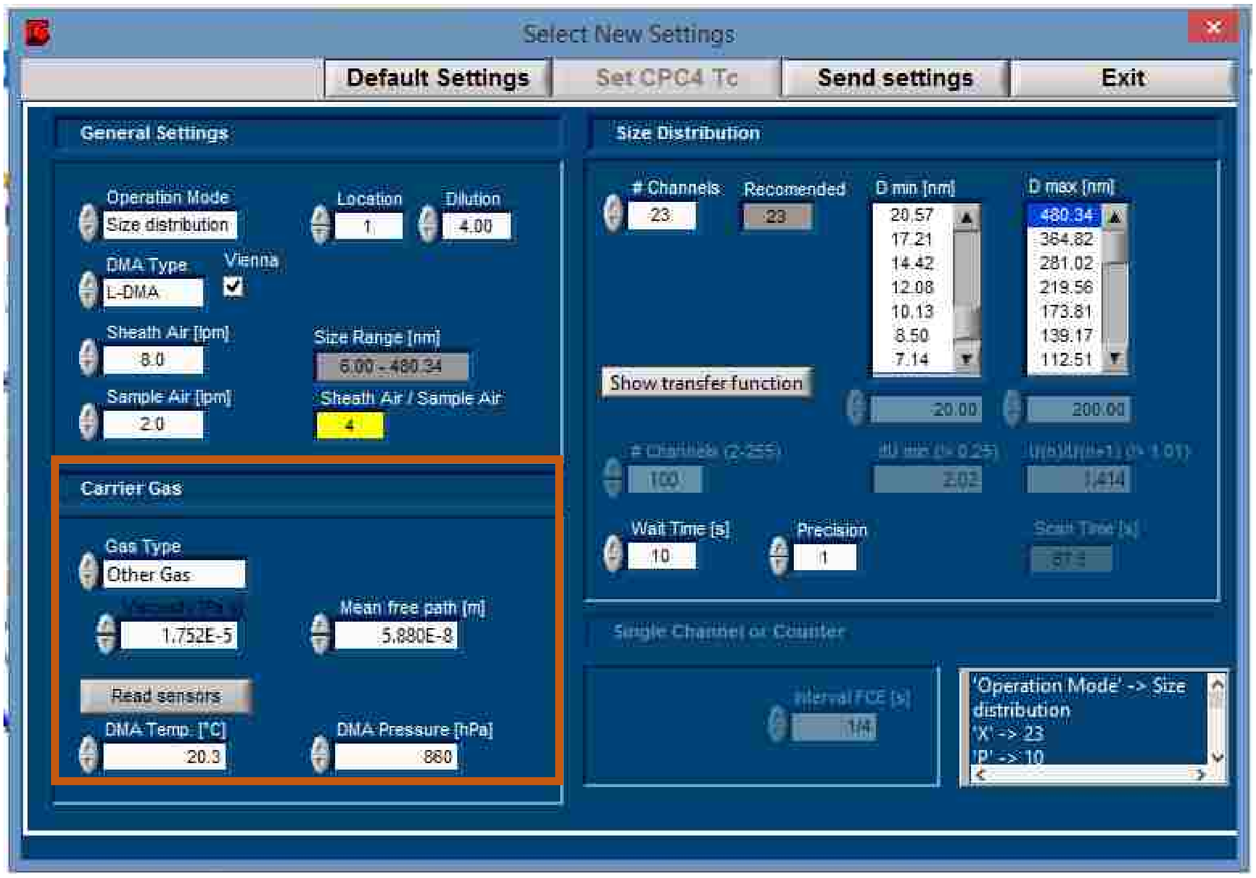

Operation Mode: Size distribution
Location: 1
Dilution: 4.00
DMA Type: L-DMA
Vienna ☑
Sheath Air [lpm]: 8.0
Size Range [nm]: 6.00 - 480.34
Sample Air [lpm]: 2.0
Sheath Air / Sample Air: 4

Gas Type: Other Gas
1.752E-5
Mean free path [m]: 5.880E-8
DMA Temp. [°C]: 20.3
DMA Pressure [hPa]: 880

Channels: 23
Recomended: 23

D min [nm]	D max [nm]
20.57	480.34
17.21	364.82
14.42	281.02
12.08	219.56
10.13	173.81
8.50	139.17
7.14	112.51

20.00
200.00
Channels (2-255): 100
dD min (> 0.25): 2.02
D(n)/D(n+1) (> 1.01): 1.414
Wait Time [s]: 10
Precision: 1
Interval FCE [s]: 1/4

'Operation Mode' -> Size distribution
'X' -> 23
'P' -> 10

The number displayed above are for Oxygen gas as the carrier gas of the sampling aerosol particles. Viscocity and mean free path are manually entered in the box.

DMA temperature and pressure can be entered manually or be obtained by clicking read sensor tab. It automatically measures the DMA temperature and pressure. A kit for calibrating DMA temperature and pressure is provided with the instrument.

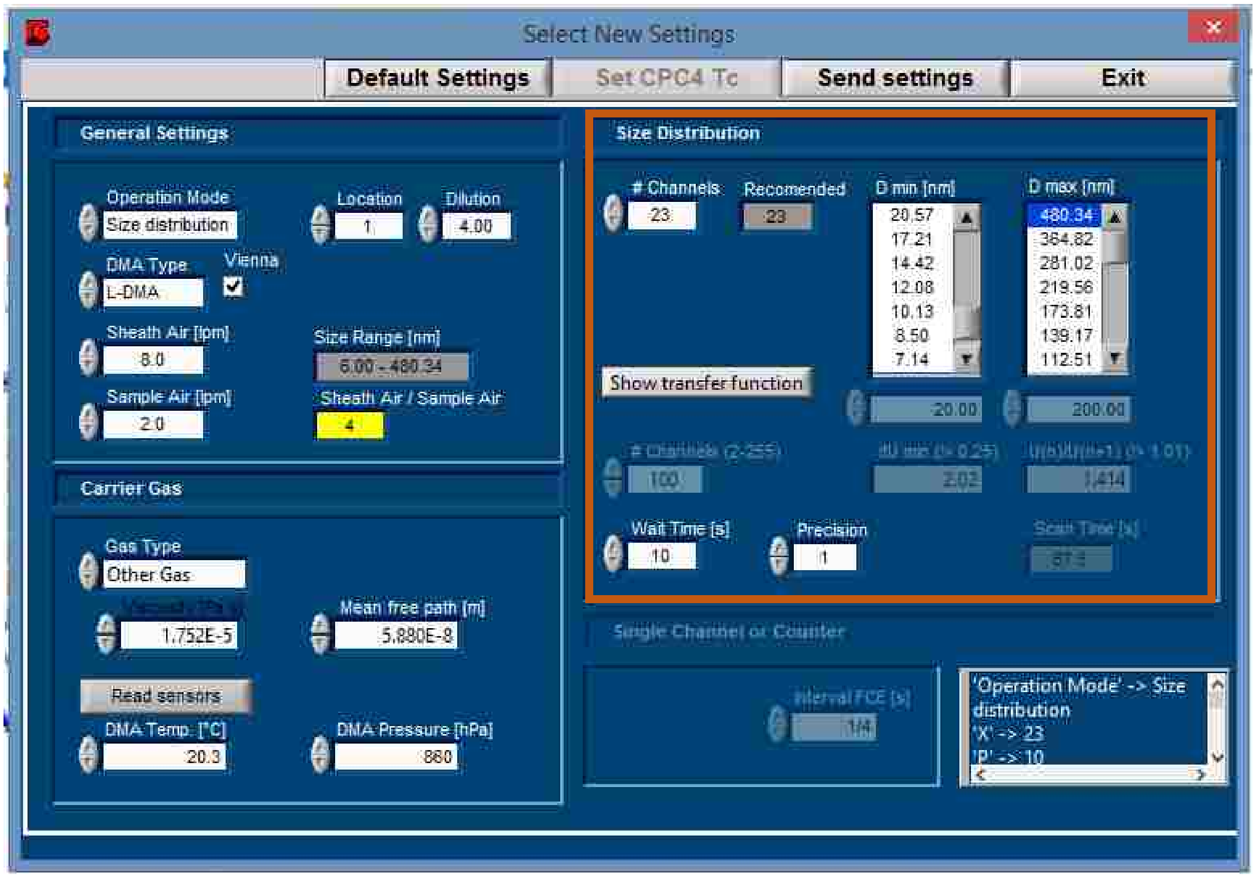

General Settings

Operation Mode: Size distribution
Location: 1
Dilution: 4.00
DMA Type: L-DMA
Vienna: ☑
Sheath Air [lpm]: 8.0
Sample Air [lpm]: 2.0
Size Range [nm]: 6.00 - 480.34
Sheath Air / Sample Air: 4

Carrier Gas

Gas Type: Other Gas
1.752E-5
Mean free path [m]: 5.880E-8
DMA Temp. [°C]: 20.3
DMA Pressure [hPa]: 860

Size Distribution

Channels: 23
Recomended: 23
D min [nm]: 20.57, 17.21, 14.42, 12.08, 10.13, 8.50, 7.14
D max [nm]: 480.34, 364.82, 281.02, 219.56, 173.81, 139.17, 112.51
20.00
200.00
Channels (2-255): 100
dU min (> 0.25): 2.02
U(n)/U(n+1) (> 1.01): 1.414
Wait Time [s]: 10
Precision: 1
Scan Time [s]

Single Channel or Counter

Interval FCE [s]: 1/4

'Operation Mode' -> Size distribution
'X' -> 23
'P' -> 10

This box will be inactive if single channel operation mode is chosen on left hand side first box.

The number of recommended channels changes with the change in sheath air flow/sample air flow ratio. The number of channels decides the sensitivity of your measurement. More the channel more the sensitivity better the distribution. One must chose at least the recommended channels for optimum results. Dmin and Dmax dispalys the size range distribution. The distribution with respect to DMA voltage can be seen by clicking the show transfer function tab. Wall time represents the wait time between two consecutive runs. Precision number decides how many times a measurement is taken at a particular voltage or size. That is at a precision of 3, the instrument will measure the particle concentration three times at 10000 V before moving on to next voltage of 7071 V.

Scan time displays the time required to finish one run from 10000 V to 4.9 V including the wall time. While using multiple SMPS for the same sample, try and match the scan times for both the instruments. This can be done by adjusting the precision and wall time.

Once all the settings are adjusted, click send setting on top bar. This will open another dialogue box which runs on its own, and identifies the adjusted settings and calculates the FCE offset of the instrument at that setting. The FCE offset is displayed at the end of this dialogue box. Click OK to measured FCE offset window and close the “initialize new setting” window.

At this you will see the following window

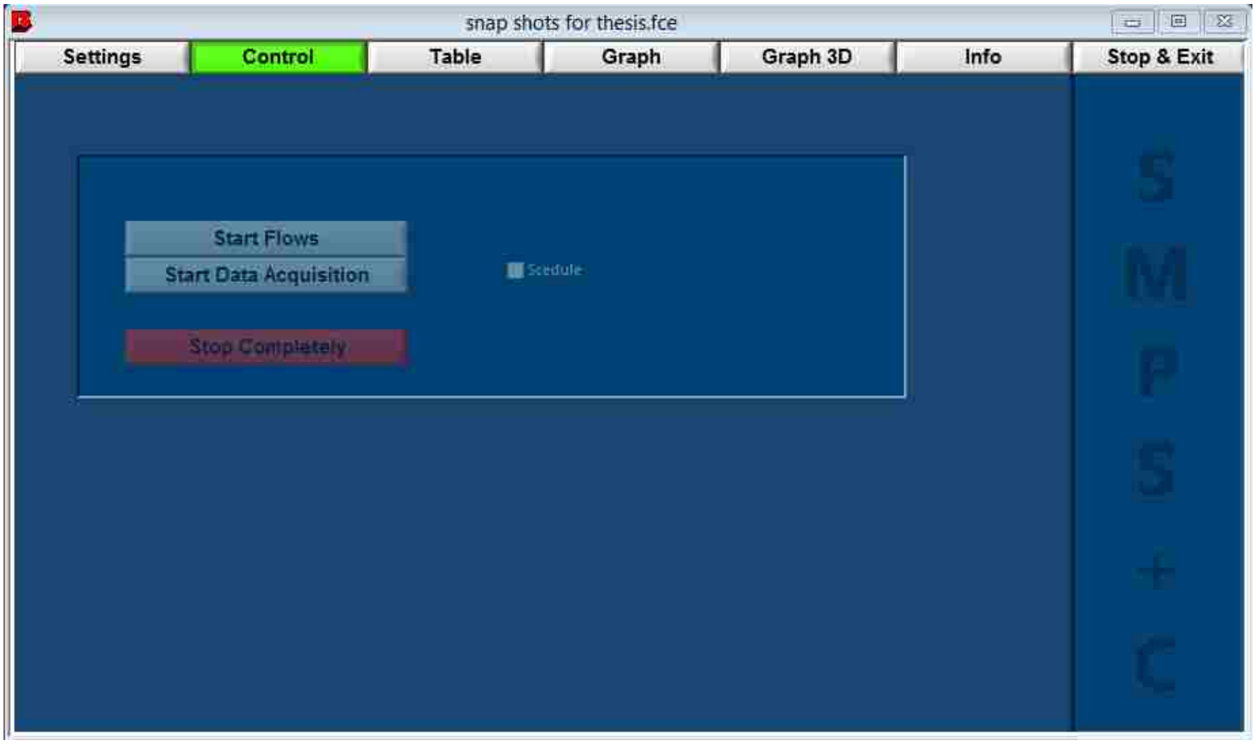

Click the Control tab up top

1. Click Start flows tab
2. Wait for 10-15 seconds for flows to stabilize in the instrument.
3. After 15 seconds, click Start data acquisition.
4. An audible beep will be heard from the instrument indicating no memory card in present in the instrument. (the message will be displayed on the instrument LCD display)
5. At this point instrument is measuring data. It can be viewed live by clicking the graph tab

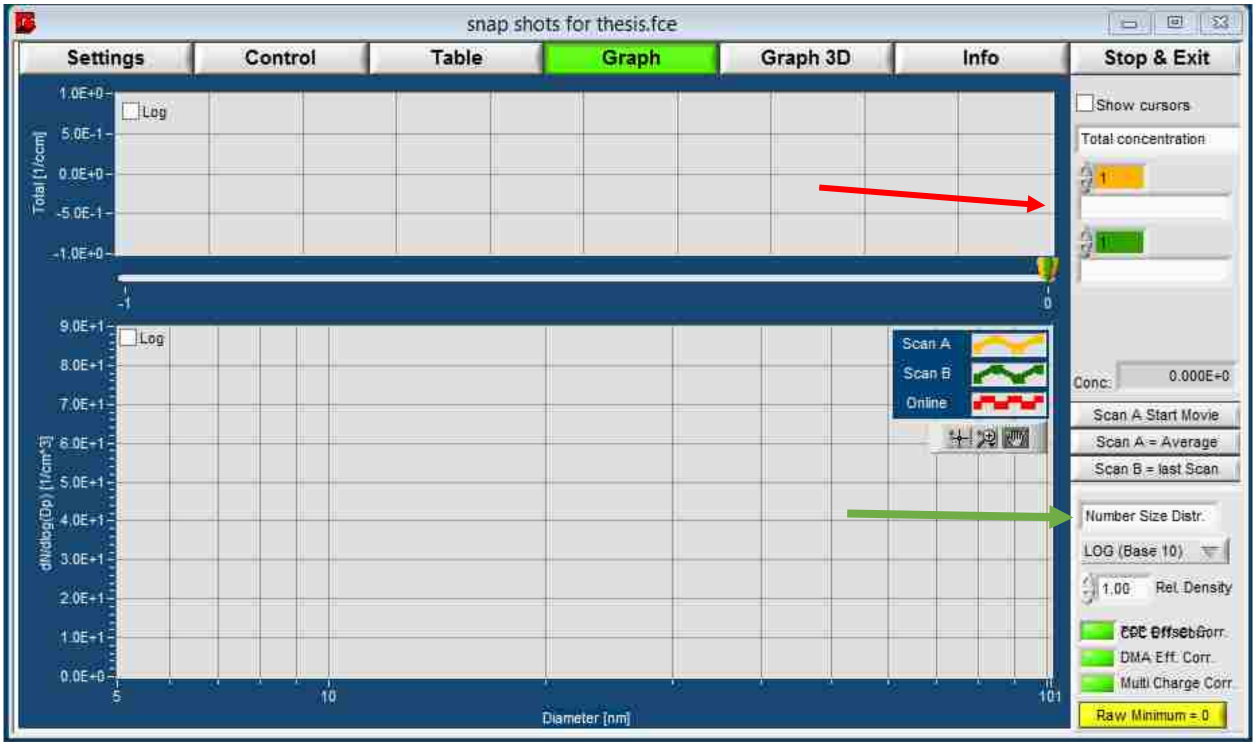

The bottom graph displays the size distribution and density of individual runs. Instrument allows to view three runs at a time. One in yellow, one in green and one live in red. The sum of the are under the peak of each run represents the total particle count of the run and is displayed in the top graph. The actual total particle concentration can be viewed in the dialogue box marked pointed in red arrows.

By clicking the dialogue box pointed in green, allows the user to change the Y axis of the bottom graph. It allows the user to measure either of the following properties of the particle: raw data (FCE current measured at each voltage), Number size distribution (the standard method of reporting the data dN/dlog(Dp) in the units of 1/cm^3), surface size distribution, volume size distribution, mass size distribution or the number of particles. Curtius et al paper has the formulas to convert from one unit to another.

Upon completion of data collection, click on the control tab and stop the data acquisition first. Wait for 15 seconds. Then click stop flows. Wait for 15 seconds again and then shut the program down or extract the collected data in excel or text form by following method.

Once you have stopped the data collection completely, click the Table tab, you will see size and concentration data in excel format. On the right hand side of the data there are options to either export data as .txt, or to excel. Click export to excel and Excel program will automatically start with the data in it. Save the excel file and you are done.